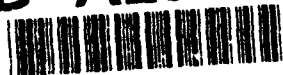PL-TR-92-2149

THE RECEIVER STRUCTURE BENEATH THE CHINESE DIGITAL SEISMOGRAPH NETWORK (CDSN) STATIONS: PRELIMINARY RESULTS

S. Mangino
J. Ebel

Weston Observatory
Department of Geology and Geophysics
Boston College
Weston, MA 02193

DTIC
ELECTE
AUG 2 6 1992
S A D

30 April 1992

APPROVED FOR PUBLIC RELEASE; DISTRIBUTION UNLIMITED

92-23675
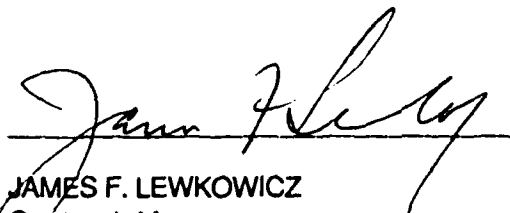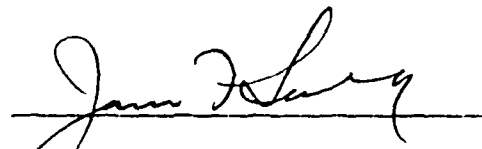|||||||||||||||||

92 8 25 108

The views and conclusions contained in this document are those of the authors and should not be interpreted as representing the official policies, either expressed or implied, of the Air Force or the U.S. Government.

This technical report has been reviewed and is approved for publication.

JAMES F. LEWKOWICZ
Contract Manager
Solid Earth Geophysics Branch
Earth Sciences Division

JAMES F. LEWKOWICZ
Branch Chief
Solid Earth Geophysics Branch
Earth Sciencs Division

DONALD H. ECKHARDT, Director
Earth Sciences Division

This document has been reviewed by the ESD Public Affairs Office (PA) and is releasable to the National Technical Information Service (NTIS).

Qualified requestors may obtain additional copies from the Defense Technical Information Center. All others should apply to the National Technical Information Service.

If your address has changed, or if you wish to be removed from the mailing list, or if the addressee is no longer employed by your organization, please notify PL/IMA, Hanscom AFB MA 01731-5000. This will assist us in maintaining a current mailing list.

Do not return copies of this report unless contractual obligations or notices on a specific document requires that it be returned.

REPORT DOCUMENTATION PAGE

Public reporting burden for this collection of information is estimated to average 1 hour per response, including the time for reviewing instructions, searching existing data sources, gathering and maintaining the data needed, and completing and reviewing the collection of information. Send comments regarding this burden estimate or any other aspect of this collection of information, including suggestions for reducing this burden, to Washington Headquarters Services, Directorate for Information Operations and Reports, 1215 Jefferson Davis Highway, Suite 1204, Arlington, VA 22232-4302 and to the Office of Management and Budget, Paperwork Reduction Project (0704-0188), Washington, DC 20503

1. AGENCY USE ONLY (Leave blank)	2. REPORT DATE 30 April 1992	3. REPORT TYPE AND DATES COVERED Scientific Report No. 1

4. TITLE AND SUBTITLE

The Receiver Structure Beneath the Chinese Digital Seismograph Network (CDSN) Stations: Preliminary Results

5. FUNDING NUMBERS

PE 61102F
PR 2309 TAG2 WU AW
Contract F19628-91-K0009

6. AUTHOR(S)

S. Mangino and J. Ebel

7. PERFORMING ORGANIZATION NAME(S) AND ADDRESS(ES)

Weston Observatory
Department of Geology and Geophysics
Boston College
Weston, MA 02193

8. PERFORMING ORGANIZATION REPORT NUMBER

9. SPONSORING/MONITORING AGENCY NAME(S) AND ADDRESS(ES)

Phillips Laboratory
Hanscom AFB, MA 01731-5000

Contract Manager: James Lewkowicz/GPEH

10. SPONSORING MONITORING AGENCY REPORT NUMBER

PL-TR-92-2149

11. SUPPLEMENTARY NOTES

12a. DISTRIBUTION/AVAILABILITY STATEMENT

Approved for public release;
Distribution unlimited

12b. DISTRIBUTION CODE

13. ABSTRACT (Maximum 200 words)

This report provides preliminary results of an investigation of the crust and upper-mantle seismic velocity structure beneath the China Digital Seismograph Network (CDSN). Receiver functions obtained from over 100 teleseismic events were stacked by common backazimuth and epicentral distance and inverted for the velocity structure beneath 5 CDSN stations. The inversion results show that stations HIA and BJI have well constrained crustal models of about 40-km thickness with gradational Mohos. At WMQ there is evidence for shallow dipping structure and the inversion results indicate a smooth positive gradient in the crust with a transitional crust-mantle boundary. Model estimates for KMI and LZH are poorly constrained by the data analyzed thus far. Synthetic seismograms of 5 CDSN crustal models for the Soviet JVE nuclear test indicate that the receiver structure most strongly affects the radial component of the recorded P wave.

14. SUBJECT TERMS

Seismology   Crustal Structure Upper Mantle Structure
China Receiver Function   Regional phases   Teleseismic

15. NUMBER OF PAGES
108

16. PRICE CODE

17. SECURITY CLASSIFICATION OF REPORT	18. SECURITY CLASSIFICATION OF THIS PAGE	19. SECURITY CLASSIFICATION OF ABSTRACT	20. LIMITATION OF ABSTRACT
Unclassified	Unclassified	Unclassified	SAR

NSN 7540-01-280-5500

Table of Contents

Accesion For		
NTIS CRA&I	☑	
DTIC TAB	☐	
Unannounced	☐	
Justification		
By		
Distribution /		
Availability Codes		
Dist	Avail and/or Special	
A-1		

iii

List of Figures

List of Tables

The Receiver Structure Beneath the China Digital Seismograph Network (CDSN) Stations: Preliminary Results

Stephen Mangino and John Ebel

Weston Observatory
Boston College
Weston, MA 02193

SUMMARY

This study provides preliminary model estimates of the crust and upper mantle velocity structure in China beneath the Chinese Digital Seismograph Network. The one-dimensional models are derived from receiver functions obtained from teleseismic data recorded at each station. Individual models are used to investigate the effects of the receiver structure on regional waveforms recorded at each station.

Key Words: receiver function, teleseismic, inversion, shear velocity, crust, upper mantle, China.

1.0 INTRODUCTION

A renewed interest in furthering restrictions on testing and proliferation of nuclear weapons has motivated the seismological community to develop effective regional and teleseismic methods of detection and discrimination between small earthquakes and low threshold nuclear explosions. In particular, the availability of high quality data from seismograph stations installed in China and the Russian States has opened up research efforts to improve current levels of effective detection and discrimination of events recorded on the Eurasian continent.

Most current regional explosion yield estimation and discrimination methods are based on spectral analysis of seismic data, however the spectra of particular regional seismic phases such as P_g, P_n, S_n, and L_g are affected by attenuation and scattering near the source, along the crust-

mantle path, and near the receiver. As a consequence, for a given region correction terms are necessary prior to evaluating data from a given station. One way to estimate the crustal velocity structure is by active, dense seismic refraction and reflection surveys, but unfortunately such costly efforts are often not practical or feasible. An alternative method is through the detailed analysis of passively recorded teleseismic data. The purpose of this work is to determine the crustal response at several stations in China using teleseismic data in order to better understand earthquake and explosion waveforms recorded by these stations.

Teleseismic body waveforms provide a wealth of information on the velocity structure beneath three-component seismic stations (for example, Archambeau et al. 1966; Basham and Ellis 1969; Kurita 1969; Bakun 1971). Time domain modeling of broadband teleseismic P-waveforms to determine the crust and upper mantle velocity structure beneath three component seismic stations is well established in seismology (Burdick and Langston 1977; Langston 1977b; Langston 1979; Langston 1981; Owens et al. 1984, 1987, 1988a, 1988b; Ammon et al. 1990; Mangino et al. 1992). In this report we describe the response and present preliminary models of the seismic velocity structure beneath five China Digital Seismograph Network (CDSN) stations. Operated by the State Seismological Bureau Peoples Republic of China in cooperation with the Albuquerque Seismological Laboratory US Geological Survey, the CDSN stations record high quality broadband digital data in continuous and trigger mode. This network currently represents 12% (as of March 26, 1992) of all stations consistently providing data to the Global Digital Seismic Network (GDSN). Across mainland China from east to west shown in Figure 1a the CDSN stations are: Mudanjiang, Heilongjiang province (MDJ); Hailar, Neimenggu Province (HIA); Beijing, Baijatuan (BJI); Kunming, Yunnan Province (KMI); Lanzhou, Gansu Province (LZH); and Urumqi, Xinjiang Province (WMQ).

Sections 1 and 2 summarize current interpretations of the tectonic history and describe some a priori crustal information which was gathered in the vicinity of each station. We use this information and forward modeling to construct initial models for the time domain inversion procedure (Ammon et al. 1990) used in this report. Section 3 summarizes the receiver function

2

modeling technique and in Section 4 we describe the teleseismic data obtained from the archives. Section 5 describes the receiver functions at each CDSN station. The responses at each station ranges from simple to complex, and the degree of complexity seems to correlate with the amount of geologic deformation experienced at each site. Section 6 presents a summary of the teleseismic P-waveform time domain inversion procedure given in Ammon et al. (1990). Section 7 presents preliminary estimates of the crustal velocity structure beneath each CDSN station. To date our focus has been on matching only the most prominent arrivals in the data within ±1 standard deviation bounds obtained from the variance of the stacked data. Section 8 assesses the implications for monitoring earthquake and explosion sources at these stations.

2.0 GEOLOGIC OVERVIEW OF CHINA

The following sections are intended to summarize the current view of the tectonic history of mainland China, in order to build a framework for interpreting the observed receiver functions and inferred crustal models beneath each CDSN station. One problem encountered in preparing this summary was the lack of consistent nomenclature, ubiquitous among English language and translations of Chinese papers, in reference to the same crustal features and physiographic province. From previous work we can obtain estimates of the average crustal P-wave velocity. However, estimates of total crustal thickness vary by as much as 8 km and upper mantle P velocity vary by as much as 0.5 km/s from paper to paper for some stations. Overall, Acta Seismologica Sinica edited by the Seismological Society of China was a most useful source of information. For additional information on the tectonic history and current topics of research refer to: Yuan et al. (1986); Hsu et al. (1990); Zhao et al. (1990); Gilder et al. (1991); Shangyou (1991) and Birchfiel et al. (1991).

China may be considered a composite continent of several paleo-plates delineated by major suture zones and fold belts. The "nucleus" of present day China centers on the Tarim and Sino-Korean (North China Block) cratons onto which several additional land masses have accreted (Gilder et al. 1991). Figure 1a shows the principal tectonic subdivisions, major suture zones and prominent crustal features of mainland China. Shown in Figure 1b are the modern political boundaries. Accretion to the northwest of the nucleus are marked by the Tien Shan-Tumen and Junggar-Xingan fold belt and the Late Paleozoic Junggar-Hegen suture to the Siberian craton (Gilder et al. 1991). Southeast and southwest of the Tarim and North China Block several stages of accretion have been identified, but the relative timing and emplacement of individual microplates are currently a focus of debate (Hsu et al. 1990; Huang and Opdyke 1991; Gilder et al. 1991; and others). To the southeast accretionary events are represented by the east-west trending Kunlun-Quinlin fold belt and by the Yangtze-Hunan Deformed Belt which is also known as the South China Block (Gilder et al. 1991). Southwest of the Kunlun-Quinlin fold belt are the Tangla Deformed Belt and Lhasa block, and since the Mesozioc the collision between the

4

Eurasian and Indian Plate has formed the Himalayan Mountains and Tibetan Plateau (Gilder et al. 1991; Shangyou 1991).

Between 100-107°E a roughly north-south seismogenic zone divides the whole country into two parts. In general, the eastern half of China is affected mainly by circum-Pacific tectonics and associated back-arc extension, while the western part is primarily affected by Tethys-Himalaya compressional tectonics (Yuan et al. 1986). China has an extensive historical data base of earthquakes due to the early interest in seismological study in 132 AD by Chang Heng and the invention of the seismoscope, the world's first seismometer. Fu (1991) tabulates Chinese earthquake data between 1900-1980 and statistically shows that the seismicity of eastern and western China is dominated by shallow focus intraplate earthquakes. These earthquakes occur 7 times more frequently in western China compared to eastern China and have a corresponding energy release ratio of 25:1 over the same time period.

Broad-scale information on crustal thickness and upper mantle velocity across China is shown in Figures 2-3 from geophysical maps given in Yuan et al. (1986) and Xingxin (1988). In Figure 2 the estimated crustal thickness along the eastern coast of China is 34-36 km and increases to 44-46 km in central China near Chengdu. West of Chengdu the Moho depth is inferred to be as much as 70 km beneath the Tibetan Plateau. These results are consistent with those of Zhao et al. (1991) who infers crustal thickness from modeling both regional Love and P_{nl} waves. Wu (1990) conducted an extensive analysis of local, regional and teleseismic data recorded at Chinese Kirnos and CDSN stations. For eastern China, Wu indicates P_n and S_n arrivals from events within 10° are generally weak and unclear, but in western China in the Xinjiang and Tibet regions, P_n and S_n may be quite prominent. In reference to Figure 3, relatively large P_n velocities are inferred for the Junggar and Tarim Basins and for the western third of the Sino-Korean Block. Much of this map is speculative, so that caution must be taken in extracting absolute values. However, the general trends are informative and we make use of those trends in this study.

2.1 BEIJING (BJI)

Station BJI is located in the Sino-Korean block in the northern end of the Jizhong Depression approximately 20 km north of Beijing. The station is installed in a hilly, mostly agricultural region in a subsurface vault at 3 meters depth on piers resting on gravel (Peterson *and others*—Kexin *and others*, 1987). Topography in the vicinity of the station is minimal. The Jizhong Basin is characterized by several NNE-SSW trending linear basement high and low graben structures composed of pre-Cenozoic rocks overlain by recent fluvial and lacustrine sediments (Zhao and Windley, 1990). Gilder et al. (1991) discuss two stages of rifting for the Bohia Gulf Region, the most recent being Late Cretaceous-Eocene until present with a heat flow average of 1.6 HFU (1 HFU $=1$ μcal cm^{-2}s^{-1}). Since the 1976 Tangshan earthquake, one the most devastating earthquakes (M$_b$= 7.8) in world history, several studies on the crustal structure in the vicinity of BJI have been published. Changquan and Shixu (1986) present and model seismic refraction data from two refraction profiles almost 200 km east of BJI. In reference to Figure 4, crustal P-wave velocities range from 6.1-6.4 km/s with a prominent low velocity zone located in the mid- to lower crust, and crustal thickness increases from SE toward NW over a transitional crust-mantle boundary. Exclusive of the low velocity zone Hellinger et al. (1985) infer a crustal thickness of 35-38 km southeast of BJI. Shedlock and Roecker (1987) infer an upper-crust P-wave velocity at 6.02 km/s between 0-15 km, 6.5 km/s between 15-35 km and an upper mantle velocity of 7.9 km/s east of BJI. They also infer a lower crustal low velocity zone between Beijing and Tangshan at 20-35 km depth as well as Vp/Vs ratios of 1.73-1.77 in the crust and 1.8 in the upper mantle. Yuan et al (1986) estimate a 36 km thick crust beneath BJI.

2.2 KUNMING (KMI)

Station KMI is located along the southwestern edge of the Yangtze or South China Block in the southern Yunnan province. The seismometers are installed in a 30 meter long limestone tunnel 27 meters deep and are within 5 km of some major industrial plants (Peterson *and others* —Kexin *and others*, 1987). Topography around KMI is moderate with elevations between

1500-3000 meters. Paleomagnetic evidence given in Fang et al (1989) suggests that the Yunnan province is composed of at least two accretionary blocks (eastern and western) and that either the Red (Yuan) River or Lancang (Mekong) River fault zones, ~200 and ~300 km west of KMI respectively, represent a major paleo-suture of the Yunnan and South China Block. Baiji and Ning (1987) delineate a 'central' Yunnan block bounded by the Red River fault to the south, the Xiaojiang fault to the east, and the Jianchuan-Lijiang fault to the north shown in Figure 5. Using a network of 14 seismic stations and KMI as the 'standard station' Baiji and Ning (1987) use teleseismic P-wave residuals to infer a higher velocity upper mantle beneath the central block (0.45 km/s faster) than the surrounding region. The results of a deep seismic sounding profile recorded along the main road from Malong, about 100 km NE of KMI, through Kunming to Simao ~300 km southwest of KMI is discussed in Qizhong et al. (1985). Their model estimate east of KMI (Figure 5) indicates a 45 km thick 5 layer crust with an average velocity of 6.3 km/s over an upper mantle of ~8.2 km/s. Yuan et al. (1986) estimate a total crustal thickness beneath KMI between 48-50 km.

2.3 LANZHOU (LZH)

Station LZH is located on the northeastern margin of the Tibetan Plateau along the Qinling fold belt in the Gansu Province. The seismometers are located on the outskirts of Lanzhou City in a buried surface vault built on loess deposits (Peterson *and others*—Kexin *and others, 1987*). Topography in the vicinity of LZH is characterized by smooth rounded slopes with narrow, steep walled modern stream valleys at elevations of 2000-3000 meters (Burchfiel et al. 1991). Several large ($M_b > 6$) earthquakes have occurred in this area with the largest being the 1920 Haiyuan event that had an associated 220 km surface rupture (Burchfiel et al. 1991). Shown in Figure 6 (top) are the Quaternary active faults and Cenozoic basins about Lanzhou. Motion along these faults suggest the Tibetan Plateau is extending toward the northeast. Lanzhou overlies a zone of high electrical conductivity in the upper mantle and local hot springs provide source regions for high-temperature wells about Lanzhou (Xingxin 1988). Shown by contour plot in Figure 6 from

Xingxin (1988) station LZH appears to overly a southwest dipping Moho at 54 km depth. Liang and Li (1991) infer 51-52 km thick crust using gravity data and show a similar dipping nature of the crust-mantle boundary beneath LZH. Yuan et al. (1986) infers a 50-54 km thick crust (Figure 2) beneath LZH.

2.4 HAILAR (HIA)

Station HIA is the northern most CDSN station located on the Sino-Korean Block in the Nei nenggu Province outside Hailar City adjacent to the Hailar River. The seismometers are located in a vault within a 12 meter long tunnel at 15 meters depth in an andesite hill (Peterson *and others*—Kexin *and others*, 1987). Topography is minimal to hilly with elevations changes between 200-500 meters. No seismic refraction or reflection survey results in the vicinity of HIA were found in the literature. Surface wave models of the crust and upper mantle derived from several Kuril earthquakes recorded by Kirnos stations WMQ, KTA, and BTO (Rui et al. 1981), provide initial estimates beneath HIA shown in Figure 7. Although these results are based on one azimuth and three paths Rui et al. (1981) infer a crustal thickness of 46 km near HIA (model 3) with an average velocity of 6.4 km/s. The upper mantle P velocity is between 7.8-8.0 km/s and all models indicate a step in velocity at approximately 23 km depth. Yuan et al. (1986) shows a 39 km thick crust beneath HIA (Figure 2), but the trend of increasing Moho depth from station MDJ toward HIA is consistent in both studies.

2.5 MUDANJIANG (MDJ)

Station MDJ is the eastern most CDSN station situated in the Sino-Korean Block of the eastern Heilongjiang Province approximately 300 km northwest of the Russian port Vladivostok. The seismometers are installed within a vault toward the end of a 60 meter long tunnel at 50 meters depth in granite outside the city of Mujanjiang (Peterson *and others* Kexin *and others*, 1987). No seismic refraction or reflection results were found in the literature for the MDJ area. Surface wave results given by Rui et al. (1981) shown in Figure 7 infer a 42 km thick crust

(model 1) with a slightly lower upper mantle velocity ~7.9 km/s beneath station MDJ. As discussed in the observations for station HIA, station MDJ also shows a step in P velocity at ~23 km depth. Yuan et al. (1986) indicate a 35 km thick crust (Figure 2) beneath MDJ.

2.6 URUMQI (WMQ)

Station WMQ is located between the Junggar Basin and the Tarim Basin along the eastern Tien Shan of the Xinjiang Province. The sensors are installed in a vault at 6 meters depth tunneled into a sandstone hill on the outskirts of Urumqi City (Peterson and others — Kexin and others, 1987). No seismic refraction and/or reflection survey results in the vicinity of WMQ were found in the literature. Yuan et al. (1986) infer a crustal thickness of approximately 46-50 km in the vicinity of WMQ.
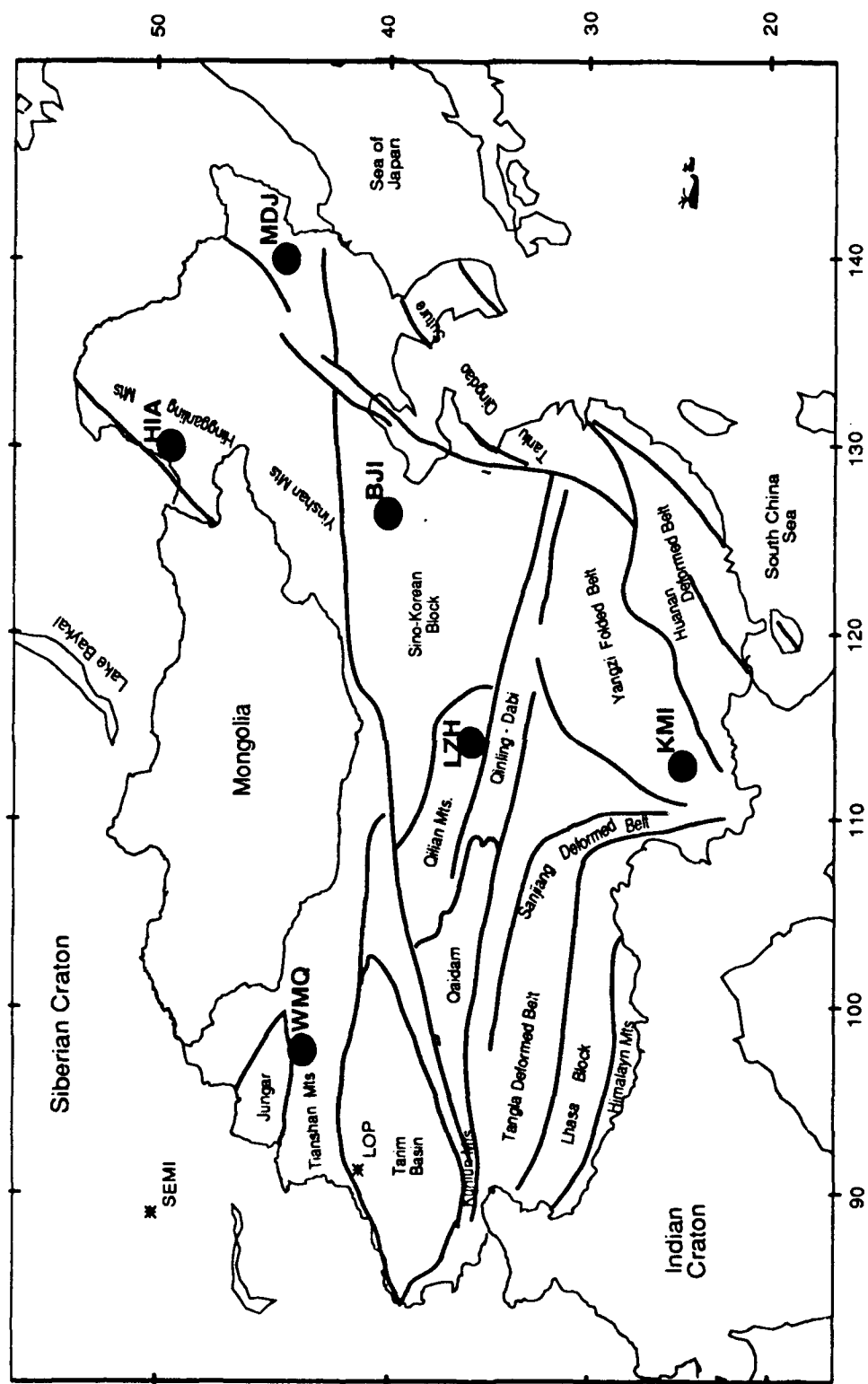
Figure 1a. Mercator projection of China showing the major physiographic features and CDSN station locations. From east to west these stations are: (MDJ) Mudanjiang, (HIA) Hailar, (BJI) Beijing, (KMI) Kunming, (LZH) Lanzhou, and (WMQ) Urumqi. Figure compiled from (Gilder et al., 1991; Hsu et al., 1990; and Shangyou, 1991)

10
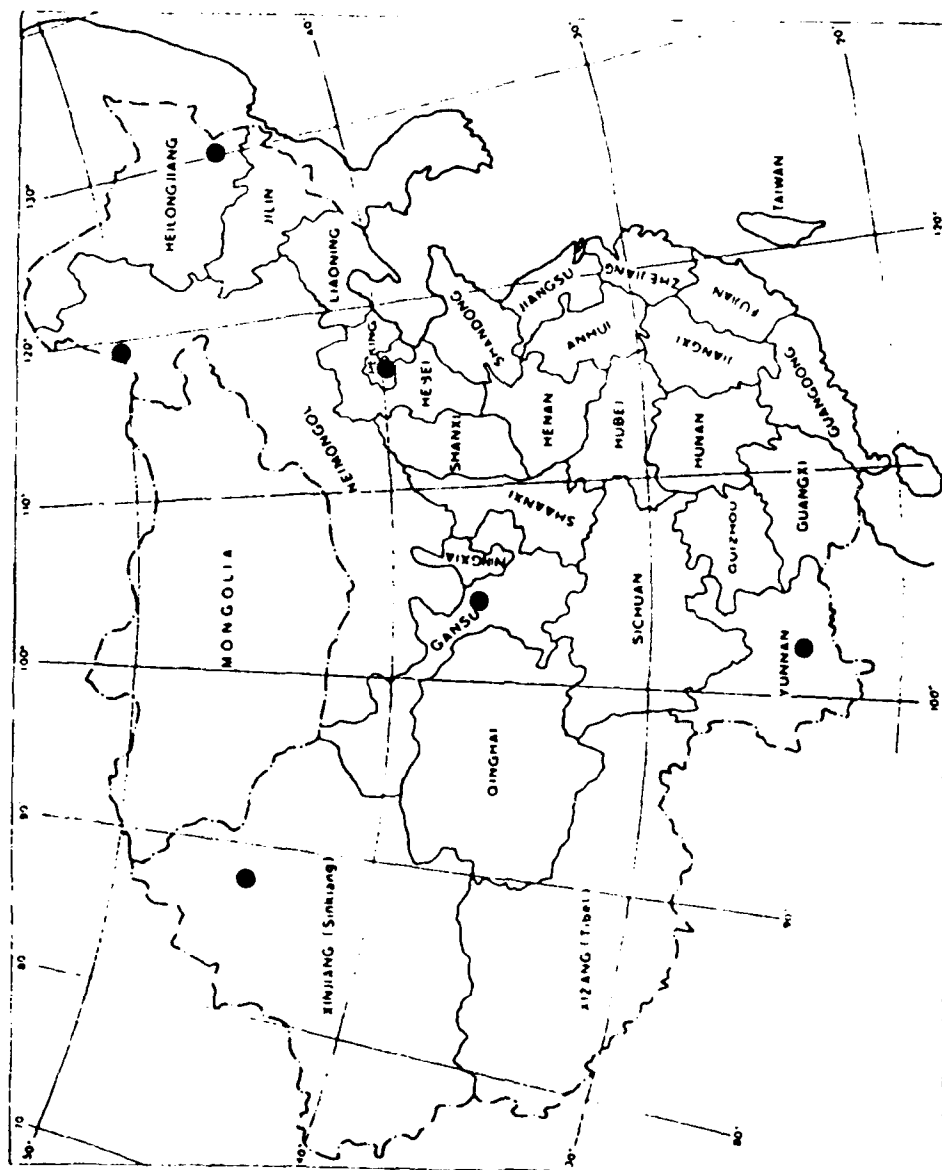
Figure 1b. The Provinces of China (Hsu et al. 1990) and CDSN locations.

11
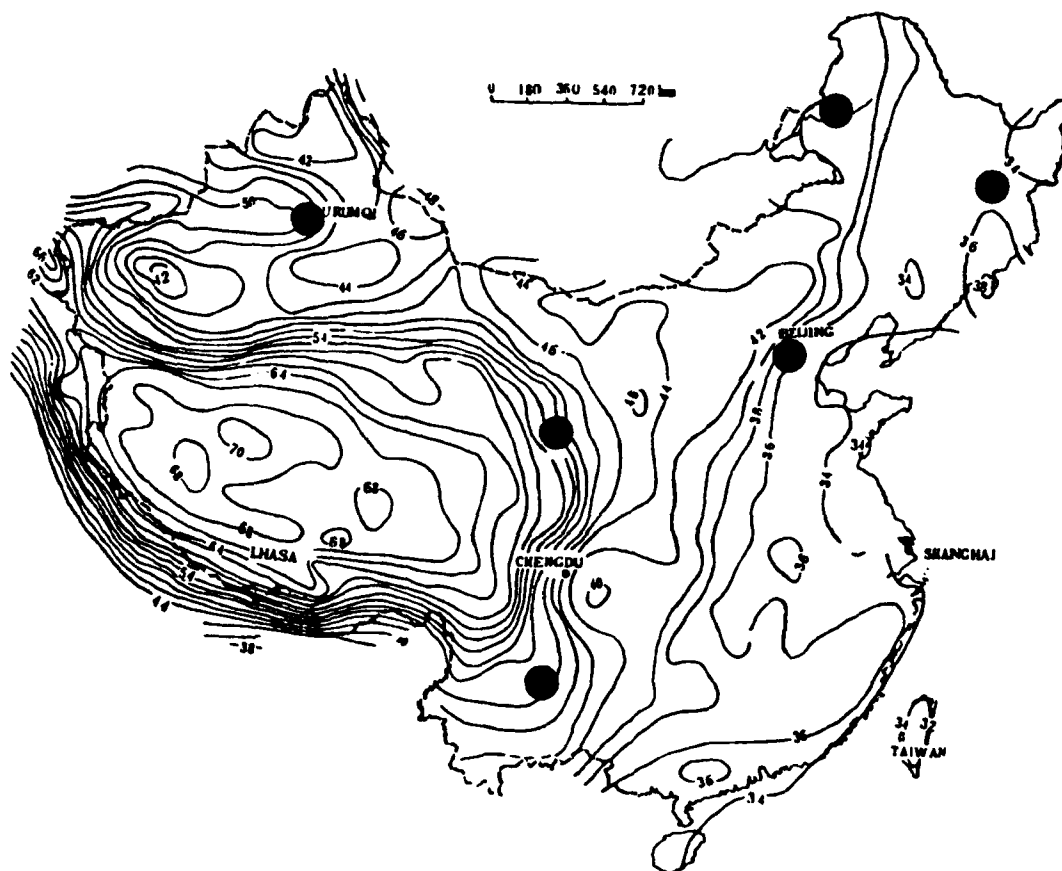
Figure 2. Contour map of Moho depth in kilometers across China, from
Yuan et al. (1986).
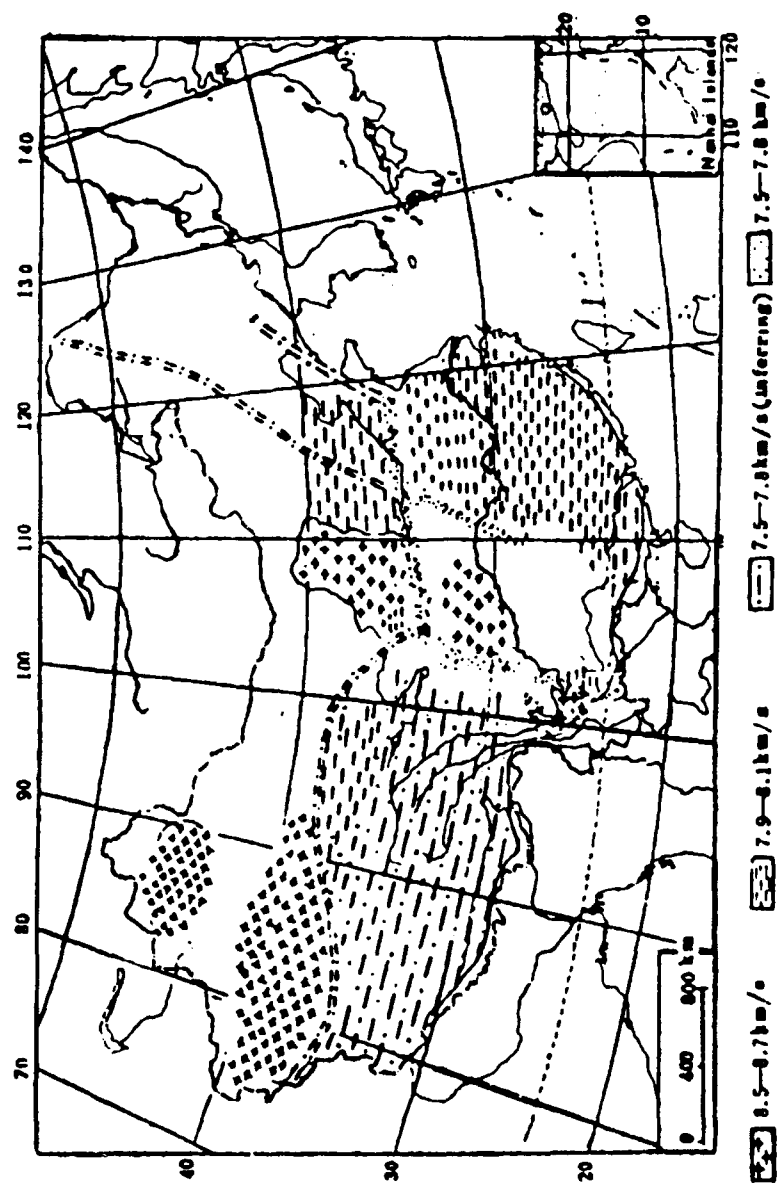
Figure 3. Pn velocity distribution across China inferred by Xingxin (1988).

13
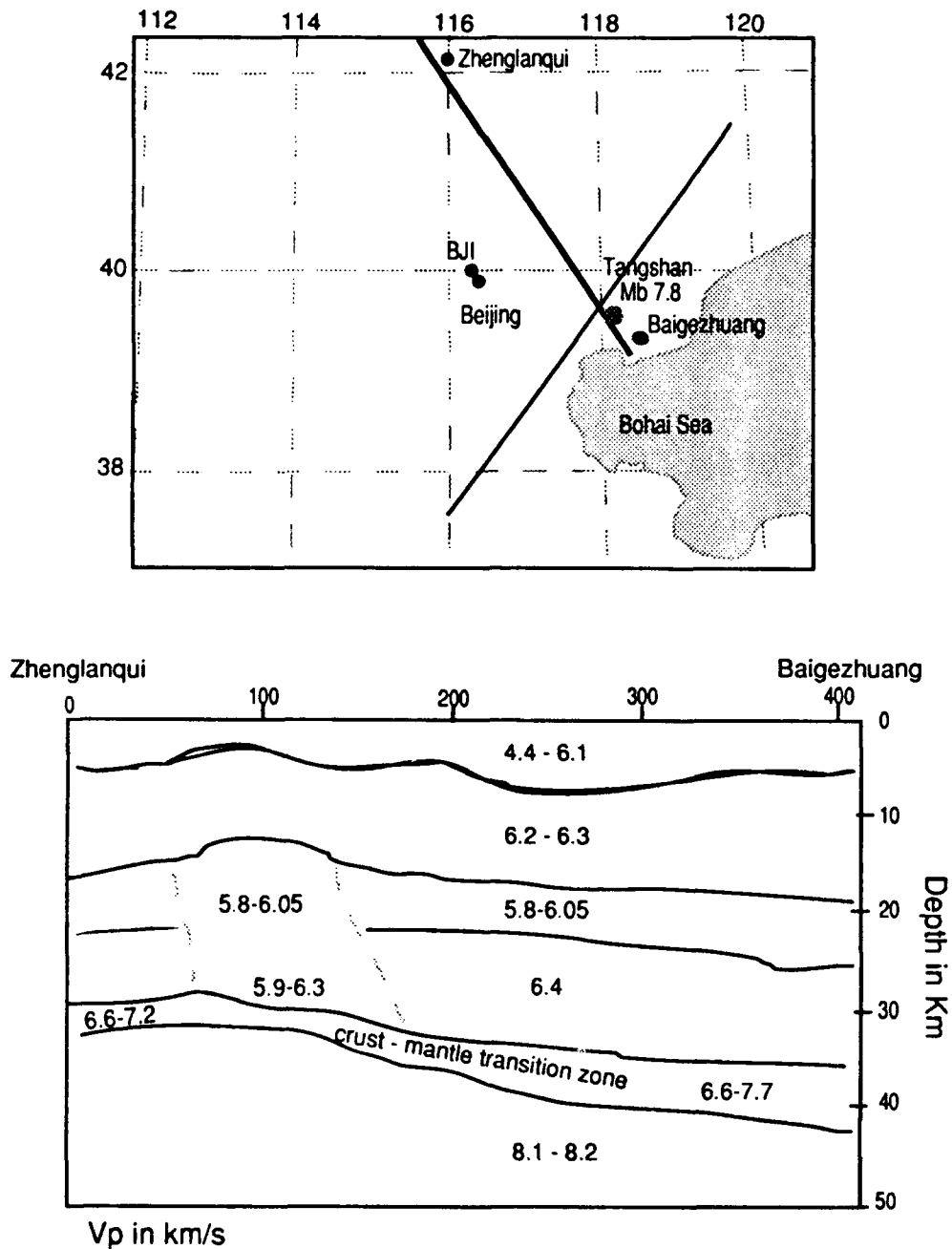
Figure 4. Refraction profiles with respect to station BJI (top) and the inferred velocity model (bottom) given by Changquan and Shixu (1986) for the Zhenglanqi (NW) to Baigezhuang (SE) profile. A low velocity zone in the mid- to lower crust is also suggested by Shedlock and Roecker (1987) for this area.
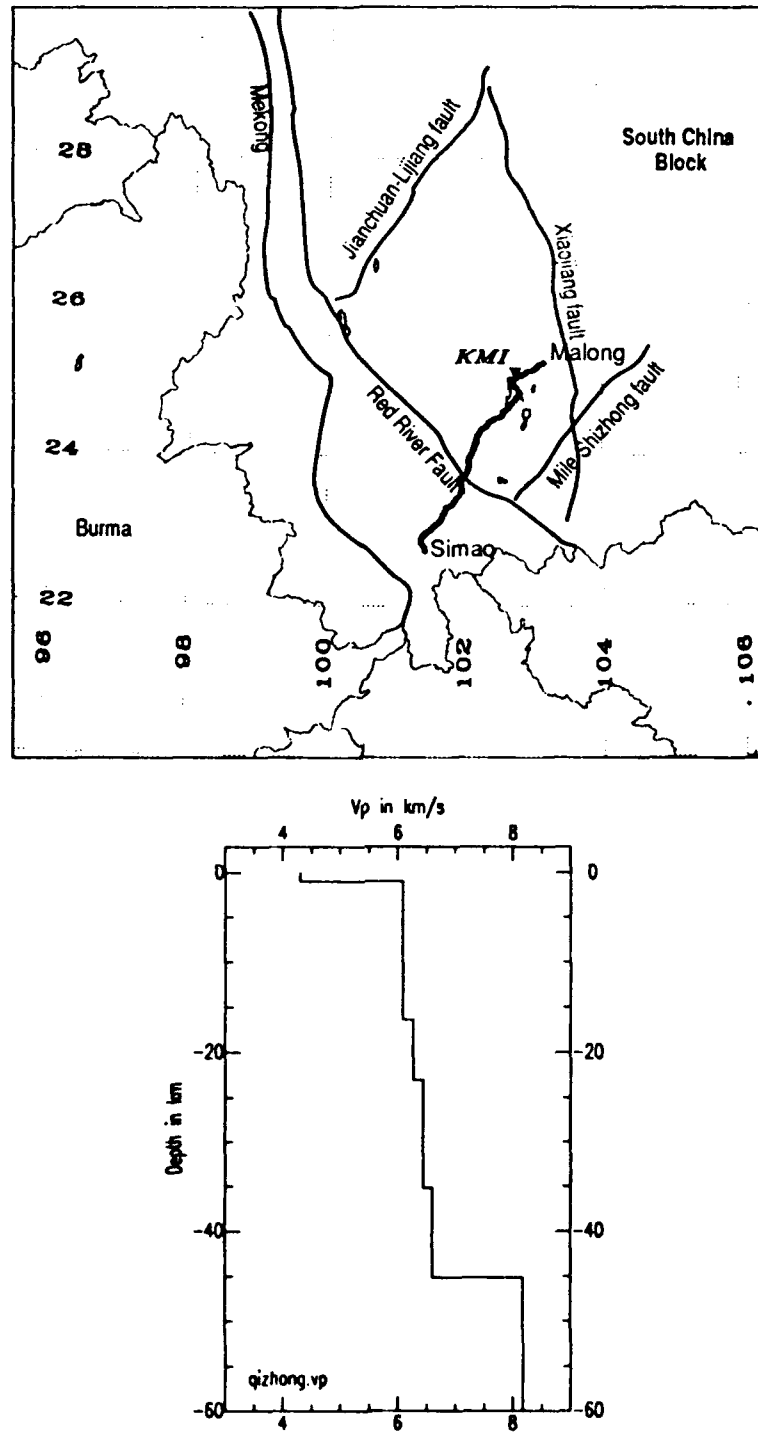
Figure 5. Tectonic map of the Yunnan-KMI-South China block region modified from
Baiji and Ning (1987) (top); and P-wave velocity model from Qizhong et al. (1985)
for the Simao-Malong profile, south of Malong and east of station KMI.

15
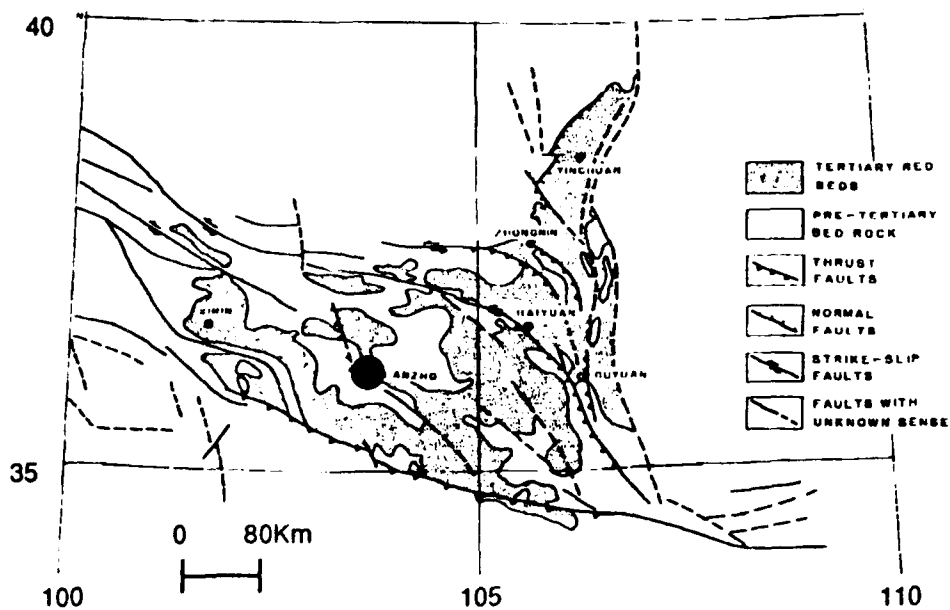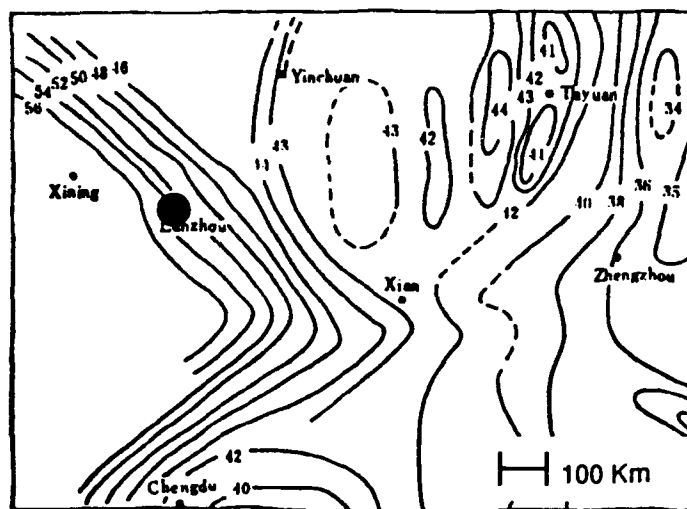
Figure 6. Depth to top of crust-mantle boundary around Lanzhou (LZH)
(top) from Xingxin (1988). Distribution of Quaternary active faults
and Cenozoic basins (bottom) from Burchfiel et al. (1991).

16
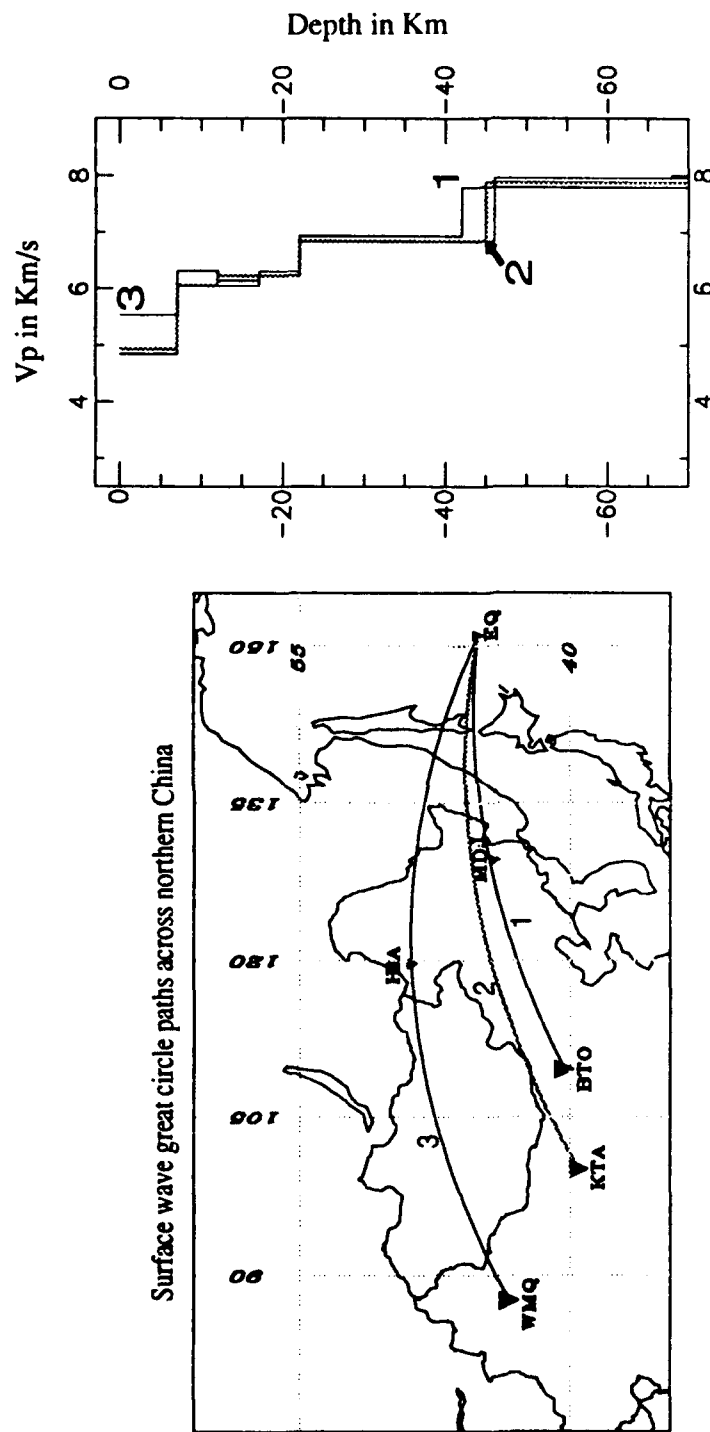
Figure 7. Great circle arc paths from a Kuril event (EQ) to Kirnos stations WMQ, KTA, and BTO (left), and the corresponding velocity models (right). This Figure is modified from Rui et al. (1981).

3.0 RECEIVER FUNCTIONS

The response of the crust and upper-mantle to an incoming teleseismic P wave may be represented with a convolutional model:

$$z(t) = e_z(t) * s(t) * i(t) \tag{1}$$

where $z(t)$ represents the vertical ground motion, $e_z(t)$ represents the vertical component response of the local structure to an incoming plane P wave and includes the effects of laterally homogeneous features and laterally varying structures, $s(t)$ represents the apparent source-time function and includes both near source and lower mantle propagation effects and $i(t)$ represents the recording instrument response. For a single station receiver function study the assumption of a laterally homogeneous structure is usually necessary. The effects of lateral heterogeneity and dipping structure can be examined through the variation of the receiver response as a function of the incident P wave azimuth Langston (1977a), Owens and Crosson (1988) and this study. The horizontal radial component of the response of a laterally homogeneous structure to an incoming plane P-wave consists of the direct P arrival followed by P-to-S converted and reverberating phases and zero tangential response.

The effects of the source and lower mantle propagation must be removed to isolate the local earth structure. Shown in Figure 8 is one of several characteristic teleseismic events from the Fiji area recorded at CDSN station BJI. The source and lower-mantle propagation effects are common to all three components of motion, and with matched instruments, a receiver function is defined as the time series resulting from the deconvolution of the vertical component of motion from the horizontal component of motion. Below we describe Langston's (1979) source equalization procedure with the modification of (Ammon 1991). Let the radial component of motion be represented by $r(t)$, the vertical by $z(t)$, the radial receiver function by $h(t)$, and the corresponding Fourier transforms by $R(\omega)$, $Z(\omega)$, and $H(\omega)$ respectively. The time domain receiver function is defined by

$$r(t) = z(t) * h(t) \tag{2},$$

such that in the frequency domain we have

$$H(\omega) = \frac{R(\omega)}{Z(\omega)}$$ (3).

To reduce the effects of noise and numerical instabilities the deconvolution is performed in the frequency domain using a minimum allowable denominator described by

$$H(\omega) = \frac{R(\omega) \, Z^*(\omega)}{\phi(\omega)} \, G(\omega),$$ (4)

where

$$\phi(\omega) = max \left\{ Z(\omega) \, Z^*(\omega), \, c \cdot max \left\{ Z(\omega) \, Z^*(\omega) \right\} \right\}$$ (5).

The constant c represents the minimum amplitude allowed in the denominator of (5), * indicates complex conjugation and

$$G(\omega) = \xi \, exp \left(\frac{-\omega^2}{4 \, a^2} \right)$$ (6)

The constant ξ normalizes the gaussian filter to unit amplitude in the time domain to produce smooth estimates of (4) while the constant "a" determines the width of the gaussian filter. A gaussian of 2.5 passes frequencies up to ~1.2 Hz while a gaussian of 1.0 passes frequencies up to ~0.4 Hz. Filling spectral holes in the denominator to avoid division by very small numbers changes the overall amplitude of the receiver function. Once a suitable water-level parameter is chosen the true receiver function amplitude is obtained by adding the following constraint to the equalization. The deconvolution of the vertical component from itself using the same water-level parameter as in the horizontal component equalizations produces a time series with a maximum amplitude of one (Ammon, 1991). True amplitude receiver functions preserve the relative

19

amplitude of the converted phases to the direct P arrival. The receiver function ray diagram in Figure 9 shows the response of an incident plane P-wave after propagation across layer 'h' determined with the technique given in Kennet (1983). The use of a plane wave approximation is justified because a teleseismic P wave has a relatively large constant phase velocity. For a horizontally layered structure each P to S conversion has the same horizontal slowness. The true amplitude synthetic receiver functions computed for the teleseismic range at 10° intervals (Figure 9) show that the amplitude falloff and moveout of multiple converted phases as epicentral distance increases is easily observed. These fundamental characteristics are observed in the CDSN data and are shown in Section 5.

Of primary concern is the contamination of a radial receiver function with waves generated by the interaction of the P-wavefield and lateral velocity variations. Differences between stacked azimuthal clusters may be attributed in part to variations in the local structure as a function of azimuth and in part by contamination with off-azimuth arrivals. The amount of scattering is represented by the observed motion on the tangential receiver function. Unlike interactive trial-and-error modeling the inversion scheme is unable to qualitatively judge the importance of a given arrival in a receiver function. Mangino et al. (1992) demonstrate a pitfall in interpretation of a receiver function inversion in the presence of significant scattering. To avoid potentially biased inversion results from small scale (relative to wavelength) heterogeneities we initially analyze CDSN data using a gaussian filter of 1.0. Longer period data tend to smooth over the effects of small scale crustal heterogeneities, so we should expect to obtain simpler and potentially less biased solution models. When multiple stacking suites are available we use those with the best signal-to-noise ratio.

August 10, 1990; Fiji Islands: DELTA = 85°, BAZ =120° Depth = 373 km
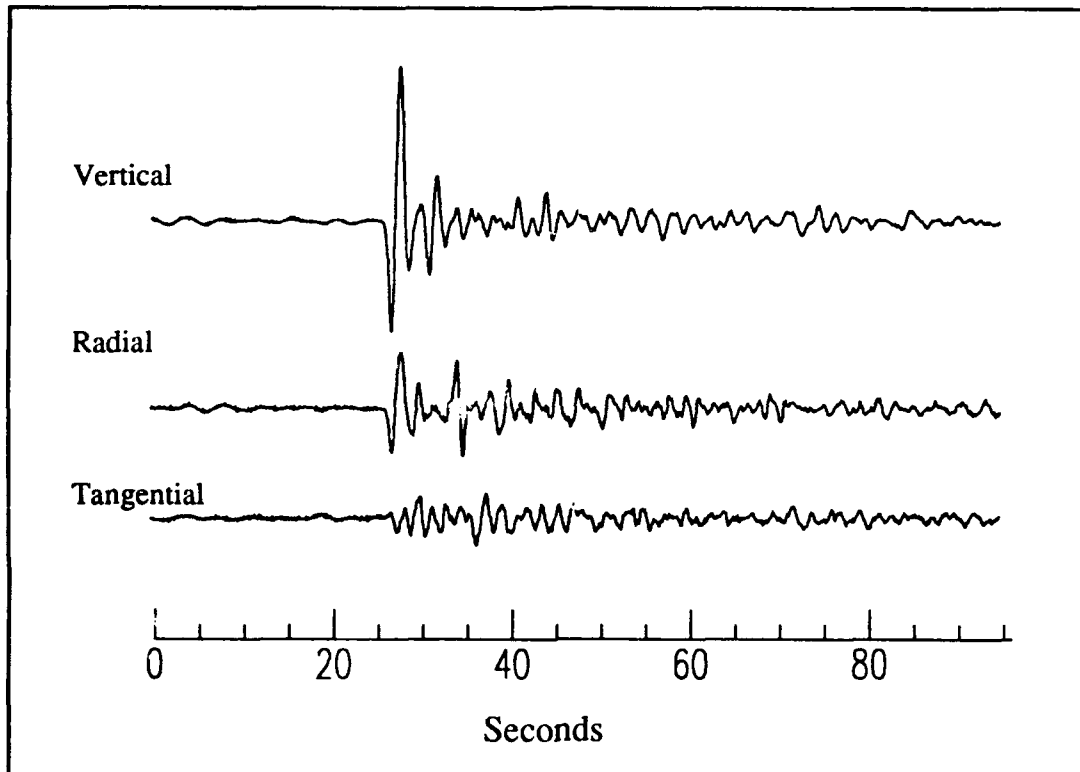
Figure 8.   An example waveform from the 20 samples/second broadband data stream of seismograph station Baijatuan, Beijing (BJI) one of 6 CDSN stations providing data to the Global Digital Seismic Network.   Above is the first 60 seconds of data normalized to the vertical component. The observed ground motion corresponds to an incident teleseismic P-wave from the Fiji region.
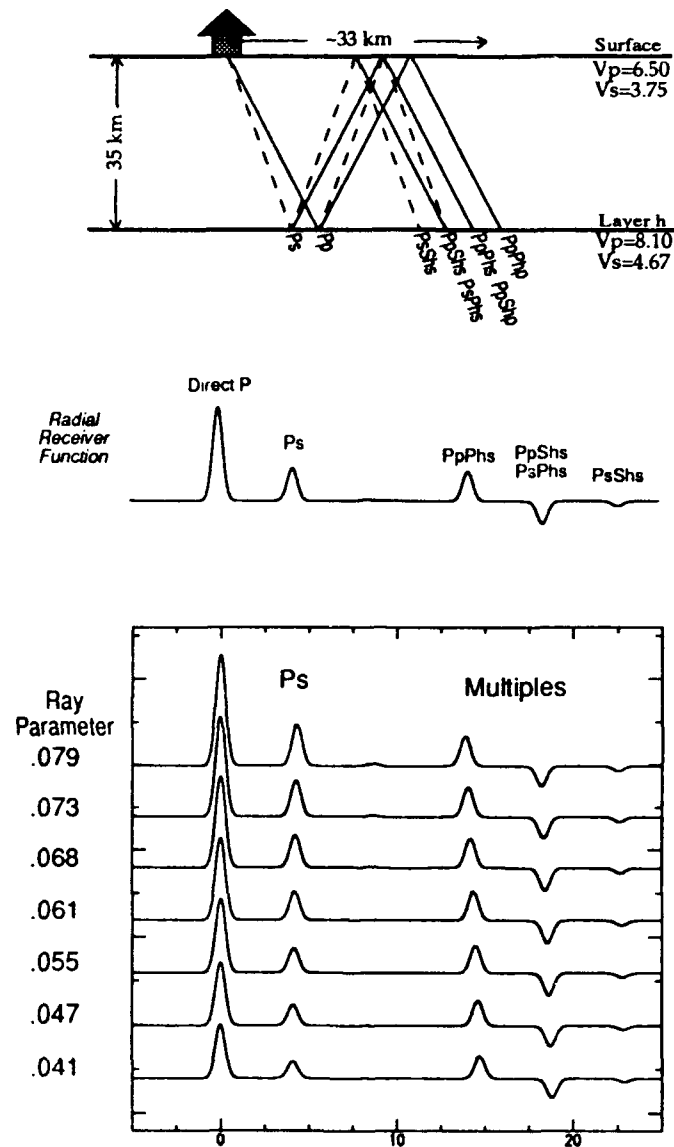
Figure 9. Receiver Function Ray Diagram (top) and corresponding receiver function (middle). Except for the first arrival all upper case letters denote down-going waves and all lower case letters denote up-going waves according to Bath and Steffanson (1966). Shown below are receiver functions from the same model at 30° to 90° epicentral distances at 10° intervals.

4.0 THE DATA

The CDSN became operational with stations BJI, LZH and WMQ during mid-October 1986. By mid-March 1987 stations KMI and HIA were 'on-line' and toward the end of 1987 station MDJ was working. Most stations are co-located at previously established fiducial sites that bear the same name (Peterson *and others*—Kexin *and others,* 1987). Three additional CDSN stations are operational (Qiongzhong (QIZ), Enshi (ENH) and Sheshan (SSE)) but do not routinely report data to the international seismological community. Deployment of new stations are planned for the Lhasa, Hotan and Golmud regions (Peterson *and others*—Kexin *and others,* 1987). All CDSN station coordinates are listed in Table 7.

In this report we examine the 20 sps BB/BH STS-1 data band. The CDSN records ground motion at sample rates of [0.1, 1.0, 20, 40] samples per second (sps) on four discrete bands defined respectively as: VLP (very long period), LP (long period), BB, BH (broadband) and SP (short period). Three types of seismometers are deployed. The BB, LP and VLP signal bands are recorded with a triaxial set of force-balance Streckeisen STS-1 seismometers. The SP band is recorded with China Institute of Geophysics DJ-1-SP and Geotech KS-3600 borehole seismometers. Station clocks are synchronized to a common time code broadcast by station BPM located in central China. Shown in Table 9 the sensitivity for each BB data channel is nearly identical at all stations.

All 'potentially useful' teleseismic events between 1986-1991 with a body wave magnitude of 5.8 or greater were retrieved from the archive. A non-potential useful event is defined as any teleseismic event recorded at a given station within the coda of a previous local, regional or teleseismic event. Not all events were within teleseismic distance of all stations and all potentially useful events were not always recorded at every station. Shown in Figure 10 are the station locations with the number of teleseismic events (1986-1991) recorded by each station with the 'potentially useful' constraint included in the tabulation. In general, the northeast and southeast quadrants contain the most data, given the location of mainland China with respect to the circum-Pacific seismogenic zones, while source regions for the southwest and northwest

23

quadrants are relatively sparse. Tables 1-6 contain the pertinent source parameters as listed in the Preliminary Determination of Epicenter Bulletins.

Once in-house all data were converted into SAC format (Seismic Analysis Code; Tapley et al. 1991) and are shown utilizing SAC graphics subroutines. For reference a flow chart summarizing procedures used throughout this report is shown Figure 11. All data were corrected for sensitivity and sorted into azimuthal quadrants. Quadrants that contain several clusters of events were binned according to a common back azimuth and epicentral distance. Throughout this procedure events with emergent first arrivals are discarded. Individual events within each bin were cut into 60 second record lengths with 30 seconds of pre-signal noise. Events without 30 seconds of pre-event data were cosine tapered and zero padded. Those events with impulsive first arrivals are selected with onset picked at the positive peak amplitude first arrival on the vertical component. The radial component is defined as the positive direction from the source pointing toward the receiver. The tangential component is defined as 90° clockwise from the positive radial direction. Each event was source equalized with the procedure discussed in Section 3 and those events within each bin with stable deconvolutions are stacked. The variance of the stacked data provide the ± 1 standard deviation bounds used to constrain acceptable model synthetics in the following sections of this report.
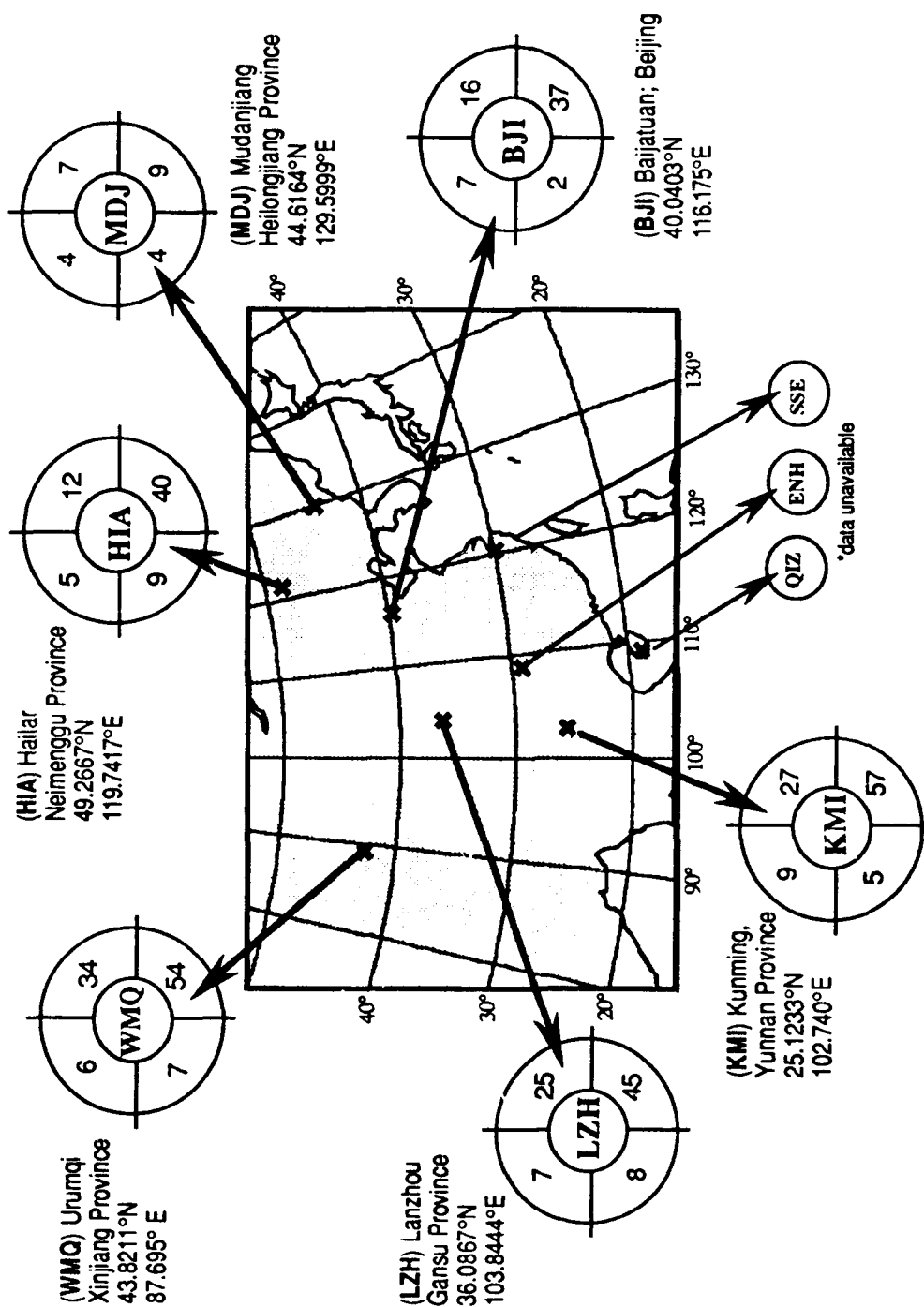
Figure 10. Distribution of all teleseismic events not arriving within the coda of a local, regional or previous teleseismic event with respect to and recorded by each CDSN station, available in the archives for the years 1986 until 1991.

(MDJ) Mudanjiang
Heilongjiang Province
44.6164°N
129.5999°E

(BJI) Baijatuan; Beijing
40.0403°N
116.175°E

(HIA) Hailar
Neimenggu Province
49.2667°N
119.7417°E

*data unavailable

(WMQ) Urumqi
Xinjiang Province
43.8211°N
87.695° E

(LZH) Lanzhou
Gansu Province
36.0867°N
103.8444°E

(KMI) Kunming,
Yunnan Province
25.1233°N
102.740°E

25

```
Search PDE's;                  Access archives and convert various
assemble data set.            formats into SAC format.


Preliminary data processing   Process all traces and correct for
                               sensivitity. Sort into bins for each
                               station for each azimuth.


Compute receiver functions &  Compute receiver functions; determine
stacking suites; evaluation.  optimum stacking suite(s).


  MDJ  HIA  KMI  LZH  WMQ  BJI  Review previous works;
                                obtain starting models; set
                                up inversion parameters.


Waveform Inversion            Inversion of stacking suites; evaluate
                              results.


Results & Discussion
```

Figure 11. Flowchart of processing steps used in this report.

26

5.0 RECEIVER FUNCTION OBSERVATIONS

As shown in Figure 9 the model synthetics clearly show that the overall amplitude falloff and moveout of the first order multiples can be clearly observed over tens of degrees. The availability of several stacks within a narrow azimuthal range provides an opportunity to observe these characteristics in the CDSN data. In Figures 12-18 and the following sections we show the response and discuss our observations for each CDSN station. We discuss the stacked radial and tangential receiver functions with the best signal-to-noise ratio for quadrants that contain several bins and we also compare stacks within the same quadrant. To facilitate comparison of arrivals common to all azimuths, the radial and tangential receiver functions are shown normalized to the radial component within each quadrant and aligned side by side. Direct comparison between arrivals on the radial to the tangential response indicate t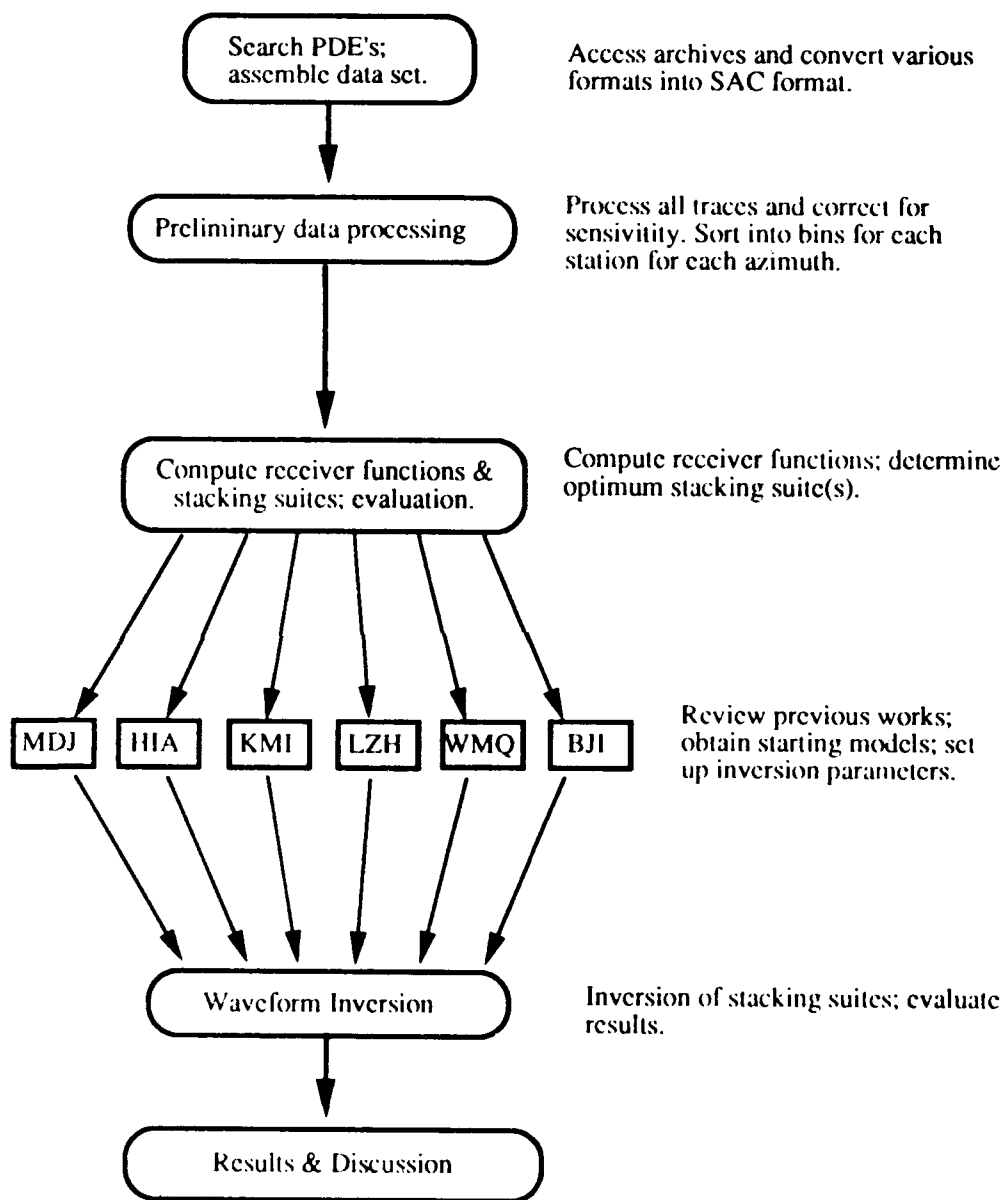he variation in time of scattered energy to the energy polarized in the vertical-radial plane. As a rule of thumb receiver functions sample a lateral distance from the station roughly equal to the horizontal distance traveled by the deepest multiple (typically from the crust mantle boundary) recorded within the first 30s after the direct P arrival.

5.1 BJI, BEIJING

The distribution of data and the 5 data bins available for BJI are shown in Figures A1-A6. Data from the northeast quadrant consists of 2 event clusters at 45° and 58° epicentral distance with an azimuthal separation of 11°. Southeast of BJI bins at 74°and 85° each contain several events. Three receiver functions were sufficient to form a single bin for data arriving from the west.

Shown in Figure 12 are the BJI receiver functions. Common to all azimuths is a large coherent pulse of energy on the radial response arriving at 5-5.3s after the direct arrival. After 7-8s both radial and tangential responses are significantly different. The BJI-NE radial receiver function appears relatively simple with a large pulse of energy at 5s after the direct arrival followed by lower energy arrivals. Tangential motion from 0-3s show a moderate level of

energy with a positive first motion followed by energy close to but not exceeding the amplitude on radial. The BJI-SE response is complicated. From 7s to about 18s the radial response contains several large amplitude arrivals while the tangential response has a small negative motion at onset followed by arrivals that exceed the radial after 6s. The pronounced scattered energy on the tangential component prohibits a confident interpretation of this azimuth in terms of a one-dimensional structure. The BJI-NW radial response has three coherent pulses of energy. The pulse at 5.3s is followed by a large positive motion at 15s and an equally prominent negative motion at 20s. The tangential response shows moderate energy from onset to 10s but does not exceed the radial. After 10s the tangential response is minimal relative to the radial.

One interpretation of the arrival at 5-5.3s common to all azimuths is a Ps conversion at the crust-mantle boundary. Furthermore, the similarity of this arrival about the station suggests that the region of the Moho structure sampled by this Ps phase is laterally consistent about the station. Motion on the NW response between 14-20s is consistent with PpP_hs and PpS_hs multiples from the Moho. From these observations only the northeast and northwest azimuths shows promise for obtaining reliable one-dimensional model estimates of the crustal structure.

5.2 KMI, KUNMING

Station KMI has 8 bins shown in Figures A7-A14. Data from the northeast contains 2 event clusters at approximately 63° and 75°. The southeast quadrant consists of 3 bins at approximately 56°, 75°, and 88°. From source regions to the west two bins are possible with the northwest quadrant containing several events.

Shown in Figure 13 are the KMI receiver functions. In general arrivals from the east are similar and arrivals from the west are similar, but between east and west there are significant differences in amplitude and number of arrivals. The northeast tangential response has large energy immediately from onset until about 20s. The radial response contains large energy pulses at 5-5.2s and between 10s to 20s that is in phase with motion on the tangential. Large amplitude tangential arrivals preclude interpretation of this azimuth in terms of a one-dimensional response.

The KMI-SE response is also complex. Tangential motion through the initial 15s is significant but low in amplitude compared to the radial component. Between 5-8s the southeast radial response contains the largest energy arrival observed at this station, followed by a second packet of (multiple?) energy between 11-18s. The KMI western receiver functions are lower amplitude after about 10s compared to the receiver functions from the east and motion on the radial components appear to be polarized in the vertical-radial plane. These observations are consistent with a one-dimensional response but does not preclude an alternate structure.

5.3 LZH, LANZHOU

Station LZH contains 7 event clusters shown in Figures A15-A22. The northeast quadrant contains 2 bins at 55° and 68° with an azimuthal separation of 14°. The southeast quadrant contains 4 bins at 46°, 62°, 77° and 93° consisting of 5, 4, 7 and 4 events respectively. This coverage is the best of any station quadrant. West of LZH a single azimuthal cluster consisting of 4 events is possible.

Shown in Figure 14 are the LZH receiver functions. Although the radial and tangential response are different for each backazimuth, all radial components show a moderately coherent pulse of energy between 6-7s after the direct arrival. The NE tangential response contains large energy from onset to about 12. The SE radial response contains a large energy packet between 2-8s after the direct arrival. Between 8-14s the tangential motion is large but does not exceed the radial response. Shown in Figure 15 spanning almost 50° great circle arc are all LZH-SE radial and tangential receiver functions. Differences in each bin suggest a difference in crustal structure over the 35° azimuthal range. As the ray parameter decreases the radial response approaches the energy level on the tangential response. The amplitude fall off of the 5-7s pulse and moveout of the pulse between 13-14s (inset) are consistent with a conversion from a common interface beneath LZH.

The LZH-W response is relatively simple compared to the east. The packet of energy at 5-8s on the radial component is the only clearly distinguishable arrival. The western tangential component has the lowest energy of all azimuths and does not exceed the radial response.

5.4 HIA, HAILAR

Station HIA contains 6 azimuthal clusters shown in Figures A23-A30. The northeast quadrant consists of one bin at 50° while the SE quadrant is well sampled by 3 bins at 55°, 62° and 73°. Data arriving from the west can be grouped into 2 bins at 34° and 50°.

Shown in Figure 16 are the HIA radial and tangential receiver functions. In general, from the direct P arrival to about 8-9s the overall response is very similar. The pulse between 4-5s followed by a smaller arrival between 6-7s is common to all radial components. Only the SE radial response contains an arrival between 13-19s that is consistent with a multiple from the same interface generating the 4-5s arrival. Tangential energy is minimal with respect to the radial for all azimuths. All HIA-SE stacks are shown in Figure 17. The strong similarity of the radial response for each bin indicates the crustal structure is similar over the azimuthal range sampled. The decreasing overall amplitude and the moveout of a suspected PpP_hS multiple (Figure 17) as a function of epicentral distance is consistent with model synthetics shown in Figure 9. Moveout of a multiple from a common interface can provide additional constraint to the velocity structure beneath HIA.

5.5 MDJ, MUDANJIANG

Station MDJ was the last CDSN station designated to provide data to the GDSN to become fully operational in 1987. Subsequently MDJ data have been sporadic in the archives. Shown in Figures A30-A33 are individual MDJ receiver functions. In particular events 9212 (SE) and 9213 (SW) are consistent with a one-dimensional response. Overall, with only a handful of events distributed about the station we believe that an analysis for the receiver structure beneath MDJ is unwarranted at this time.

5.6 WMQ, URUMQI

The WMQ data contains 5 possible bins shown in Figure A35-A40. The northeast quadrant consists of a single well populated bin at 63°. The southeast quadrant contains two bins at 63° and 75°, separated by 21°. Data arriving from western sources yield one bin at 50° in the southwest and a second bin at 38° in the northwest quadrant.

Shown in Figure 18 are the WMQ receiver functions. The overall difference in response indicates a laterally varying velocity structure beneath the station. Motion on the NE tangential is the largest while motion on the SE tangential is the least for all azimuths. Close examination of the radial response reveals an offset of the direct arrival for all azimuths. This observation coupled with a significant variation in polarity within the initial 0-4s of the tangential response suggest the presence of a dipping structure beneath WMQ. Owens and Crosson (1988) show that the time lag of the direct arrival on the radial response is related to the traveltime of a Ps conversion propagating through the up-dip or down-dip direction, provided that velocity increases with depth. A Ps conversion traveling up-dip has the largest delay because of a longer travel path through a slower medium. Langston (1977) shows that the initial motion on the tangential response is reversed across a line parallel to the dip direction.

In light of these previous studies to constrain the suspected dipping structure we measured the time lag for all radial receiver functions and examine all tangential receiver functions for polarity reversals as a function of backazimuth. Shown in Figure 19a are the observed time-lags measured from all stable WMQ radial receiver functions. A consistent pattern with an average delay of 0.8s is clearly present between 310° to 15°. Figure 19b shows the tangential response about WMQ. Arrows indicate the backazimuth range over which we can constrain a line parallel to the dip direction. The time delays of the direct arrival plus the polarity reversals are consistent with a north-northwest dipping structure beneath the station. The effects of this feature are most likely diverting converted shear wave energy out of the vertical-radial plane and therefore could lead to biased inversion results.

31
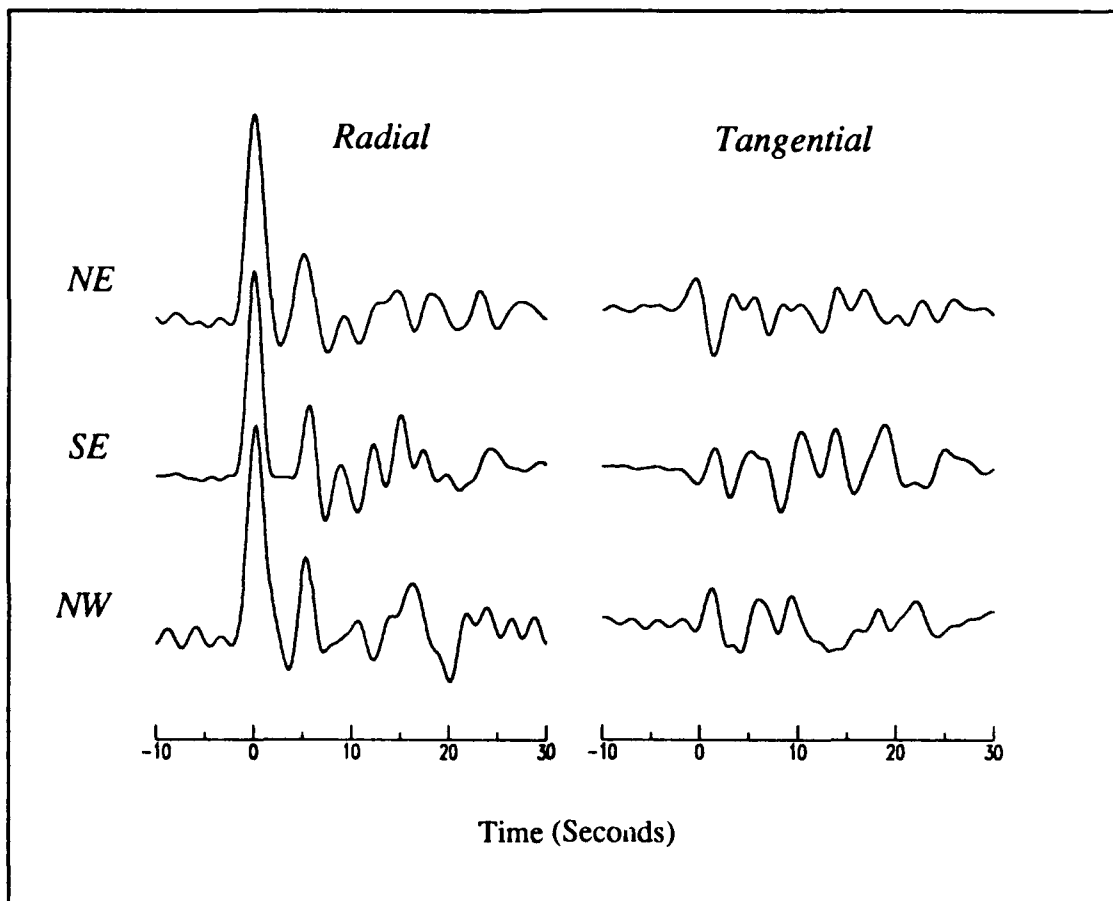
Figure 12. BJI Receiver Functions
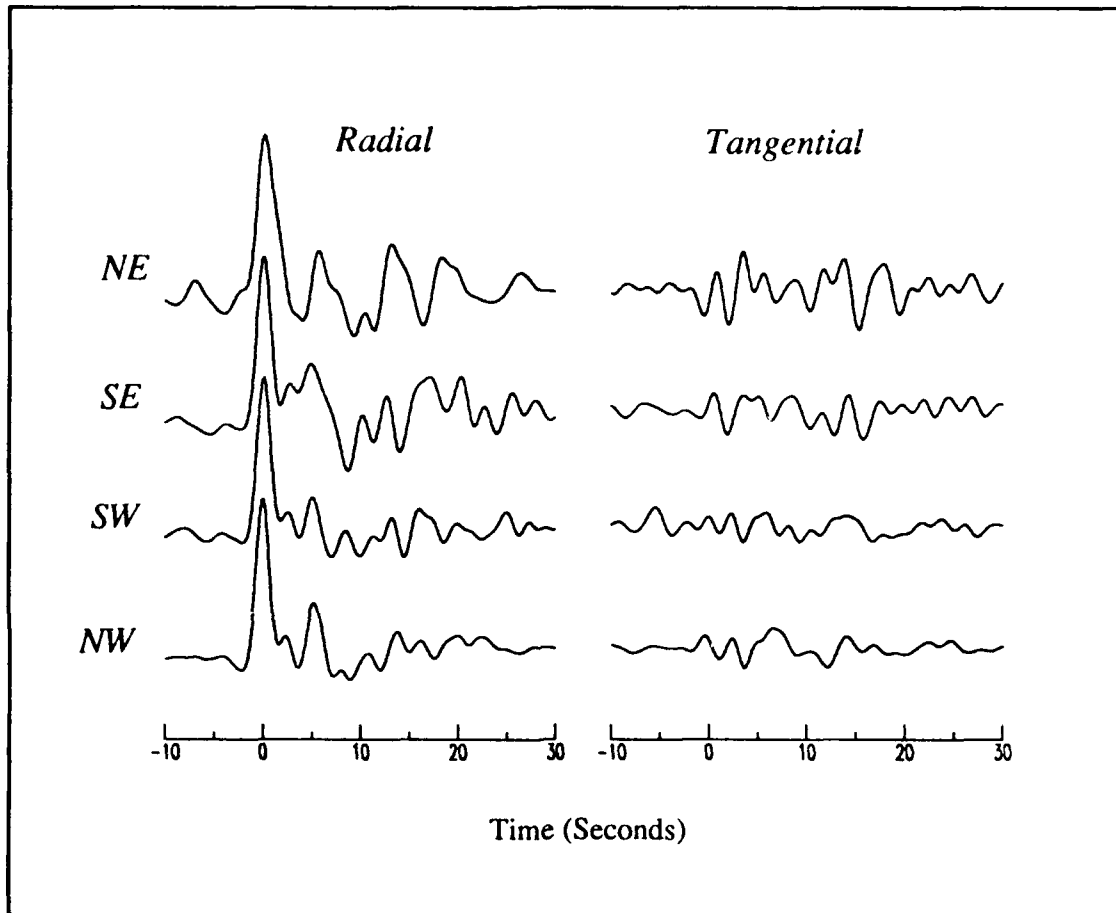
Figure 13. KMI Receiver Functions
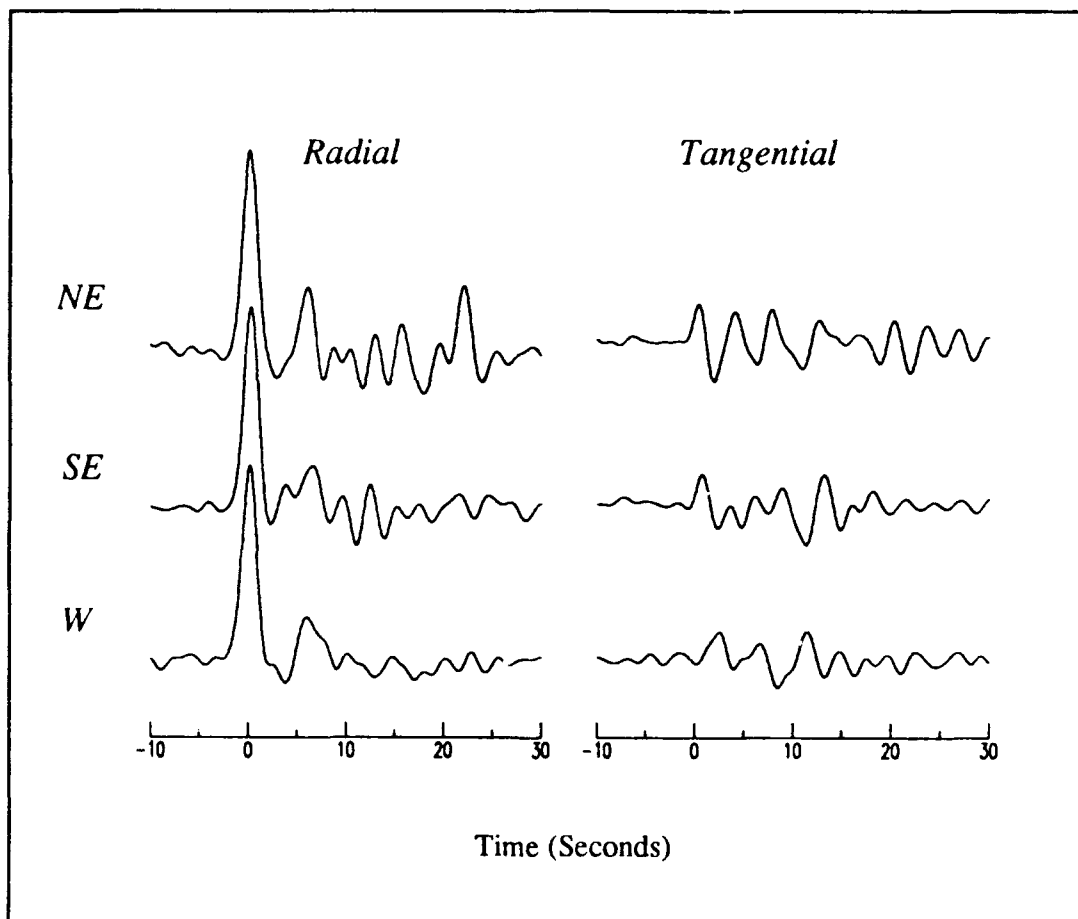
Figure 14. LZH Receiver Functions
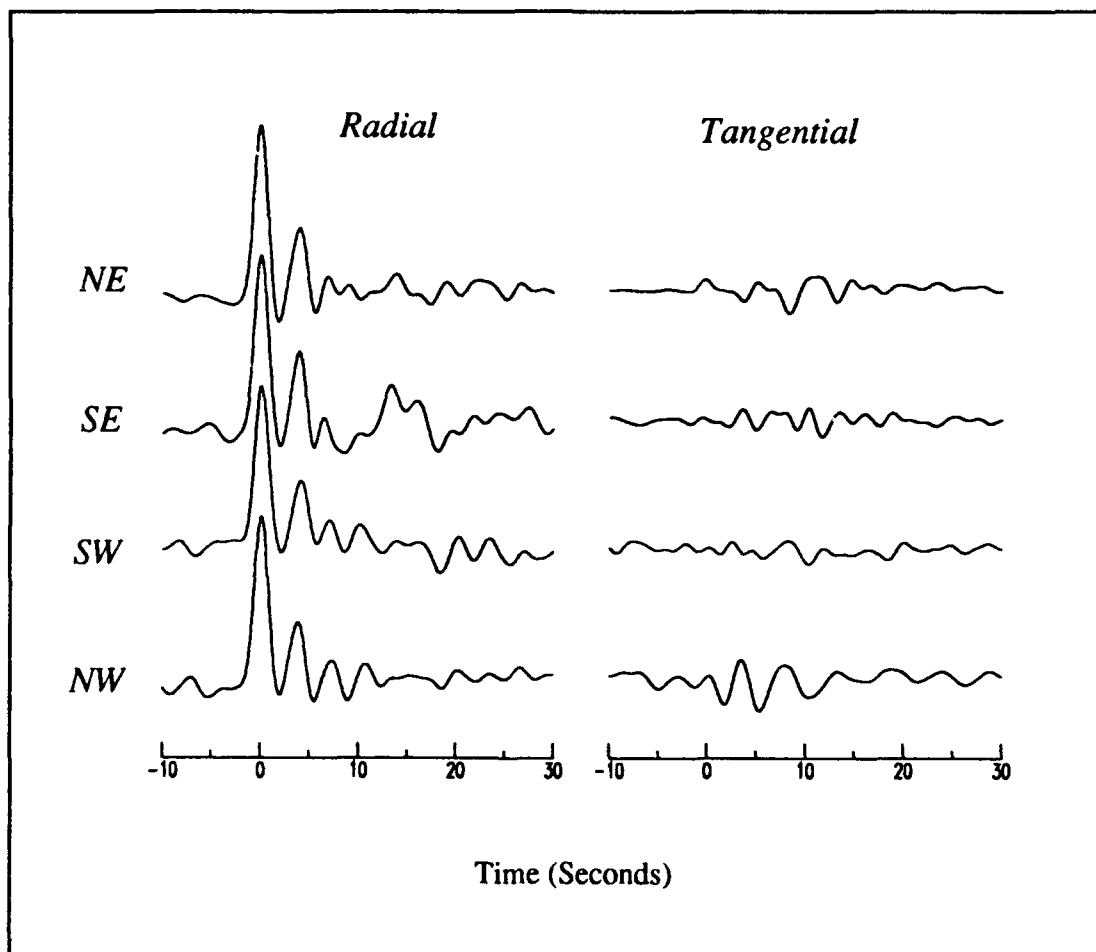
Figure 15

Figure 16. HIA Receiver Functions

HIA-SE Response with increasing epicentral distance

hia55se.rad
hia62se.rad
hia73se.rad
hia55se.tan
hia62se.tan
hia73se.tan

t3−t1=0.18s

hia55se.rad

T1

hia62se.rad

T2

hia73se.rad

T3

Seconds
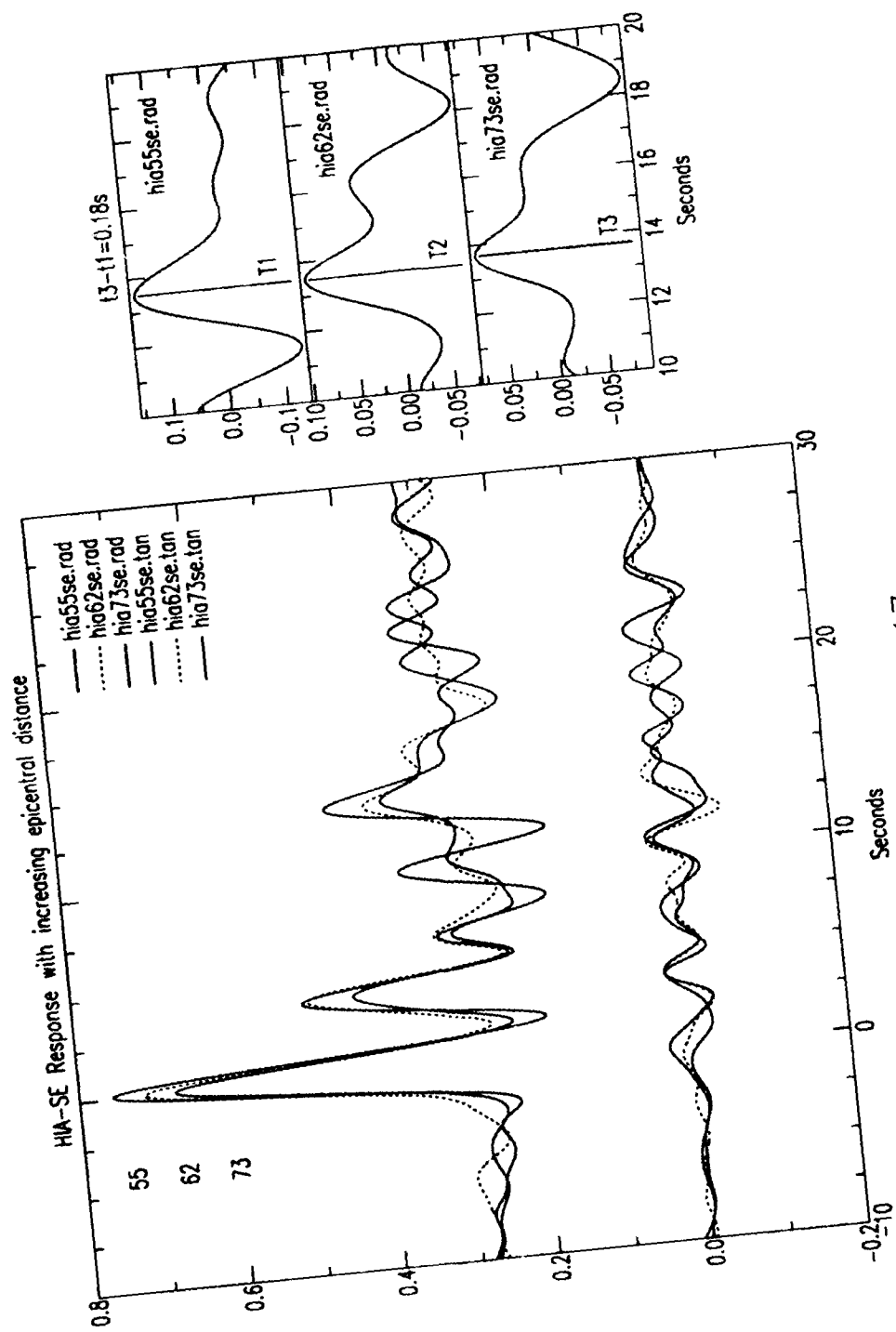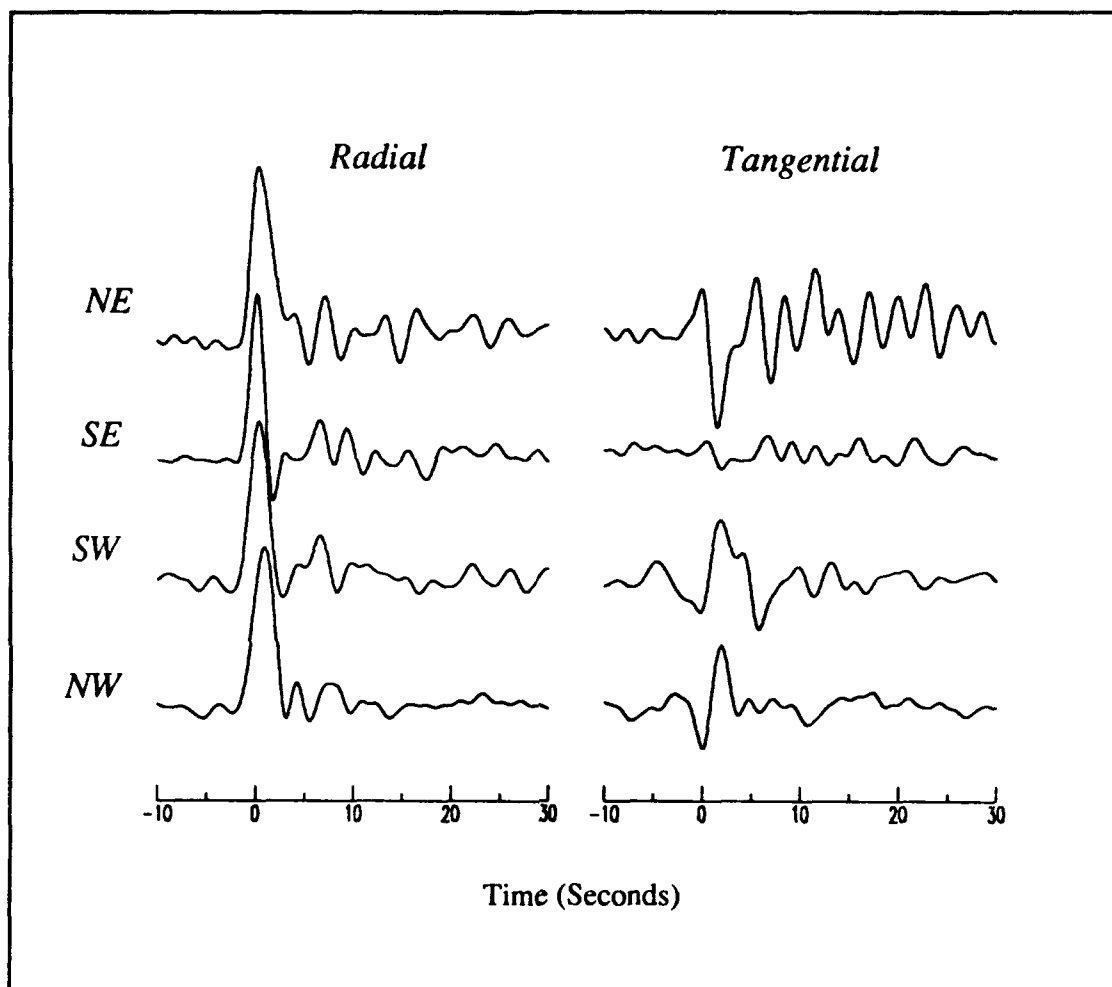
Figure 17

Figure 18. WMQ Receiver Functions
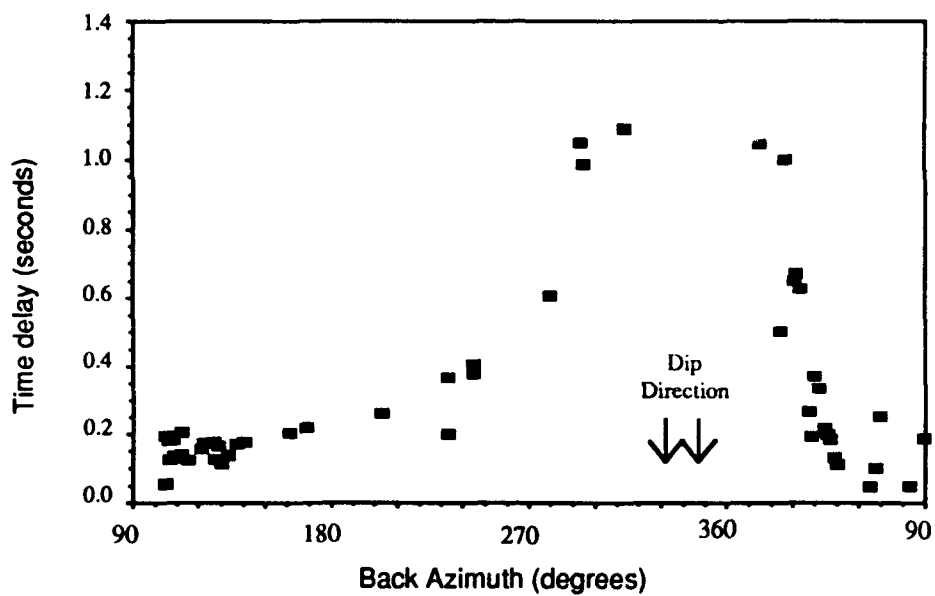
Figure 19a. Shown above are the time lags for all first arrivals on the radial component. A clear time delay as a function of azimuth suggests a dipping structure toward the NW of the station.

WMQ tangential receiver functions
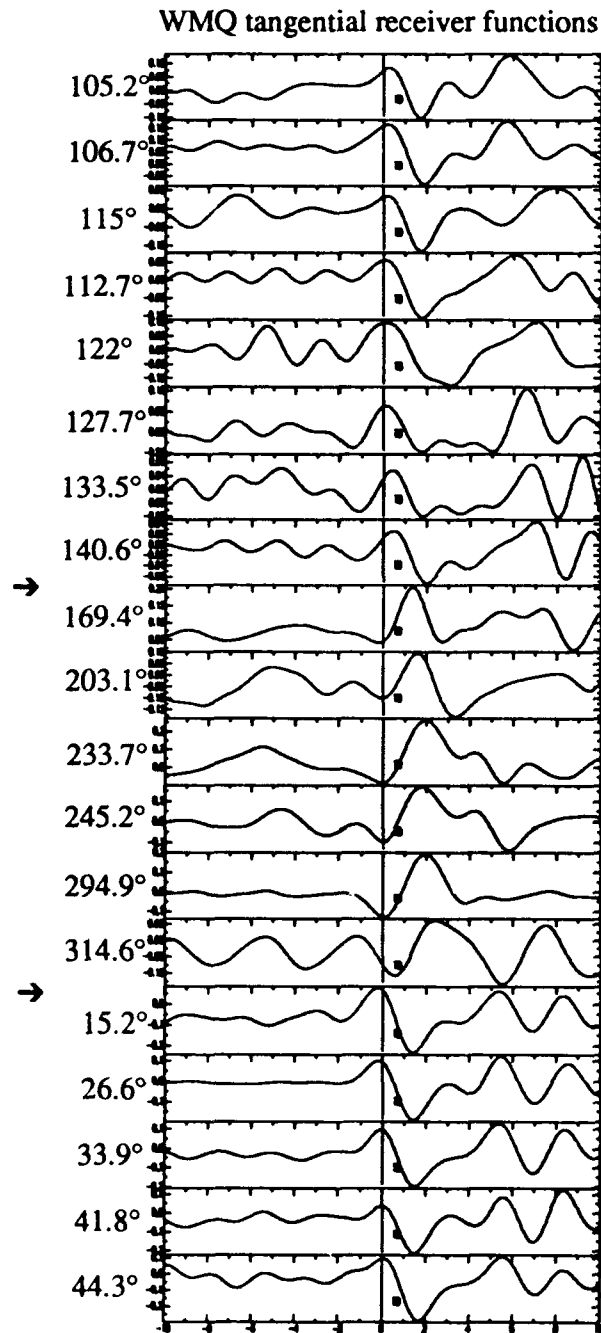
Figure 19b. Distribution of tangential receiver functions by backazimuth at WMQ. Polarity reversal of the first arrival occurs along a line parallel to the dip direction (Langston 1977). Arrows indicate the backazimuthal range where the polarity of the tangential reverses.

6.0 RECEIVER FUNCTION INVERSION

The inversion procedure used in this report and the notation summarized below are consistent with those presented Ammon et al. (1990) who give a rigorous description of the method. We highlight here those points most important for understanding and interpreting our results. The non-linear relationship between the velocity structure and the waveform is approximated by a Taylor series expansion about an initial model, m_0:

$$d_j = F_j[m] \approx F_j[m_0] + (D, \delta m)_j + O\|\delta m^2\| \qquad j = 1, 2, 3, ..N \qquad (7)$$

where d_j represents the observed data, m is the true model, parentheses denote the inner product, and D is a matrix containing the partial derivatives of the waveform with respect to changes in the layer velocities in m_0. The operator F represents the nonlinear relationship between the model and the receiver function, and it includes the calculation of a plane-wave synthetic seismogram and the source equalization procedure described in Section 3.0. Neglecting the higher order terms (7) becomes

$$(D, \delta m)_j \approx F_j[m] - F_j[m_0] \qquad (8)$$

The right hand side of (8) is the waveform residual vector and (8) may be solved for δm using standard least-squares techniques described by Wiggins (1972) and Aki and Richards (1980). Adding (D, m_0) to both sides of (8) enables solution directly for m to produce:

$$(D, m)_j \approx F_j[m] - F_j[m_0] + (D, m_0)_j \qquad (9)$$

Equation (9) is a matrix equation with the only unknown being m. By solving directly for the model m, a smoothness constraint can be applied during the solution of (9). We refer the reader to Ammon et al. (1990) on the topic of applying smoothness constraints to the solution of (9). The matrix D is calculated by employing Randall's (1989) efficient differential seismogram

41

calculation technique. Compressional wave velocities are determined using a constant Poisson's ratio of 0.25 and the layer density is adjusted by using the equation $\rho = 0.32 \ V_p + 0.77$ (Berteussen 1977).

In practice, once an initial model is obtained from previous work and from forward modeling, we run a set of inversions with a range of smoothness values in order to minimize both model roughness and RMS error between the model synthetic and the stacked data. With the pseudo-monte-carlo technique the initial model is randomly perturbed into 24 different starting models by adding a random cubic polynomial function as well as a random component for each layer. The non-uniqueness of the problem is examined by inverting the receiver function beginning with many different starting models (Ammon et al. 1990). The first inversion suite has a random cubic perturbation of 0.5 km/s and the second has inversion suite has a 1.0 km/s perturbation, which allows a larger range of starting models to test the sensitivity of solution models on the initial model. Shown in Figure 20 are the starting models for station BJI. A total of 48 starting models are inverted and all model synthetics that do not fit the most coherent arrivals within the variance of the stacked data are discarded. The range of remaining solution models reflects the non-uniqueness of the particular problem.
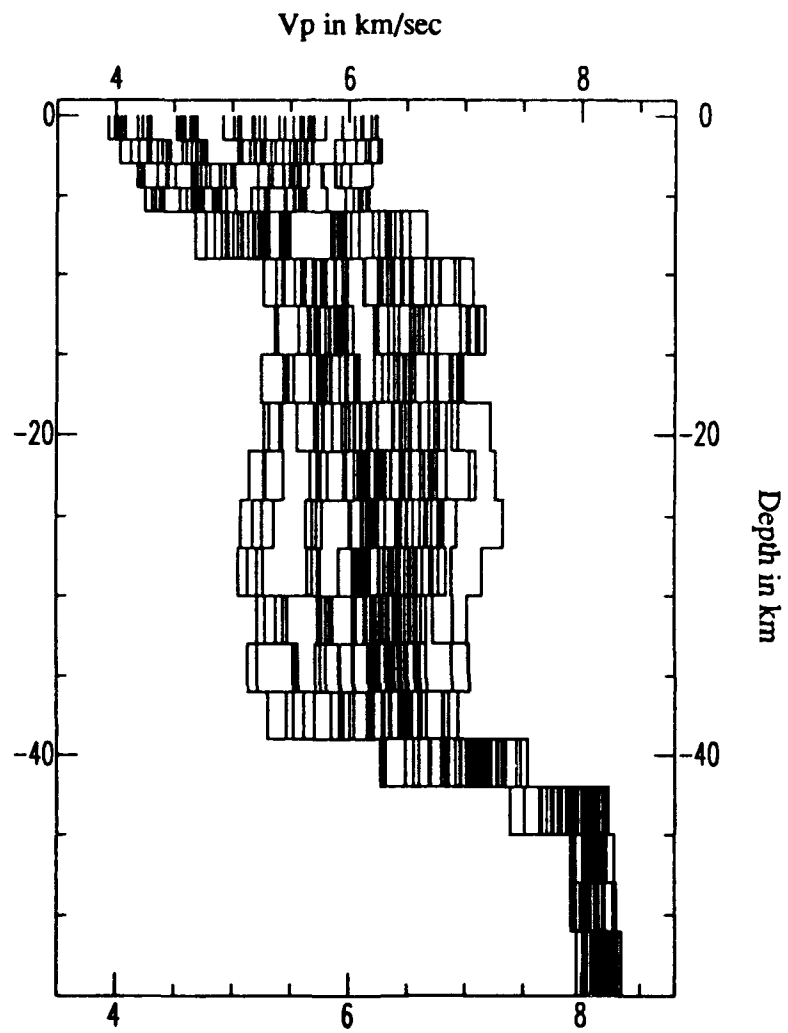
Figure 20. Range of starting models for station BJI.

7.0 PRELIMINARY RESULTS

In this section we present preliminary inversion results for each CDSN station. Our goal here is to determine model estimates of the receiver structure by forcing *only the most prominent phases* in the synthetic receiver functions to be within the ±1 standard deviation bounds obtained from the variance of the stacked data. By relaxing the smoothness constraint as well as shifting the layer thickness and upper mantle velocity we may better fit the smaller amplitude arrivals in the stacked data. However in some cases the lower amplitude arrivals on the radial are close to the energy level present on the tangential. Therefore caution must be used when matching such energy solely with P to S conversions generated within the vertical-radial plane. For those stations where the tangential response is small the initial model solutions should provide a good estimate of the velocity structure beneath the station.

7.1 BJI

Shown in Figure 21 are preliminary model results for station BJI. The starting model was estimated from previous refraction models near the station. In general the crust west of station BJI appears relatively simple in structure. The upper 6 km is characterized by a strong positive gradient. Between 10 to 33 km depth the average crustal P wave velocity is 6 km/s, and a small low velocity zone is present at about 15 km depth. Between 33-39 km depth a strong positive gradient is present, and the top of the upper mantle is at 39 km depth.

7.2 KMI

Shown in Figure 23 are preliminary model estimates for KMI. No models have been selected based on synthetics that fit the data within one standard deviation. The starting model was estimated from previous refraction models near the station. The wide range of crustal velocities suggests significant differences exist between the starting model and the structure necessary to fit the data. Shifting the layer thickness, upper mantle velocity, and decreasing the smoothness constraint may narrow the range. The variability in solution models at KMI is not

surprising given the strong waveform variability of the radial receiver function and the large tangential energy as a function of azimuth.

7.3 LZH

Shown in Figure 24 are preliminary model estimates for LZH. The synthetics are strongly dependent on changes in the near-surface velocity. Model synthetics from a high velocity shallow crust fall on and above the upper resolution bound, while synthetics from lower velocity shallow crustal models fall on and below the lower resolution bound. Shifting layer thickness, upper mantle velocity, and decreasing the smoothness constraint may narrow the range of possible crustal models.

7.4 HIA

Preliminary results for station HIA are shown in Figure 25. The model synthetics provide a reasonably good fit to the data. The starting model was estimated from surface wave estimates near HIA. The upper-crust has a shallow jump in velocity followed by a negative gradient to ~7.5 km depth. The mid-crust has a relatively constant velocity of ~6.0 km/sec to a depth of 28 km, and overlies a transitional crust-mantle boundary between 30-37 km depth. The top of the upper mantle is at 37-38 km depth.

7.5 WMQ

Shown in Figure 26 are preliminary results at station WMQ for data arriving in the up-dip direction. The upper crust shows a strong positive gradient to about 6-8 km depth, which is necessary to fit the large time lag measured for this azimuth. The absence of a prominent converted phases results in a smoothly varying velocity structure with increasing depth.
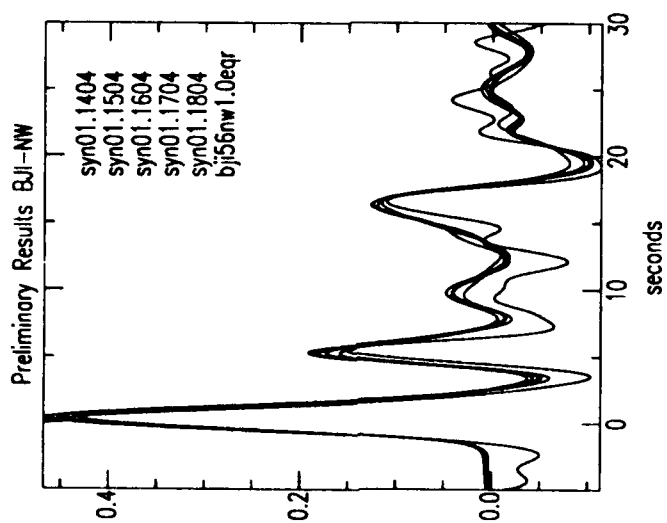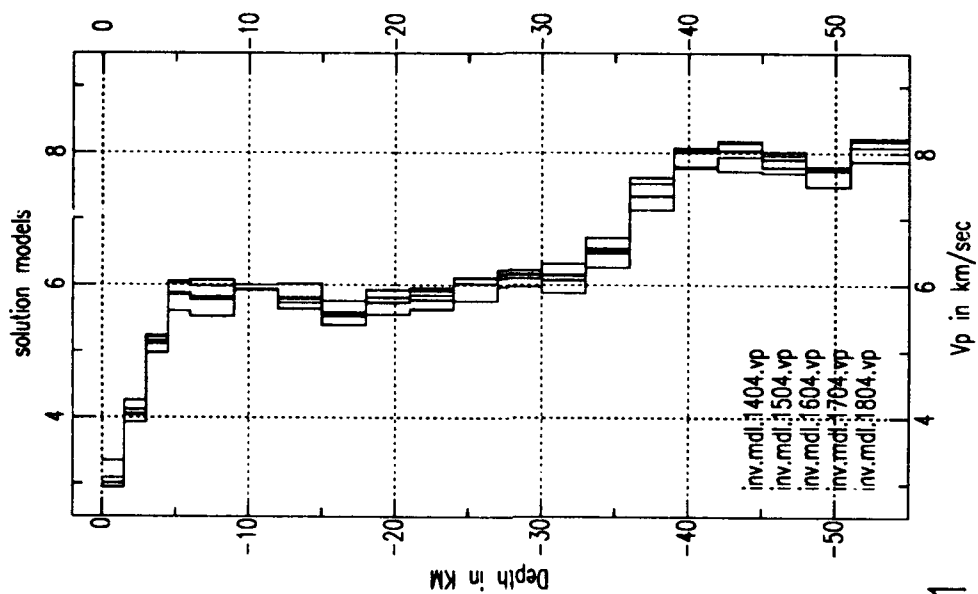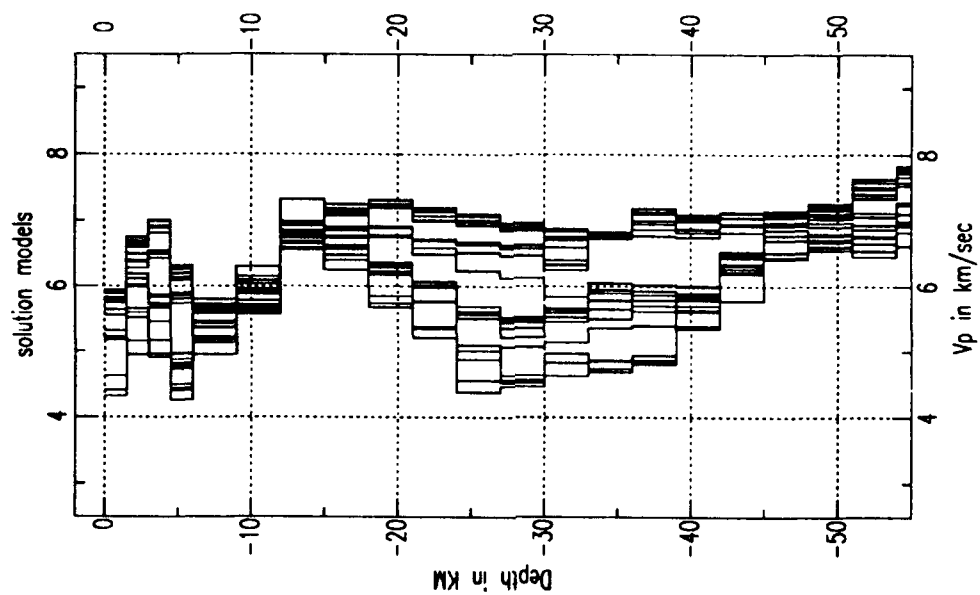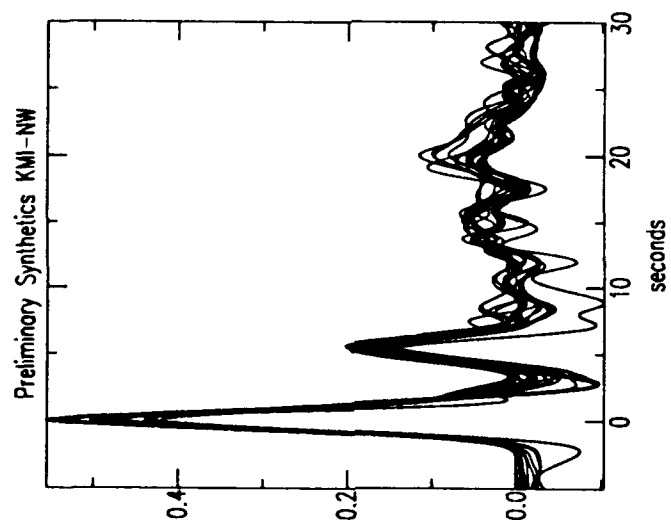
Figure 21

solution models

Depth in KM

Vp in km/sec

Preliminary Synthetics KMI-NW

seconds

Figure 22

47
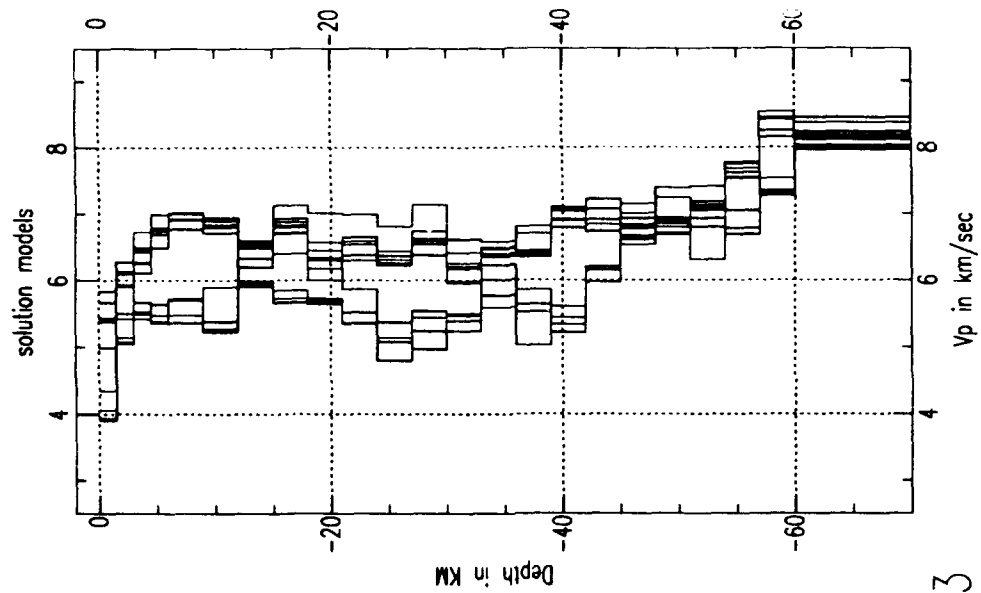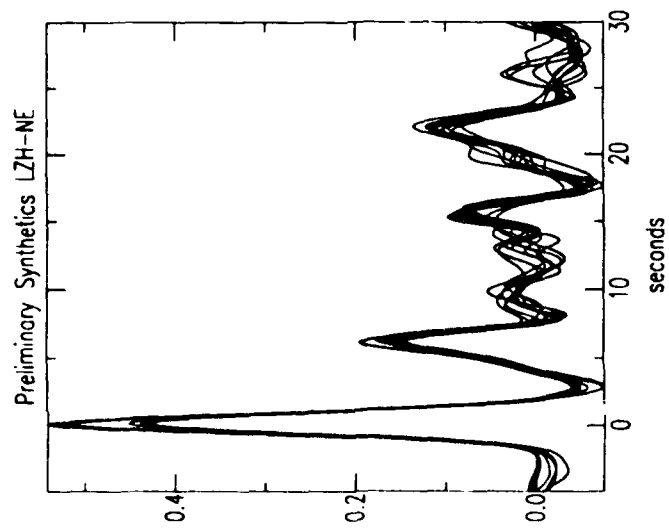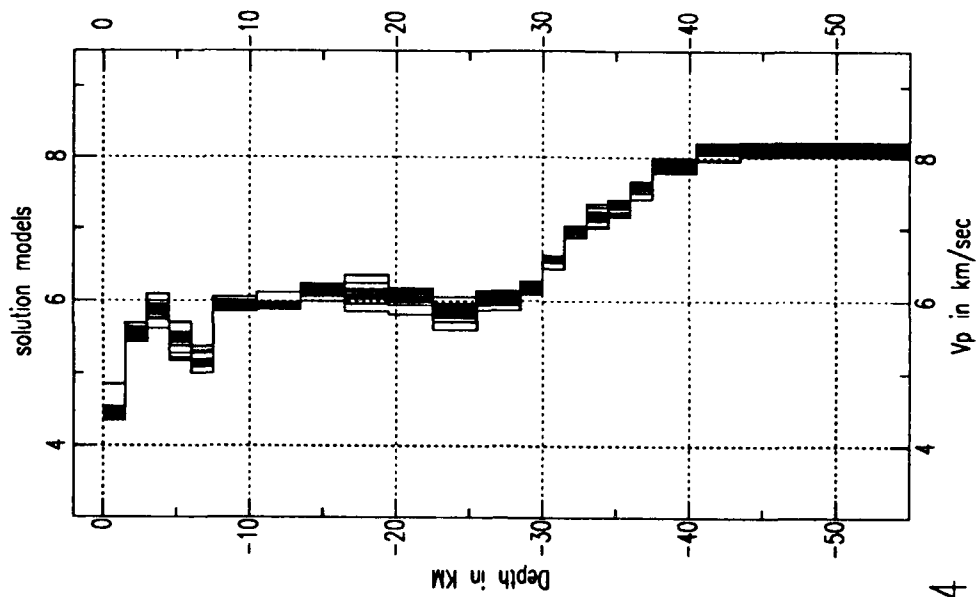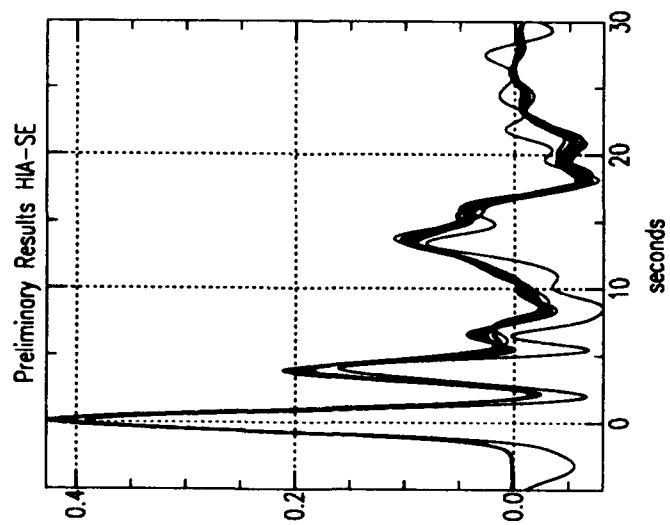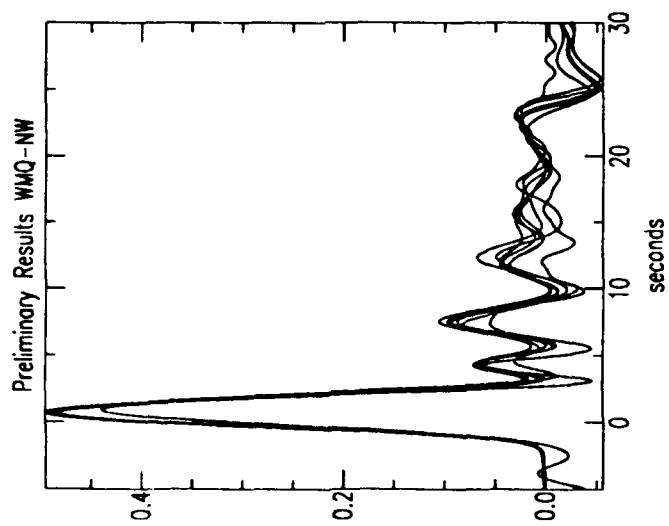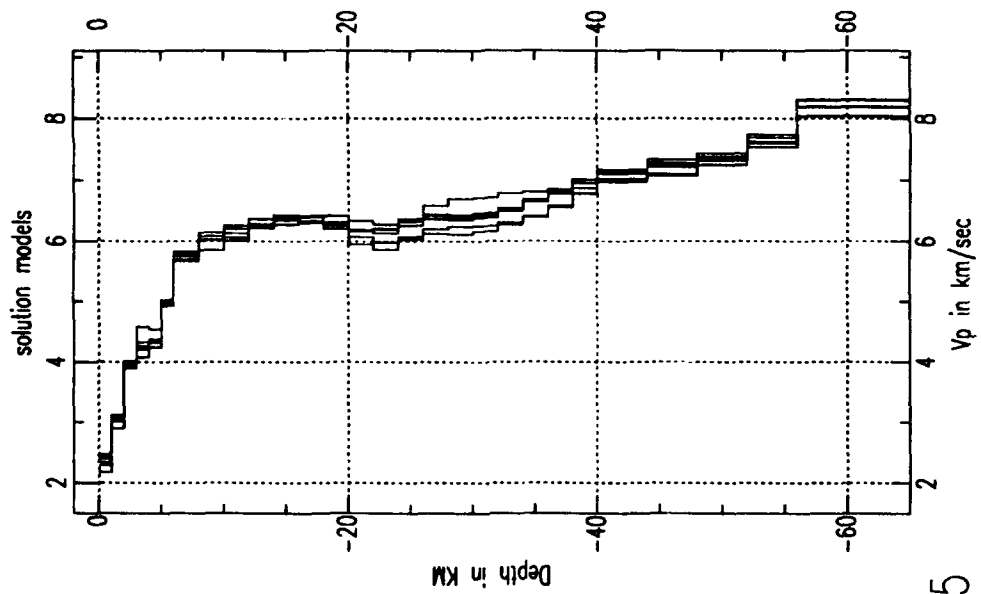
Figure 23

Figure 24

Figure 25

8.0 DISCUSSION

The main advantage of the receiver function technique is that it can be used to obtain estimates of the velocity structure beneath a seismic station without resorting to specialized field studies around the station. Furthermore, the method is able to resolve the velocity structure of the crust and upper mantle within only a few tens of kilometers beneath a seismic station as compared to seismic refraction techniques which typically estimate the crust and upper mantle structure averaged over 50-100 km. However, a tradeoff between receiver function and refraction methods arises because refraction experiments can record waveforms with frequencies up to 25-30 Hz while this receiver function study examines frequencies up to about 0.4 Hz. Thus, while low-pass receiver functions tend to smooth over the fine details of the crustal structure, they are able to constrain depth-to-interface and velocity values for the major velocity layers beneath a station.

8.1 IMPLICATIONS FOR THE MONITORING OF NUCLEAR TEST BAN TREATIES

Determination of the velocity structure beneath remote seismic stations has important applications for the monitoring of existing nuclear test ban treaties and clandestine testing. Accurate event locations require a detailed knowledge of the seismic velocity structure of the earth (Blandford, 1982), something which is not well known in potential areas where clandestine testing could take place. Also, accurate knowledge of Earth structure beneath the recording station can be an important factor in refining yield estimates of nuclear explosions (Bache, 1982, Hansen et al., 1990). Some of the variability in amplitude and waveshape measurements of the body waves (typically the P waves) from underground nuclear explosions is due to scattering and body-wave conversions beneath the receiving stations (e.g., Bannister, 1990). The receiver function technique is useful in addressing the effect of this particular problem at a given seismic station.

Shown in Figure 26 are great circle paths from the September 14, 1988 JVE2 nuclear explosion at the Soviet test site in Semipalatinsk (SEM) to the five CDSN stations that recorded

51

this event. The source-receiver distances are: WMQ - 950 km; LZH - 2530 km; HIA - 2926 km; BJI - 3106 km; and KMI - 3432 km. The effects of the velocity structure beneath these CDSN stations on the waveforms from this event are explored in Figures 27a,b. Figure 27a shows filtered observations (vertical and radial) for the P wave and some of the P coda. Synthetic waveforms for these stations are shown in Figure 27b. The synthetics were computed by taking the Mueller-Murphy source pulse shape for an 118 kt explosion in granite and convolving it with the appropriate instrument response and the vertical and radial responses computed from one of the models determined in this study for each station. The synthetics are quite simple. They do not include important upper mantle triplications which must be present in most of the seismograms, nor do they include free surface reflections (pP), spall, source structure or tectonic release. The purpose of the synthetics is to document how much variability in the P waveforms can be expected due to the differences in the receiver structures found beneath the CDSN stations. Figure 27b shows the same major effects documented by Bannister et al. (1990) in the P waves from NORESS. Motions on the radial component are much more affected by the estimated receiver structures than the vertical component. However, even for the vertical component, the width of the second peak for the P wave (the so-called "c" peak) varies from station to station. Furthermore, the relative amplitude of the "c" peak to the first (or "a") peak differs somewhat among the stations for the vertical P component. The radial ground motions show variations among the width of the "c" peaks as well as in the waveforms about 5 seconds after the P-wave. The latter, hints of which may be observed in the data, reflect differences in the crustal structure from station to station. Thus, as concluded by Bannister et al. (1990) P-to-S scattering does have a significant effect upon the P coda whereas P-to-P scattering does not.
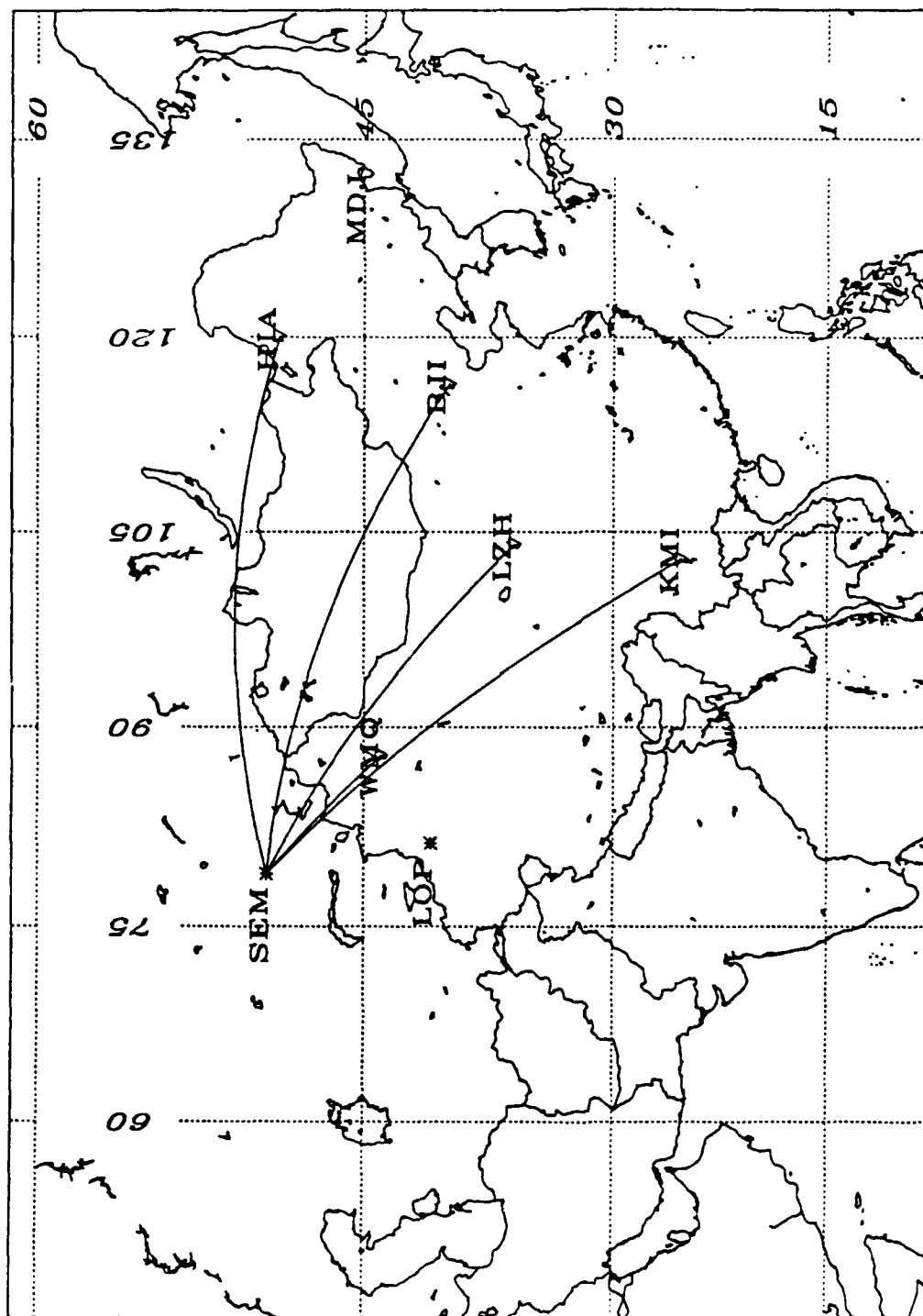
Figure 26. Mercator projection of great circle paths between Semipalatinsk and CDSN stations (HIA) Hailar, (BJI) Beijng, (KMI) Kunming, (LZH) Lanzhou, and (WMQ) Urumqi.
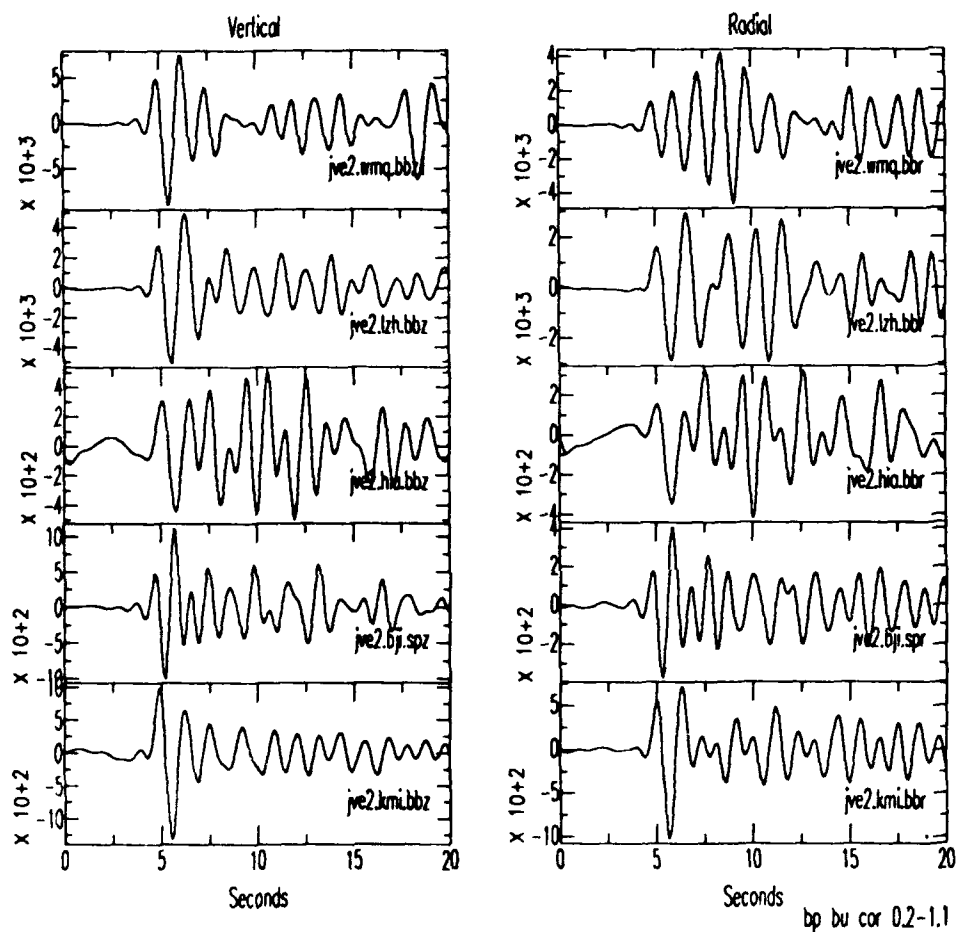
Figure 27a.   JVE2 vertical (left) and radial (data) as recorded at
all CDSN stations bandpass filtered between 0.2—1.1 Hz.
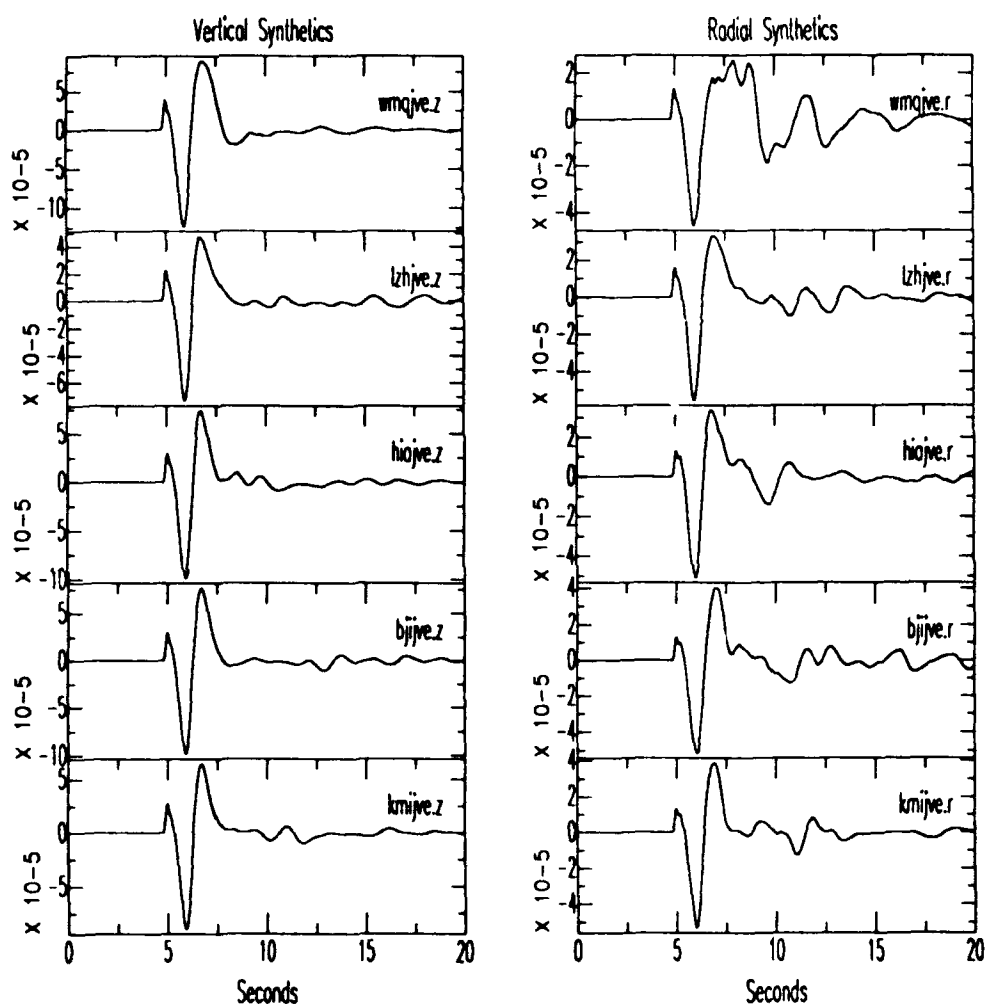
Figure 27b. Synthetic vertical and radial seismograms obtained from a characteristic preliminary model from each station, convolved with a JVE2 source time function and STS-1 instrument response.

9.0 REFERENCES

Aki, K., and P.G. Richards, Quantative Seismology: Theory and Methods, Vol 2, 932 pp, W.H. Freeman, New York 1980.

Ammon, C.J., The isolation of receiver effects from teleseismic P waveforms, Bull. Seismol. Soc. Am, 81, 2504-2510, 1991.

Ammon, C.J., G.E. Randall, and G. Zandt, On the resolution and non-uniqueness of receiver function inversions, J Geophys. Res. v 95, 15303-15318, 1990.

Archambeau, C.B., E.A. Flinn, and D.G. Lambert, Detection, Analysis and Interpretation of Teleseismic Signals, J. Geophys. Res. v 71, 3483-3501, 1966.

Baiji, L., and Li Ning, Residuals of Teleseismic P-wave travel times and lateral heterogeneity of the crust and upper mantle structure in Yunnan Region, Journal of Seismological Research, Vol 10. No. 1, 103-117, 1987.

Bakun, W.H., Crustal model parameters from P-wave spectra, Bull. Seismol. Soc. Am, 61, 913-935, 1971.

Bannister, S.C., E.S. Husebye, and B.O. Ruud, Teleseismic P coda analyzed by three-component and array techniques: deterministic location of topographic P-to-Rg scattering near the NORESS array, Bull. Seism. Soc. Am., 80, 1969-1986, 1990.

Basham, P.W., and R. M. Ellis, The composition of P codas using magnetic tape seismograms, Bull. Seismol. Soc. Am, 59, 473-486, 1969.

Bath, M. and R. Steffanson, S-P conversions from the base of the crust, Ann. Geophys., v 19, 119-130, 1966.

Bache, T.C., Estimating the yield of underground nuclear explosions, Bull. Seism. Soc. Am., 72, S131-S168, 1982.

Berteussen, K.A., Moho depth determinations based on spectral ratio analysis of NORSAR long-period P waves, Phys. Earth Planet Int., 1 v 15, 13-27, 1977.

Blandford, R.R., Seismic event discrimination, Bull. Seism. Soc. Am., 72, S69-S87, 1982.

Burchfiel, B.C., P. Zhang, W. Yipeng, Z., Weiqi, S. Fangmin, D. Qidong, P. Molnar, and L. Royden, Geology of the Haiyuan Fault zone, Ningxia-Hui autonomous region, China, and its relation to the evolution of the northeastern margin of the Tibetan Plateau, Tectonics, vol. 10, NO. 6, pp 1091-1110, 1991.

Burdick, L.J., and C.A. Langston, Modeling crustal structure through the use of converted phases in teleseismic body-wave forms, Bull. Seismol. Soc. Am, 67, 677-691, 1977.

Changquan, L., and J. Shixu, Structural property of the crust and upper mantle in the Tangshan Earthquake region, ACTA Seismological Sinica, Vol 8, No 4, 1-22, 1986.

Fang, W., R. Van der Voo, R., and Liang, Q., Devonian Paleomagnetism of Yunnan Province across the Shan Thai South China Suture, Tectonics, Vol 8, NO. 5, pp 939-952, 1989.

Fu, Zhengxiang, Spatial variations in seismicity of the eastern Chinese mainland, Tectonophysics, 193, p 291-298, 1991.

Gilder, S.A., G.R. Keller, M. Luo and P.C. Goodell, Timing and spatial distribution of rifting in China, Tectonophysics, 197, p 225-243, 1991.

Hansen, R.A., F. Ringdal and P.G. Richards, The stability of RMS Lg measurements and their potential for accurate estimation of the yields of Soviet underground nuclear explosions, Bull. Seism. Soc. Am., 80, 2106-2126, 1990.

Hellinger, S. K. Shedlock, J. Sclater, and H. Ye, The Cenozoic evolution of the North China Basin, Tectonics, Vol. 4, NO. 4. pp 343-358, 1985.

Huang, K. and N. D. Opdyke, Paleomagnetism of Jurassic rocks from the southwestern Sichuan and the timing of the closure of the Qinling Suture, Tectonophysics, 200, 299-316, 1991.

Hsu, K.J., L. Jiliang, C. Haihong, W. Qingchen, S. Shu, and A.M.C. Sengor, Tectonics of South China: Key to understanding West Pacific geology, Tectonophysics, 183, p 9-39, 1990.

Kennet, B.L.N. Seismic wave propagation in stratified media, Cambridge University Press, Cambridge, England, (1983).

Kurita, T., Crustal and upper mantle structure in Japan from amplitude and phase spectra of long-period P waves. Part 1, Central mountain area, J. Phys. Earth. 17, p 13-41, 1969.

Liang, G., and Weijuan, L., The characteristics of deep structure of the north segment of the North-South Seismic Belt, Acta Seismologica Sinca, Vol 4. No. 2, 259-273, 1991.

Langston, C.A., The effect of planer dipping structure on source and receiver responses for constant ray parameter, Bull. Seismol. Soc. Am., V. 67, 713-724, 1977a.

Langston, C.A., Corvallis , Oregon, crustal and upper mantle receiver structure from teleseismic P and S waves, Bull. Seismol. Soc. Am, 67, 1029-1050, 1977b.

Langston, C.A., Structure under Mount Rainier, Washington, inferred from teleseismic body waves, J. Geophys. Res. 84, 4749-4762, 1979.

Langston, C.A., Evidence for the subducting lithosphere under southern Vancouver Island and western Oregon from teleseismic P wave conversions, J. Geophys. Res., 86, 3857-3866, 1981.

Mangino, S.G., The receiver structure beneath the Chinese Digital Seismic Network Stations, International union of geodesy and geophysics, IASPEI-S2, p. 35, Vienna, Austria (1991).

Mangino, S.G., G. Zandt, and C.J. Ammon, The crustal structure beneath the Walker Belt, western Nevada, submitted to Bull. Seismol. Soc. Am., 1992.

Owens, T.J., G. Zandt, and S.R. Taylor, Seismic evidence for an ancient crustal rift beneath the Cumberland Plateau, Tennessee: A detailed analysis of broadband teleseismic P-waveforms, J. Geophys. Res., 89, 7783-7795, 1984.

Owens, T.J., G. Zandt, and S.R. Taylor, Crustal structure at regional seismic test network stations determined from inversion of broadband teleseismic P waveforms, Bull. Seismol. Soc. Am, 77, 631-662, 1987.

Owens, T.J., R. S. Crosson, and M. A. Hendrickson, Constraints on the subduction geometry beneath western Washington from broadband teleseismic waveform modeling, Bull. Seismol. Soc. Am., 78, 1319-1334, 1988a.

Owens, T.J., and R. S. Crosson, Shallow Structure effects on Broadband Teleseismic P Waveforms, Bull. Seismol. Soc. Am., 78, 96-108, 1988b.

Peterson, J. and E.E. Tilgner, Description and preliminary testing of the CDSN seismic sensor systems, U.S. Geological Survey Open File Report 83-288, 37 pp, 1985.

Peterson J., *and others*—Kexin, Q., *and others*, The China Digital Seismograph Network, A joint report by the Institute of Geophysics, State Seismological Bureau and the Albuquerque Seismological Laboratory, U.S. Geological Survey; 91 pp, 1987.

Qizhong, Y., Z. Guoquing, K. Rongju, and H. Hongxiang, The crust structure of Simao to Malong Profile, Yunnan Province, China, Journal of Seismological Research, Vol 8. No 2, 249-273, 1985.

Randall, G.E., Efficient calculation of differential seismograms for lithosphere receiver functions, Geophys. J. Int., 99, 469-481, 1989.

Rui, F., Z. Jieshou, D. Yunyu, C. Guoying, H. Zhenqin, Y. Shubin, Z. Hainan, and S. Kezhong, Crustal Structure in China From Surface Waves, (in Chinese) ACTA Seismologica Sinica, Vol 3 No 4 p 335-350, 1981.

Shangyou, N., Paleoclimate and paleomagnetic constraints on the Paleozoic reconstructions of south China, North China and Tarim, Tectonophysics, 196, 279-308, 1991.

Shedlock, K.M., and S.W. Roecker, Elastic wave velocity structure of the crust and upper mantle beneath the North China basin, J. Geophys. Res., 92, 9327-9350, 1987.

Tapley, W.C., and Tull J.E., SAC-Seismic Analysis Code, Users Manual, Lawrence Livermore National Laboratory, Mail Stop L-205, Livermore, CA 94550, 1991.

Wiggins, R., The general linear inverse problem: implications of surface waves and free oscillations for earth structure, Reviews of Geophys. and Space Phys.,10, 251-285, 1972.

Wu, F. T., Studies of Regional Phases and Discriminates in Asia, GL-TR-90-0017, 1990, ADA222184.

Xingxin, D., Electrical conductivity anomaly in the Lanzhou-Xi'An-Zhengzhou Zone, ACTA Seismologica Sinica, Vol 1 No 3 p 60 -68, 1988.

Yong, C., K. Tsoi, C. Feibi, G. Zhenhuan, Z. Qijia, and C. Zhangli, The Great Tangshan Earthquake of 1976, An Anatomy of Disaster, edited by: State Seismological Bureau, PRC, ISBN 0-08-034875-0, 149 pp, 1988.

Yuan, X., S. Wang, L.Li, and J. Zhu, A geophysical investigation of the deep structure in china, in Reflection Seismology, A Global Perspective, Geodynamic Series Volume 13, American Geophysical Union, Publication 0112, p.151-160, 1986.

Zandt, G., and T.J. Owens, Comparison of velocity profiles determined by seismic refraction and teleseismic methods, Tectonophysics 128, p. 155-161, 1986.

Zhao, X., R.S. Coe, Y. Zhou, H. Wu, and J. Wang, New paleomagnetic results from northern China: collision and suturing with Siberia and Kazakhstan, Tectonophysics, 181, p 43-81, 1990.

Zhao, L, Helmberger, D.V., and Harkrider, D.G., Shear Velocity Structure of the Crust and Upper Mantle Beneath Tibetan Plateau and Southeastern China, PL-TR-91-2062, 1991, ADA238933.

Zhao, Z.Y., and B.F.Windley, Cenozoic tectonic extension and inversion of the Jizhong Basin, Hebi, northern China, Tectonophysics, 185, p 83-89, 1990.

Table 1 Station BJI

		Event	Latitude°	Longitude°	Mb	BAZ°	Delta°	Location
NE	1	0121	58.840 N	156.858 W	6.1	39	55	Alaska **
	2	1052	58.419 N	175.445 W	6.3	42	46	Bering Sea
	3	7005	52.448 N	169.381 W	6.1	49	50	Fox Island *
	4	7049	51.298 N	179.279 W	6.2	53	45	Andreanof Islands *
	5	7321	58.586 N	143.270 W	6.6	35	61	Gulf of Alaska **
	6	8038	50.785 N	173.465 E	6.2	55	40	Aleutian Islands *
	7	8066	56.953 N	143.032 W	6.8	37	62	Gulf of Alaska **
	8	8085	62.154 N	124.182 W	6.1	26	67	Canada
	9	9247	55.543 N	156.835 W	6.5	42	56	Alaska **
	10	9280	51.314 N	179.028 W	6.1	53	45	Aleutian Islands *
SE	11	0177	22.015 S	179.473 W	6.0	123	86	Fiji *
	12	0222	19.085 S	177.385 W	6.0	120	85	Fiji *
	13	1008	18.016 S	173.660 W	6.1	116	87	Tonga
	14	6303	21.702 S	176.616 W	6.4	120	87	Fiji *
	15	7041	19.489 S	177.456 W	6.2	119	85	Fiji *
	16	7078	20.397 S	176.134 W	5.9	119	87	Fiji *
	17	7119	19.013 S	177.736 W	5.9	119	85	Fiji *
	18	9070	17.766 S	174.761 W	6.4	119	85	Tonga *
	19	0208	15.355 S	167.464 E	6.4	128	72	Vanuatu **
	20	0224	19.435 S	169.132 E	6.3	129	77	Vanuatu **
	21	0271	13.559 S	167.079 E	6.0	127	71	Vanuatu **
	22	7042	15.834 S	167.355 E	5.9	128	73	Vanuatu
	23	8157	15.397 S	167.578 E	6.0	127	72	Vanuatu **
	24	9096	19.306 S	169.002 E	6.1	129	76	Vanuatu
	25	9268	20.355 S	169.277 E	6.1	129	77	Vanuatu **
NW	26	0151	45.811 N	26.769 E	6.1	307	62	Romania *
	27	0310	28.251 N	55.462 E	6.2	276	50	Iran *
	28	1119	42.489 N	43/647 E	6.2	297	53	Western Caucasus
	29	7125	36.480 N	70.673 E	5.8	279	35	Hindu Kush Region
	30	7352	28.191 N	56.677 E	5.8	275	49	Iran
	31	8342	40.987 N	44.485 E	6.2	296	53	Turkey-USSR border

Event location modifications correspond to the following azimuthal bins: *BJI-45-NE,
**BJI-58-NE; *BJI-86-SE, **BJI-74-SE. See Appendix 1 for individual events.

Table 2 Station KMI

		Event	Latitude°	Longitude°	Mb	BAZ°	Delta°	Location
NE	1	7049	51.298 N	179.279 W	6.2	43	63	Andreanof Isl.
	2	7058	53.470 N	167.291 W	6.2	39	70	Fox Island **
	3	7080	52.056 N	177.547 W	6.0	42	64	Andreanof Isl. *
	4	7081	51.594 N	173.574 W	5.9	42	66	Andreanof Isl. *
	5	7172	54.211 N	162.601 W	6.2	37	72	Alaska Peninsula **
	6	8038	50.785 N	173.465 E	6.2	44	58	Aleutian Islands *
	7	8320	52.109 N	171.103 W	5.9	41	68	Fox Island
	8	8066	56.953 N	143.032 W	6.8	30	81	Gulf of Alaska
	9	8085	62.154 N	124.182 W	6.1	20	85	Canada
	10	9139	54.305 N	165.574 W	6.1	38	70	Aleutian Islands
	11	9167	31.807 N	137.982 E	5.9	32	75	Honshu
	12	9247	55.543 N	156.835 W	6.5	35	75	Alaska **
	13	9280	51.314 N	179.028 W	6.1	43	63	Aleutian Isl. *
	14	0121	58.840 N	156.858 W	6.1	32	74	Alaska **
SE	15	7041	19.489 S	177.456 W	6.2	111	89	Fiji ^
	16	7042	15.834 S	167.355 E	5.9	115	74	Vanuatu **
	17	7285	7.288 S	154.371 E	6.3	115	59	Solomon Isl.
	18	7338	5.777 S	154.555 E	5.9	114	58	Solomon Isl. *
	19	8022	19.847 S	133.803 E	6.2	143	53	Northern Australia *
	20	8070	20.917 S	178.645 W	6.1	113	89	Fiji
	21	8137	13.941 S	166.335 E	6.0	114	73	Vanuatu
	22	8157	15.397 S	167.578 E	6.0	115	74	Vanuatu **
	23	8184	14.278 S	167.180 E	5.9	114	73	Vanuatu **
	24	8209	13.112 S	167.051 E	5.9	113	73	Vanuatu **
	25	8205	6.526 S	152.779 E	6.7	116	57	New Britain Region
	26	8205a	22.127 S	174.900 E	5.9	117	84	Loyalty Isl ^
	27	8219	7.136 S	151.057 E	5.9	117	56	New Britain Region
	28	9035	4.625 S	153.066 E	6.1	113	57	New Ireland Region *
	29	9070	17.766 S	174.761 W	6.4	113	89	Tonga ^
	30	9268	6.526 S	152.779 E	6.7	118	78	Vanuatu **
	31	0177	22.015 S	179.473 W	6.0	114	88	Fiji ^
	32	0208	22.015 S	179.473 W	6.0	115	74	Vanuatu **
	33	0224	19.435 S	169.132 E	6.3	117	78	Vanuatu **
	34	0271	13.559 S	167.097 E	6.0	113	73	Vanuatu **
	35	0364	5.097 S	150.967 E	6.6	115	55	New Britain Region *
SW	36	9069	13.702 S	34.420 E	6.2	248	76	Malawi *
	37	9232	11.766 N	41.942 E	5.8	268	58	Ethiopia *
	38	9233	11.874 N	41.870 E	6.3	268	58	Ethiopia *
	39	0362	14.875 S	66.777 E	6.0	225	53	Mid-Indian Rise
NW	40	8342	40.987 N	44.485 E	6.2	303	50	Turkey-USSR border *
	41	8219	36.461 N	71.043 E	6.1	300	29	Afghn.-USSR border
	42	9259	40.337 N	51.534 E	6.4	302	45	Caspian Sea *
	43	9260	42.489 N	43.647 E	6.2	302	44	Caspian Sea *
	44	0150	45.841 N	26.688 E	6.7	310	62	Romania
	45	0310	28.251 N	55.462 E	6.2	285	42	Iran *
	46	1119	42.489 N	43/647 E	6.2	305	51	Western Caucasus *

Event location modifications correspond to the following azimuthal bins: *KMI-63-NE,
**KMI-73-NE; *KMI-56-SE, **KMI-75-SE, ^KMI-88-SE. See Appendix 1 for
individual events.

Table 3 Station LZH

		Event	Latitude°	Longitude°	Mb	BAZ°	Delta°	Location
NE	1	7049	51.298 N	179.279 W	6.2	48	55	Andreanof Isl.*
	2	7080	52.056 N	177.547 W	6.0	46	55	Andreanof Isl.*
	3	7081	51.594 N	173.574 W	5.9	46	58	Andreanof Isl.
	4	7172	54.211 N	162.601 W	6.2	40	63	Alaska Peninsula
	5	7279	52.956 N	159.972 E	6.1	48	42	Kamchatka
	6	7321	58.586 N	143.270 W	6.6	30	70	Gulf of Alaska **
	7	8038	50.785 N	173.465 E	6.2	50	50	Aleutian Islands
	8	8047	51.564 N	175.041 E	5.9	46	57	Rat Isl. *
	9	8066	56.953 N	143.032 W	6.8	32	71	Gulf of Alaska **
	10	8067	41.669 N	152.222 E	5.9	66	37	Northern Pacific
	11	8085	62.154 N	124.182 W	6.1	21	74	Canada
	12	8320	52.109 N	171.103 W	5.9	45	59	Fox Island
	13	9022	41.806 N	144.282 E	6.0	61	31	Hokkaido
	14	9065	35.545 N	140.444 E	5.9	80	29	Honshu
	15	9101	49.488 N	159.185 E	6.3	53	41	Kuril Islands
	16	9139	54.305 N	165.574 W	6.1	41	61	Aleutian Islands
	17	9144	56.177 N	164.264 E	5.9	43	44	Komandorsky Islands
	18	9167	31.807 N	137.982 E	5.9	34	66	Honsu
	19	9247	55.543 N	156.835 W	6.5	37	65	Alaska **
	20	9280	51.314 N	179.028 W	6.1	48	55	Aleutians *
	21	9282	51.780 N	171.869 E	6.0	49	49	Aleutians
	22	9355	45.364 N	150.108 E	5.9	60	35	Kuril Isl
	23	0121	58.840 N	156.858 W	6.1	34	64	Alaska **
SE	24	6303	21.702 S	176.616 W	6.4	113	94	Fiji ^
	25	7003	14.998 S	167.929 E	6.0	92	60	Vanuatu
	26	7041	19.489 S	177.456 W	6.2	112	92	Fiji ^
	27	7078	20.397 S	176.134 W	5.9	112	94	Fiji ^
	28	7168	5.577 S	130.791 E	6.6	143	48	Banda Sea *
	29	8022	19.847 S	133.803 E	6.2	147	62	Northern Australia **
	30	8116	7.791 S	158.255 E	6.1	119	67	Solomon Islands **
	31	8124	22.744 S	170.278 E	5.9	121	85	Loyalty Isl. Region
	32	8137	13.941 S	166.335 E	6.0	117	77	Vanuatu
	33	8151	7.501 S	128.325 E	6.5	147	49	Banda Sea *
	34	8157	15.397 S	167.578 E	6.0	118	78	Vanuatu ~
	35	8184	14.278 S	167.180 E	5.9	117	77	Vanuatu ~
	36	8205	6.526 S	152.779 E	6.7	122	62	New Britain Region
	37	8209	13.112 S	167.051 E	5.9	116	77	Vanuatu ~
	38	9010	3.162 S	130.556 E	5.9	141	46	Ceram *
	40	9067	1.031 N	126.189 E	5.9	146	41	Molucca Passage
	41	9195	8.081 S	125.129 E	6.4	151	48	Timor *
	42	9257	1.644 N	127.322 E	6.0	142	40	Halmahera *
	43	9268	6.526 S	152.779 E	6.7	120	83	Vanuatu ~
	44	9291	10.155 S	161.065 E	6.1	118	70	Solomon Islands
	45	9300	11.022 S	162.350 E	6.1	118	72	Solomon Islands ~
	46	0177	22.015 S	179.473 W	6.0	115	92	Fiji ^
	47	0208	22.015 S	179.473 W	6.0	118	78	Vanuatu ~
	48	0271	13.559 S	167.097 E	6.0	117	72	Vanuatu ~
	49	0364	5.097 S	150.967 E	6.0	122	60	New Britain Region **
	50	1003	7.148 S	148.490 E	6.0	126	60	East Papua New Guinea **

Table 3 Station LZH (continued)

	Event		Latitude°	Longitude°	Mb	BAZ°	Delta°	Location
W	51	7352	28.191 N	56.677 E	5.8	272	40	Iran
	52	8094	4.687 N	94.419 E	5.9	197	32	Northern Summatera
	53	8342	40.987 N	44.485 E	6.2	295	46	Turkey-USSR border *
	54	9259	40.337 N	51.534 E	6.4	292	40	Caspian Sea *
	55	9260	42.489 N	43/647 E	6.2	292	40	Caspian Sea
	56	0310	28.251 N	55.462 E	6.2	273	41	Iran*
	57	0362	14.875 S	66.777 E	6.0	221	61	Mid Indian Rise
	58	0150	45.841 N	26.688 E	6.7	305	56	Romania
	59	0151	45.811 N	26.769 E	6.1	305	56	Romaina
	60	0310	28.251 N	55.462 E	6.2	273	41	Iran ′
	61	1119	42.489 N	43/647 E	6.2	297	46	Western Caucasus *

Event location modifications correspond to the following azimuthal bins: *LZH-57-NE, **LZH-68-NE; *LZH-46-SE, **LZH-62-SE, ~LZH-77-SE, ^LZH-93-SE. See Appendix 1 for individual events.

Table 4 Station HIA

		Event	Latitude°	Longitude°	Mb	BAZ°	Delta°	Location
NE	1	8066	56.953 N	143.032 W	6.8	42	54	Gulf of Alaska *
	2	8085	62.154 N	124.182 W	6.1	29	57	Canada *
	3	9280	51.314 N	179.028 W	6.1	62	38	Aleutian Islands *
	4	8320	52.109 N	171.103 W	5.9	58	42	Fox Island
SE	5	9195	8.018 S	125.129 E	6.4	173	57	Timor *
	6	9212	8.048 S	121.384 E	6.3	178	57	Flores Isl Region *
	7	8151	7.501 S	128.325 E	6.5	169	57	Banda Sea *
	8	9010	3.162 S	130.556 E	5.9	166	53	Ceram *
	9	7168	5.577 S	130.791 E	6.6	166	55	Banda Sea *
	10	7178	2.164 S	138.170 E	5.7	156	53	West Irian *
	11	9213	4.511 S	139.022 E	6.0	156	56	West Irian
	12	0208	15.355 S	167.464 E	6.4	132	76	Vanuatu **
	13	0271	13.559 S	167.079 E	6.0	132	75	Vanuatu **
	14	8137	13.941 S	166.335 E	6.0	133	75	Vanuatu **
	15	8157	15.397 S	167.578 E	6.0	132	77	Vanuatu **
	16	8184	14.278 S	167.180 E	5.9	132	75	Vanuatu **
	17	9035	10.447 S	161.372 E	6.0	135	69	Solomon Isl.
	18	9291	10.155 S	161.063 E	6.1	136	69	Solomon Isl.
	19	8116	7.791 S	158.255 E	6.1	137	66	Solomon Isl. ** ^
	20	0364	5.097 S	150.967 E	6.6	143	60	New Britain Region ^
	21	1003	7.148 S	148.490 E	6.0	147	61	East Papua, New Guinea
	22	7285	7.288 S	154.371 E	6.3	141	63	Solomon Isl. ^
	23	8190	6.290 S	154.667 E	5.8	140	63	Solomon Isl.
	24	8205	6.526 S	152.779 E	6.7	142	62	New Britain Region ^
	25	8219	7.136 S	151.057 E	5.9	144	62	New Britain Region ^
	26	1008	18.016 S	173.660 W	6.1	119	89	Tonga
	27	9096	19.306 S	169.002 E	6.1	133	81	Vanuatu
SW	28	0310	28.251 N	55.462 E	6.2	271	52	Iran
	29	1005	23.478 N	95.983 E	6.3	224	32	Burma*
	30	7125	36.480 N	70.673 E	5.8	268	37	Hindu Kush Region *
	31	7352	28.191 N	56.677 E	5.8	270	52	Iran
	32	8233	26.755 N	86.616 E	6.4	240	34	Nepal-India *
	33	9232	11.766 N	41.942 E	5.8	268	73	Ethiopia
	34	0362	14.875 S	66.777 E	6.0	231	79	Mid-Indian Rise
NW	35	1119	42.489 N	43/647 E	6.2	293	51	Western Caucasus *
	36	8342	40.987 N	44.485 E	6.2	291	51	Turkey-USSR border *
	37	9260	40.203 N	51.749 E	6.1	286	47	Caspian Sea *
	38	0150	45.841 N	26.688 E	6.7	305	58	Romania
	39	0151	45.811 N	26.769 E	6.1	305	58	Romania

Event location modifications correspond to the following azimuthal bins: *HIA-55-SE,
^HIA-62-SE, **HIA-73-SE. See Appendix 1 for individual events.

Table 5 Station MDJ

		Event	Latitude°	Longitude°	Mb	BAZ°	Delta°	Location
NE	1	9139	54.305 N	165.574 W	6.1	52	42	Fox Islands
	2	9247	55.543 N	156.835 W	6.5	48	46	Alaska
SE	3	9134	30.523 S	178.414 W	5.9	137	88	Kermadec
	4	9135	9.803 S	159.531 E	5.9	145	61	Solomon Isl
	5	9140	30.508 S	178.270 W	5.7	137	88	Kermadec
	6	9213	4.511 S	139.022 E	6.0	167	50	West Irian
	7	9268	20.355 S	169.277 E	6.1	141	74	Vanuatu
	8	9291	10.155 S	161.063 E	6.1	144	62	Solomon Isl
	9	8022	19.847 S	133.803 E	6.2	175	64	Northern Australia
SW	10	9163	21.861 N	89.763 E	6.1	248	40	Bangladesh
	11	9212	8.048 S	121.348 E	6.3	191	53	Flores Isl. Region
	12	9257	1.644 N	127.322 E	6.0	183	43	Halmahara
NW	13	9233	11.874 N	41.870 E	6.3	276	80	Ethiopia
	14	9259	40.337 N	51.543 E	6.4	295	55	Caspian Sea
	15	9260	40.203 N	51.749 E	6.1	294	55	Caspian Sea

See Appendix 1 for individual receiver functions.

Table 6 Station WMQ

		Event	Latitude°	Longitude°	Mb	BAZ°	Delta°	Location
NE	1	7005	52.448 N	169.381 W	6.1	41	63	Fox Island *
	2	7058	53.470 N	167.291 W	6.2	40	63	Fox Island *
	3	7080	52.056 N	177.547 W	5.9	45	59	Andreanof Isl.
	4	7081	51.594 N	173.574 W	5.9	44	61	Andreanof Isl. *
	5	7172	54.211 N	162.601 W	6.2	37	65	Alaska Peninsula *
	6	8038	50.785 N	173.465 E	6.2	50	55	Aleutian Islands
	7	8066	56.953 N	143.032 W	6.8	26	70	Gulf of Alaska
	8	8085	62.154 N	124.182 W	6.1	15	71	Canada
	9	9065	35.545 N	140.444 E	5.9	83	40	Honshu
	10	9082	33.788 N	141.395 E	5.6	84	42	Honshu
	11	9167	31.807 N	137.982 E	5.9	30	66	Honshu
	12	9280	51.314 N	179.028 W	6.1	46	59	Aleutian Isl *
	13	0121	58.840 N	156.858 W	6.1	31	64	Alaska*
	14	9247	55.543 N	156.835 W	6.6	33	66	Alaska*
SE	15	7168	5.577 S	130.791 E	6.6	130	63	Banda Sea *
	16	7178	2.164 S	138.170 E	5.7	121	64	West Irian *
	17	7338	5.777 S	154.555 E	5.9	110	77	Solomon Islands **
	18	8094	4.687 N	94.419 E	5.9	169	39	Northern Sumatera
	19	8116	7.791 S	158.255 E	6.1	109	81	Solomon Islands
	20	8151	7.501 S	128.325 E	6.5	133	63	Banda Sea *
	21	8157	15.397 S	167.578 E	6.0	107	93	Vanuatu
	22	8184	14.278 S	167.108 E	5.9	107	92	Vanuatu
	23	8205	6.526 S	152.779 E	6.7	112	76	New Britain Region **
	24	8207	6.081 S	133.667 E	6.5	127	65	Aroe Isl *
	25	8209	13.112 S	167.051 E	5.9	106	91	Vanuatu
	26	9010	3.162 S	130.556 E	5.9	128	61	Ceram *
	27	9059	2.288 N	129.916 E	5.7	127	54	Molucca Passage
	28	9067	1.031 N	126.189 E	5.9	132	54	Molucca Passage
	29	9067a	1.031 N	126.189 E	5.9	130	55	Molucca Passage
	30	9121	4.200 S	101.366 E	5.5	161	49	Southern Sumatera
	31	9135	9.803 S	159.531 E	5.9	110	84	Solomon Islands
	32	9144	3.748 S	159.564 E	5.6	105	79	Sulawesi
	33	9165	12.875 N	143.351 E	5.5	105	56	South of Mariana Isl
	34	9195	8.081 S	125.129 E	6.4	136	62	Timor *
	35	9212	8.048 S	121.384 E	6.3	140	60	Flores Isl Region *
	36	9213	4.511 S	139.022 E	6.0	122	67	West Irian*
	37	9291	10.155 S	161.063 E	6.1	108	85	Solomon Isl.
	38	9300	11.022 S	162.305 E	6.1	108	86	Solomon Isl.
	39	0364	5.097 S	150.967 E	6.6	112	74	New Britain Region **
	40	1003	7.148 S	148.490 E	6.0	116	74	East Papua New Guinea **
SW	41	9068	13.710 S	34.381 E	5.8	234	75	Malawi
	42	9069	13.702 S	34.420 E	6.2	234	75	Malawi
	43	9232	11.766 N	41.942 E	5.8	245	50	Ethiopia *
	44	9233	11.874 N	41.870 E	6.3	245	50	Ethiopia *
	45	0063	28.925 S	66.331 E	6.8	199	75	Pakistan
	46	0362	14.875 S	66.777 E	6.0	203	61	Mid Indian Rise

Table 6 Station WMQ (continued)

		Event	Latitude°	Longitude°	Mb	BAZ°	Delta°	Location
NW	47	8342	40.987 N	44.185 E	6.2	280	32	Turkey-USSR border *
	48	9160	71.432 N	4.371 W	5.6	335	49	Jan Mayen Isl.
	49	9177	39.112 N	28.242 W	5.7	314	79	Azores
	50	9359	60.008 N	73.445 W	6.2	350	75	Northern Quebec
	51	0150	45.841 N	26.769 E	6.7	294	42	Romania *
	52	0151	45.811 N	26.769 E	6.1	294	42	Romania *

Event location modifications correspond to azimuthal bins: *WMQ-63-SE, **WMQ-75-SE. See Appendix 1 for individual events.

TABLE 7 CDSN STATION LOCATIONS

BJI	Lat: 40.040277° N Lon: 116.175000° E Elev: +43.0 meters Baijatuan, Beijing
HIA	Lat: 49.266666° N Lon: 119.7416666° E Elev: +610.0 meters Hailar, Neimenggu Province
KMI	Lat: 25.148055° N Lon: 102.747222° E Elev: +1952.0 meters Kunming, Yunnan Province
LZH	Lat: 36.086666° N Lon: 103.84444° E Elev: +1560.0 meters Lanzhou, Gansu Province
MDJ	Lat: 44.616388° N Lon: 129.591944° E Elev: +250.0 meters Mudanjiang, Heilongjiang Province
WMQ	Lat: 43.821111° N Lon: 87.695° E Elev: +970.0 meters Urumqi, Xinjiang Province
QIZ	Lat: 19.029444° N Lon: 109.843333° E Elev: +230 meters Qiongzhong, Hainan Island
SSE	Lat: 31.095555° N Lon: 121.186666° E Elev: +10 meters Sheshan
ENH	Lat: 46.266666° N Lon: 109.497500° E Elev: +487 meters Enshi, Hubie Province

Table 8. Sensitivity of each CDSN BB Channel

BJI.BBZ	7.200E+09
BJI.BBN	6.890E+09
BJI.BBE	6.910E+09
HIA.BBZ	7.120E+09
HIA.BBN	7.020E+09
HIA.BBN	7.020E+09
KMI.BBZ	6.810E+09
KMI.BBN	6.960E+09
KMI.BBE	7.020E+09
LZH.BBZ	7.470E+09
LZH.BBN	6.830E+09
LZH.BBE	6.900E+09
MDJ.BBZ	7.340E+09
MDJ.BBN	7.020E+09
MDJ.BBE	7.020E+09
WMQ.BBZ	7.160E+09
WMQ.BBN	6.870E+09
WMQ.BBE	6.850E+09

(counts/meter/second)

CDSN Instrument Response, all signal bands.

Period in Seconds
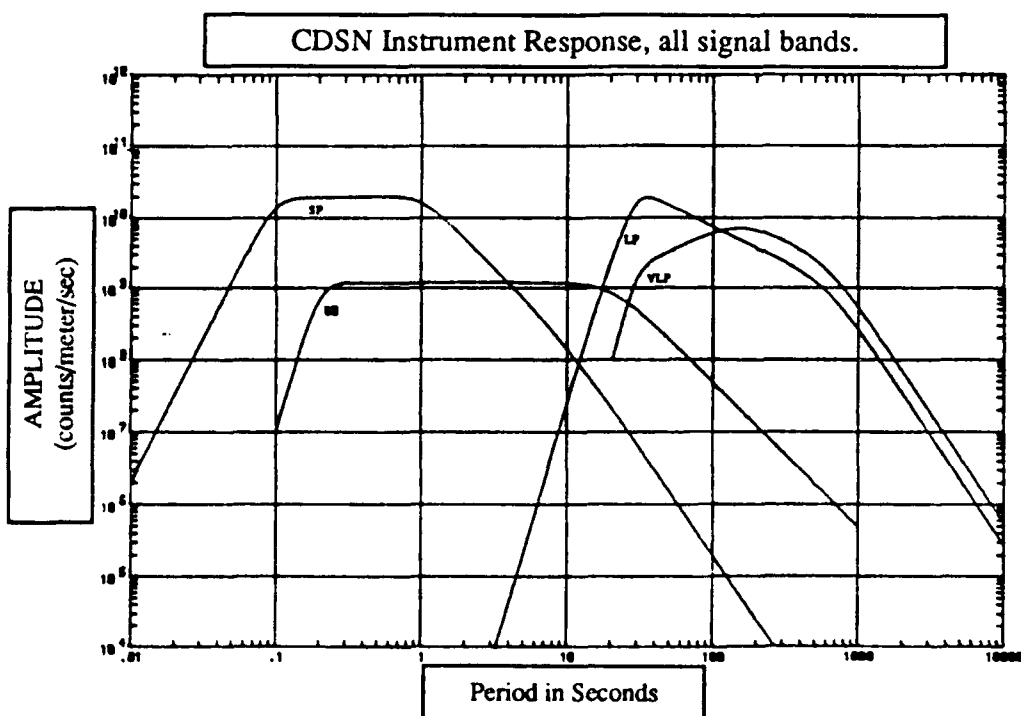
APPENDIX

In the following style of file identification each radial receiver function corresponds to each single or double asterisk, hat, or tilde appended to a given event in Tables 1-5. Event indexes are defined by calender year and Julian day. For example *0241.bji.eqr* corresponds to 1990-Julian day 241-station BJI-radial receiver function. Shown below each bin is the stack and the bin filename includes the average epicentral distance.

BJI Event Distribution


Figure A-1. Shaded ellipses correspond to azimuthal bins shown for each quadrant.
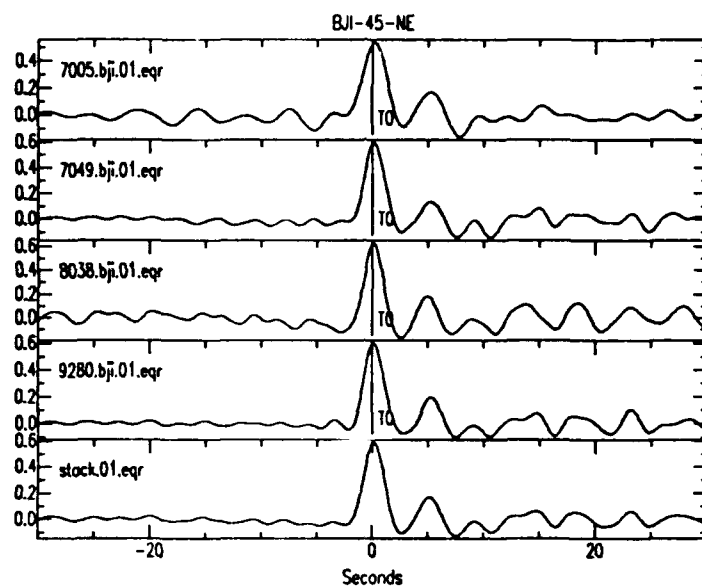
Figure A-2
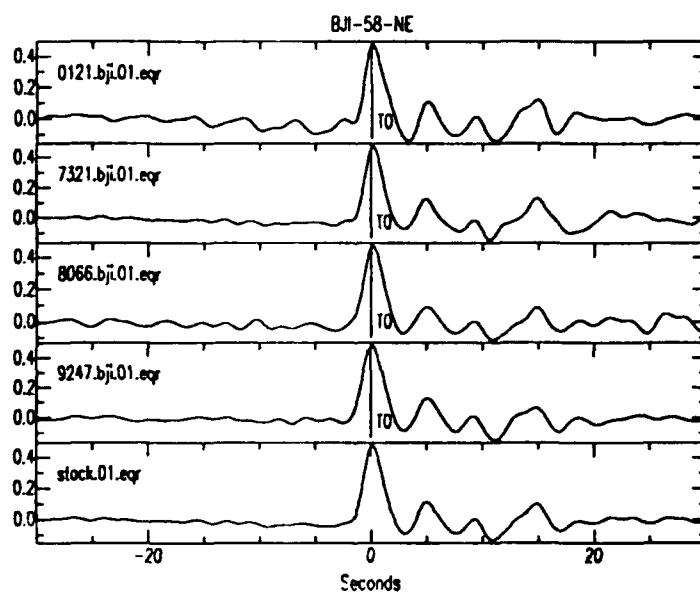
Figure A-3
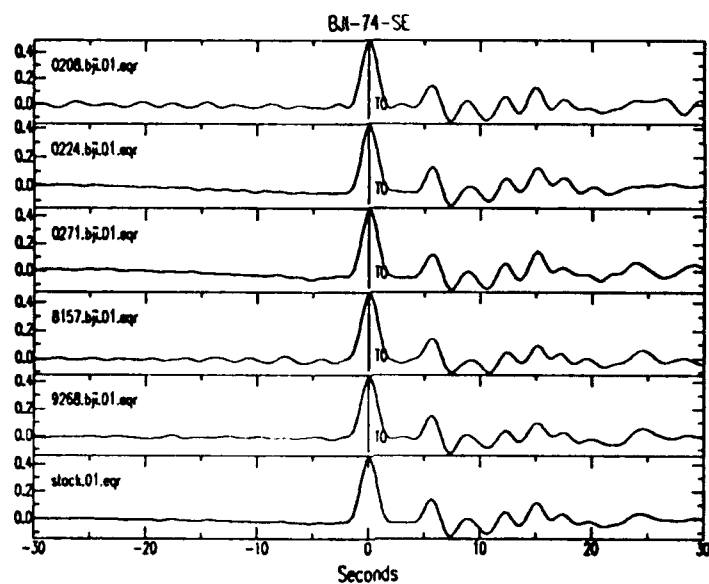
Figure A-4

Figure A-5

72

Figure A-6

73
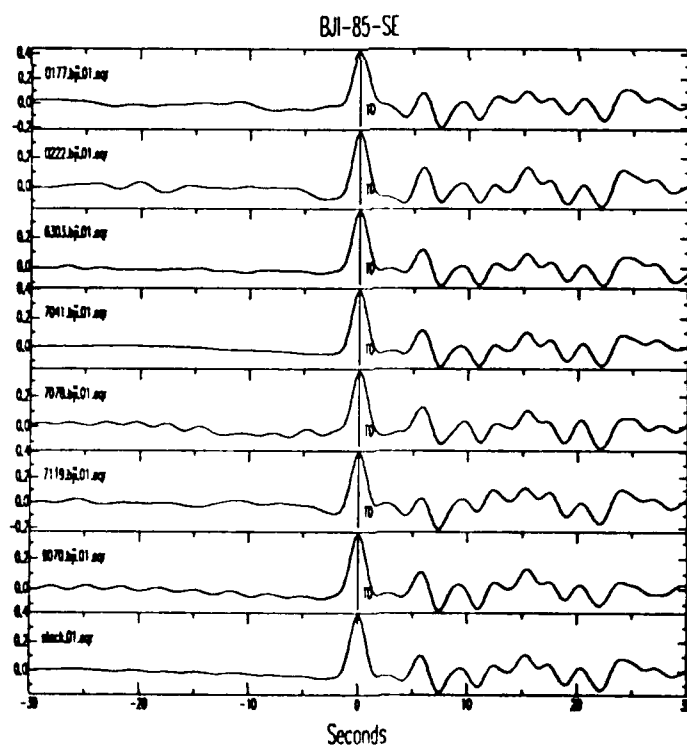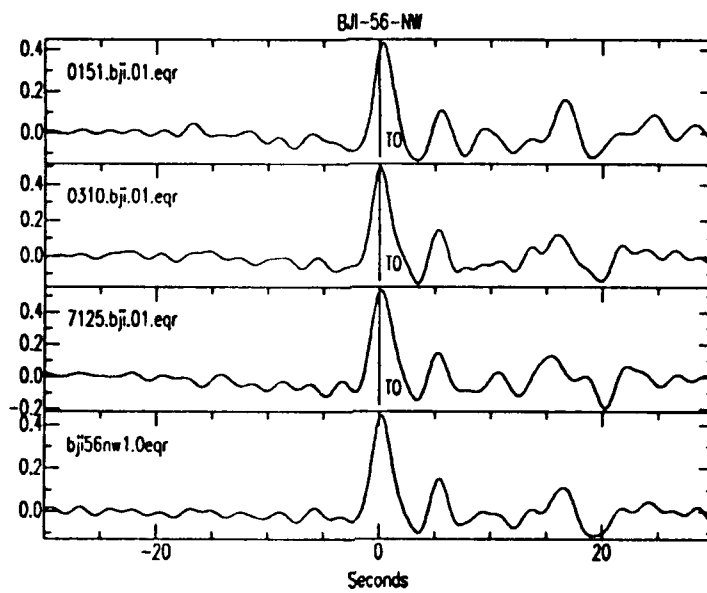
KMI Event Distribution
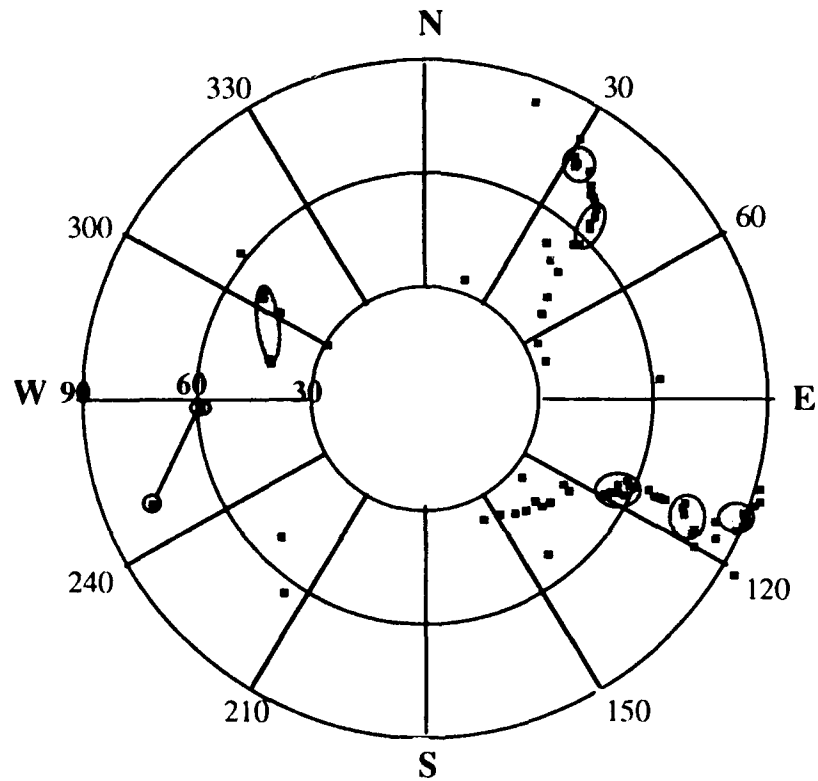
Figure A-7. Shaded ellipses correspond to azimuthal bins shown for each quadrant.
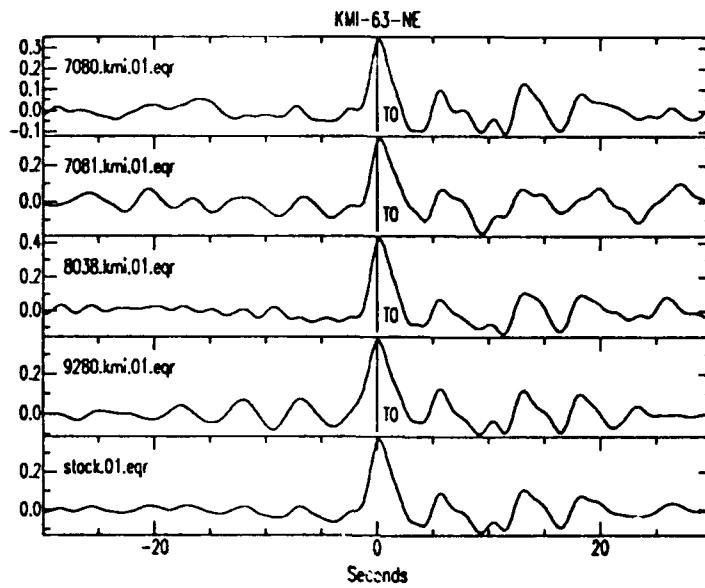
Figure A-8

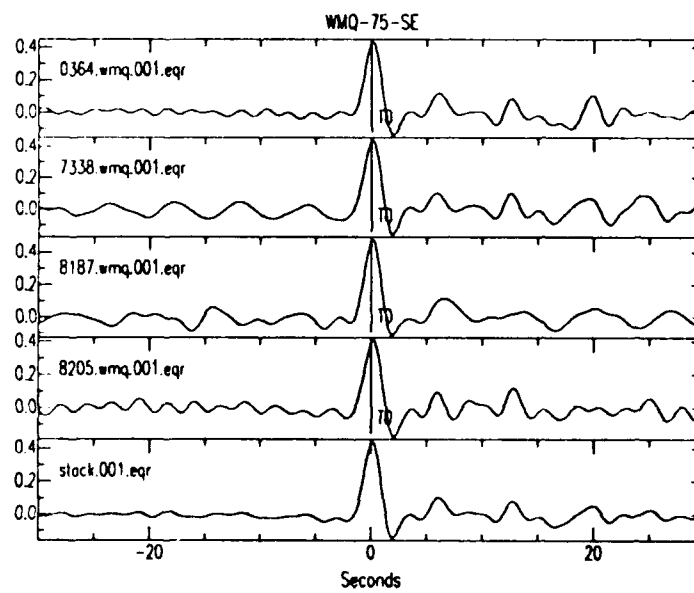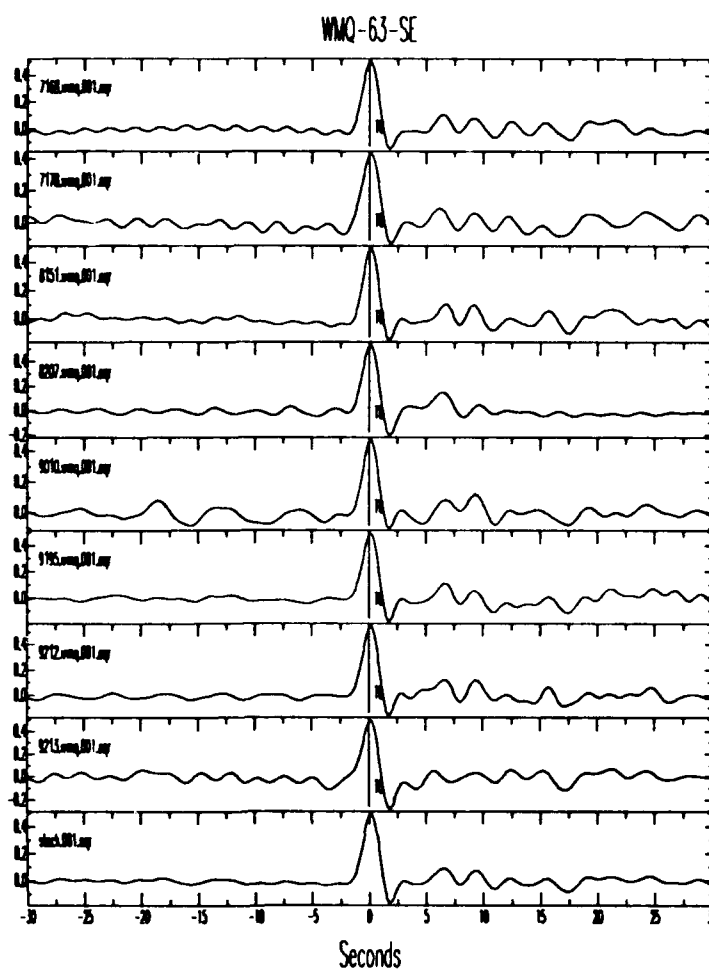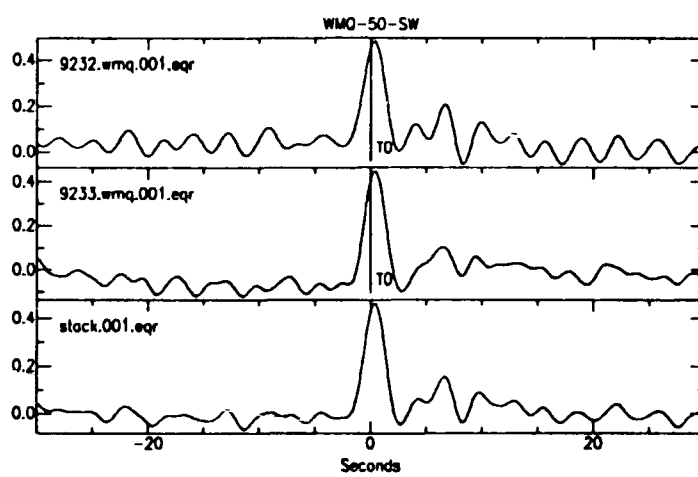Figure A-9

KMI-56-SE

Figure A-10

KMI-75-SE
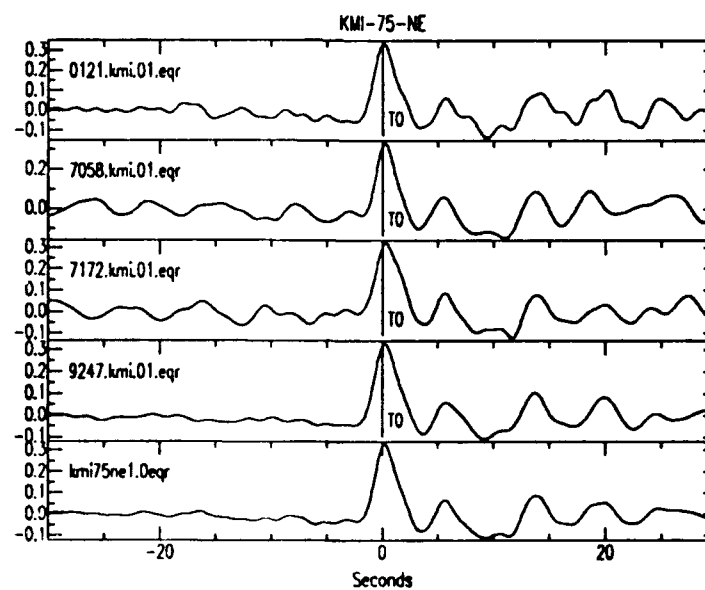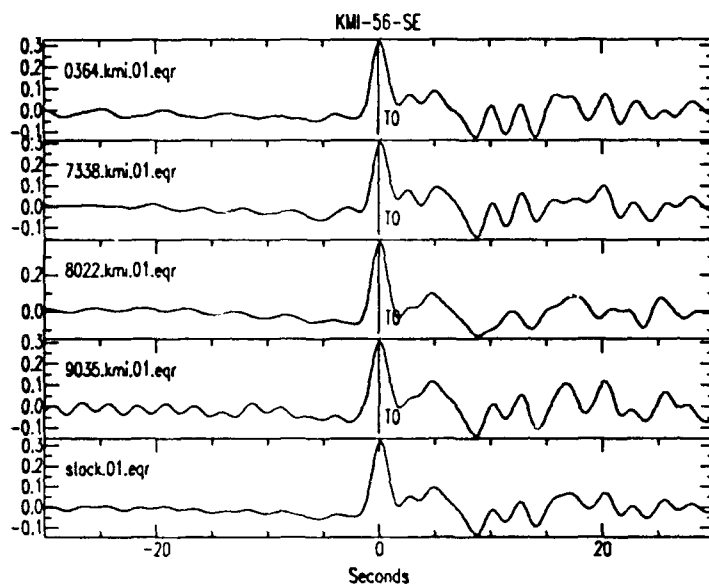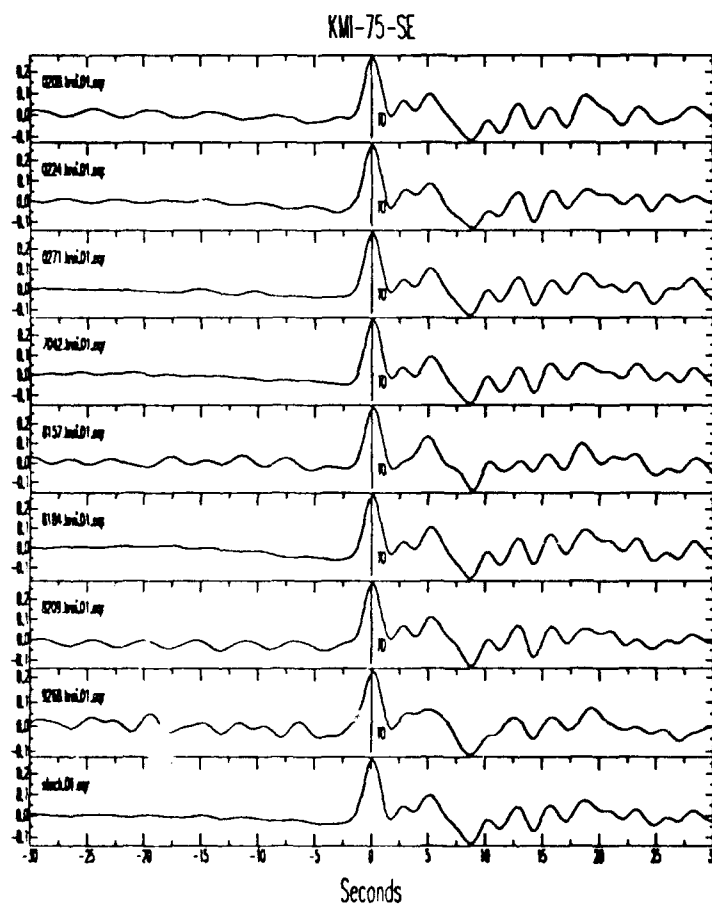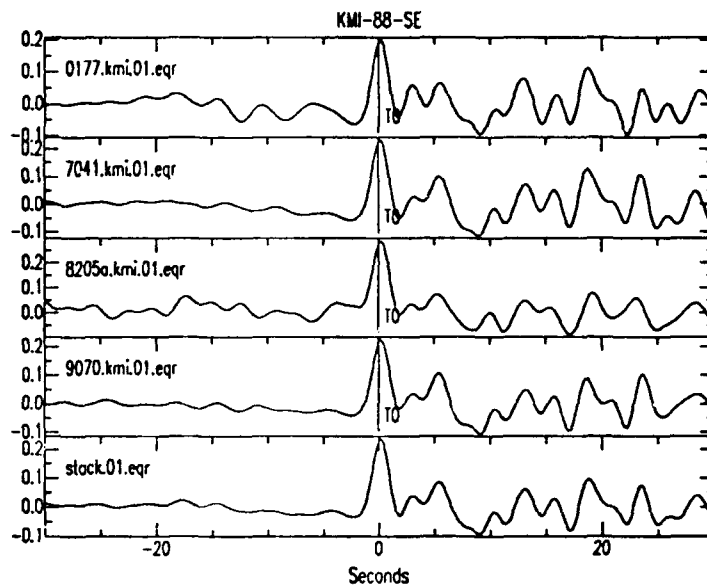
Figure A-11

Figure A-12
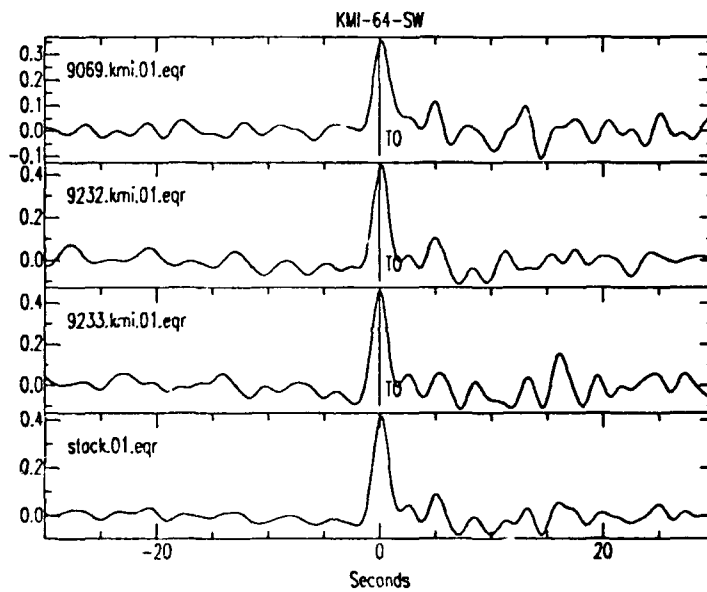
Figure A-13
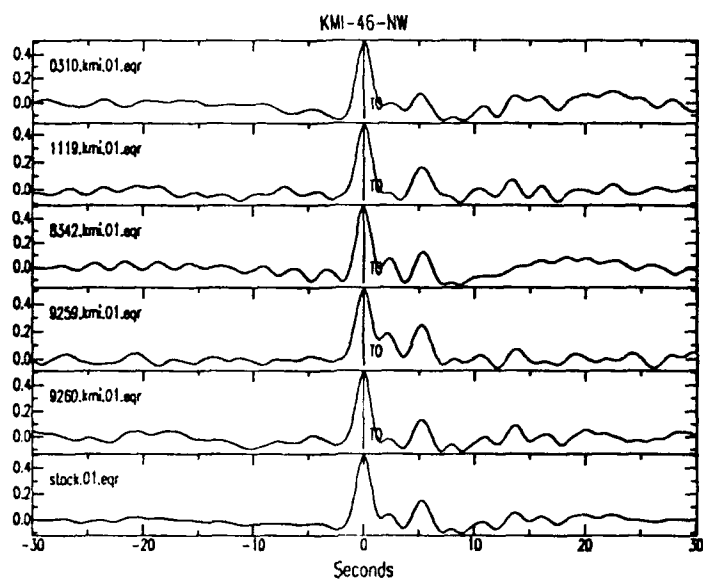
Figure A-14

LZH Event Distribution
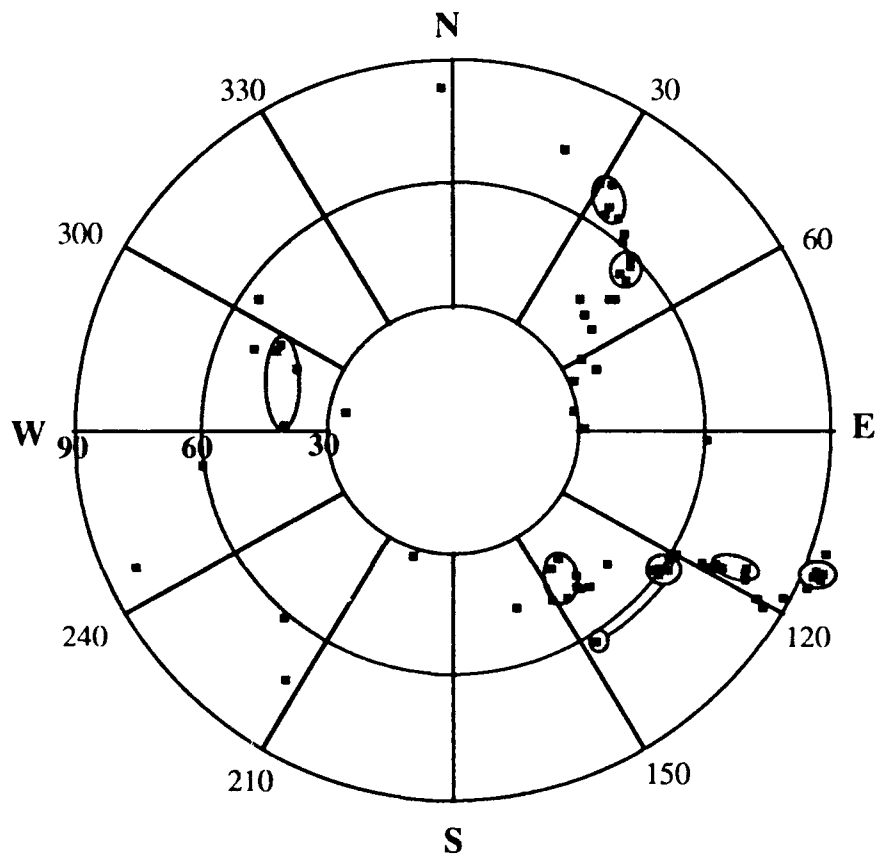
Figure A-15. Shaded ellipses correspond to azimuthal bins shown
for each quadrant.
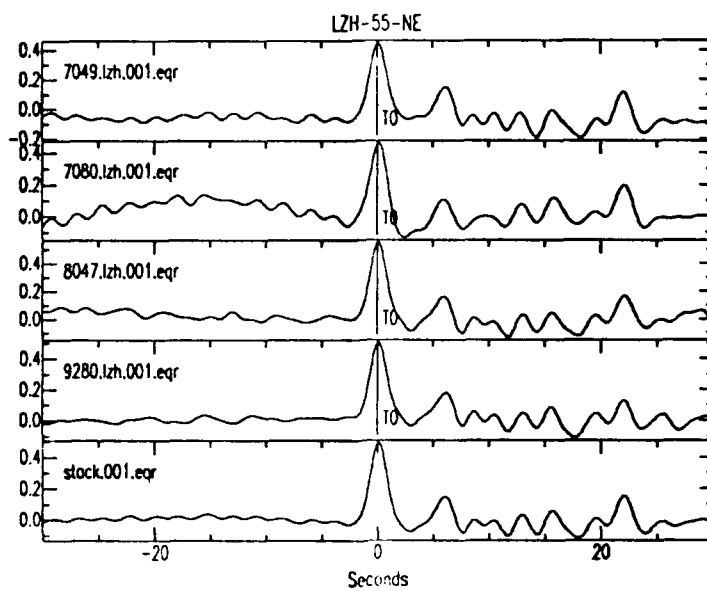
Figure A-16
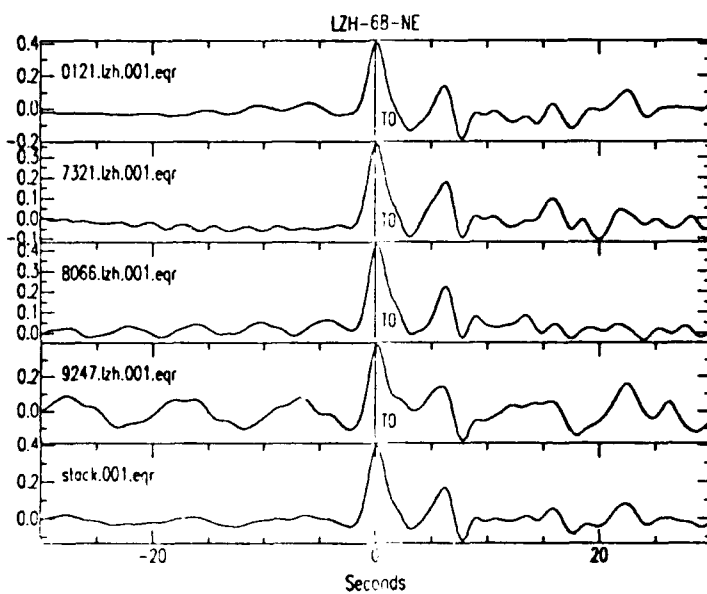
Figure A-17

Figure A-18

Figure A-19

81

LZH-77-SE

Figure A-20

LZH-93-SE

0177.lzh.001.eqr
6303.lzh.001.eqr
7041.lzh.001.eqr
7078.lzh.001.eqr
stack.001.eqr
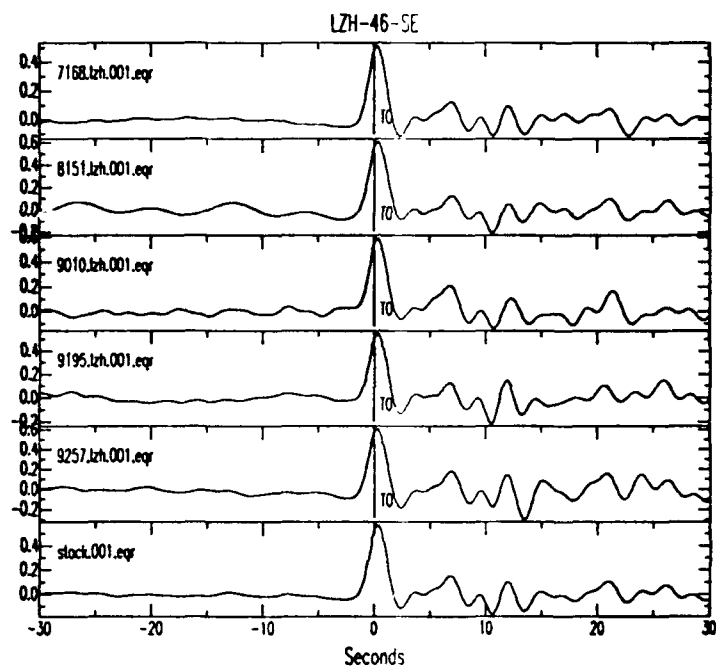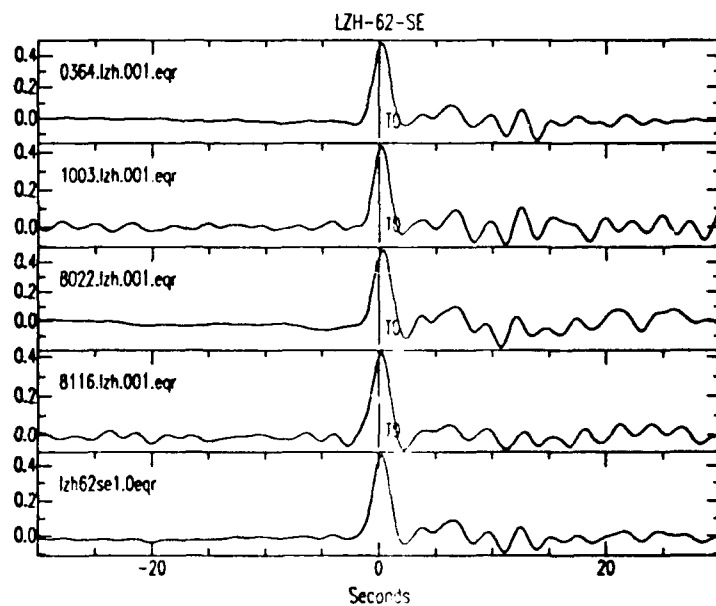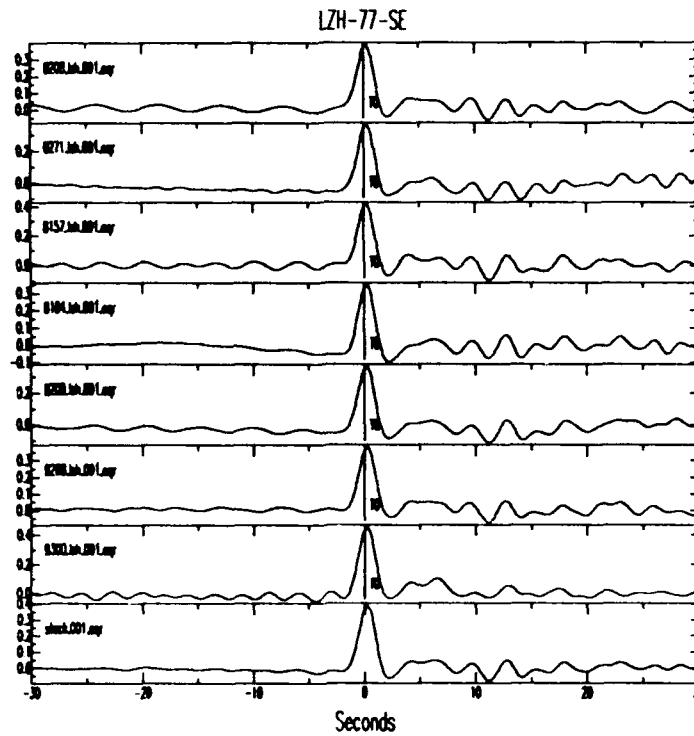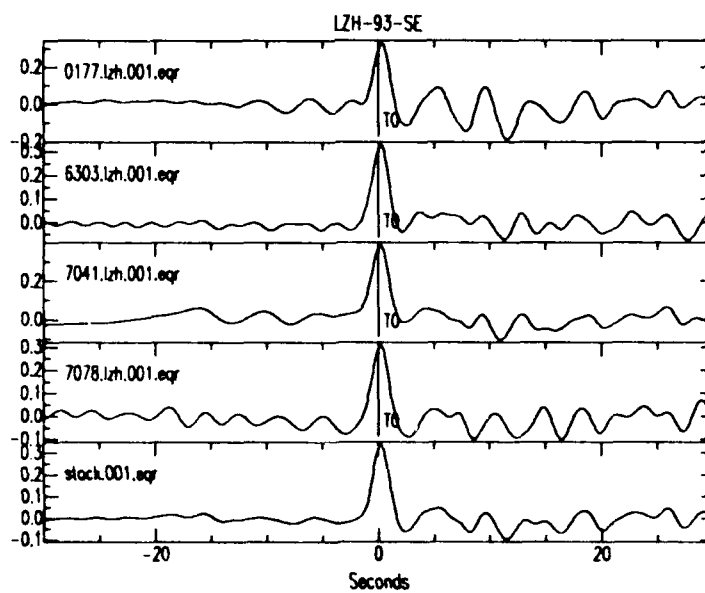
Figure A-21
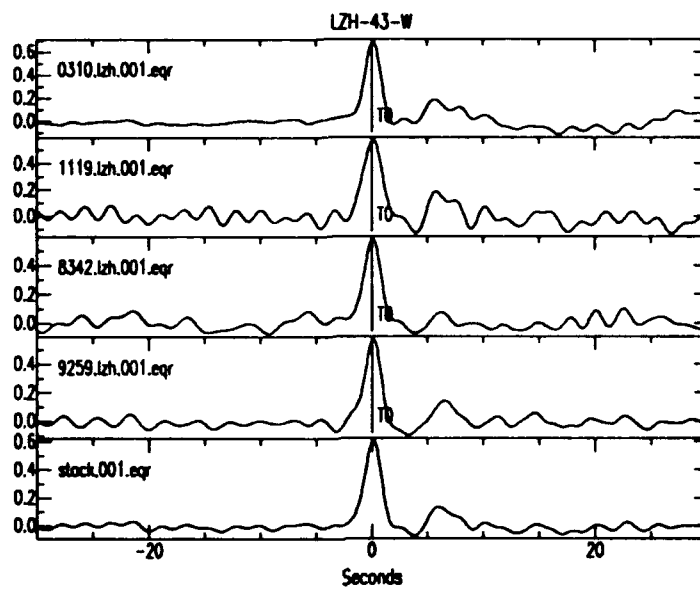
Figure A-22

HIA Event Distribution
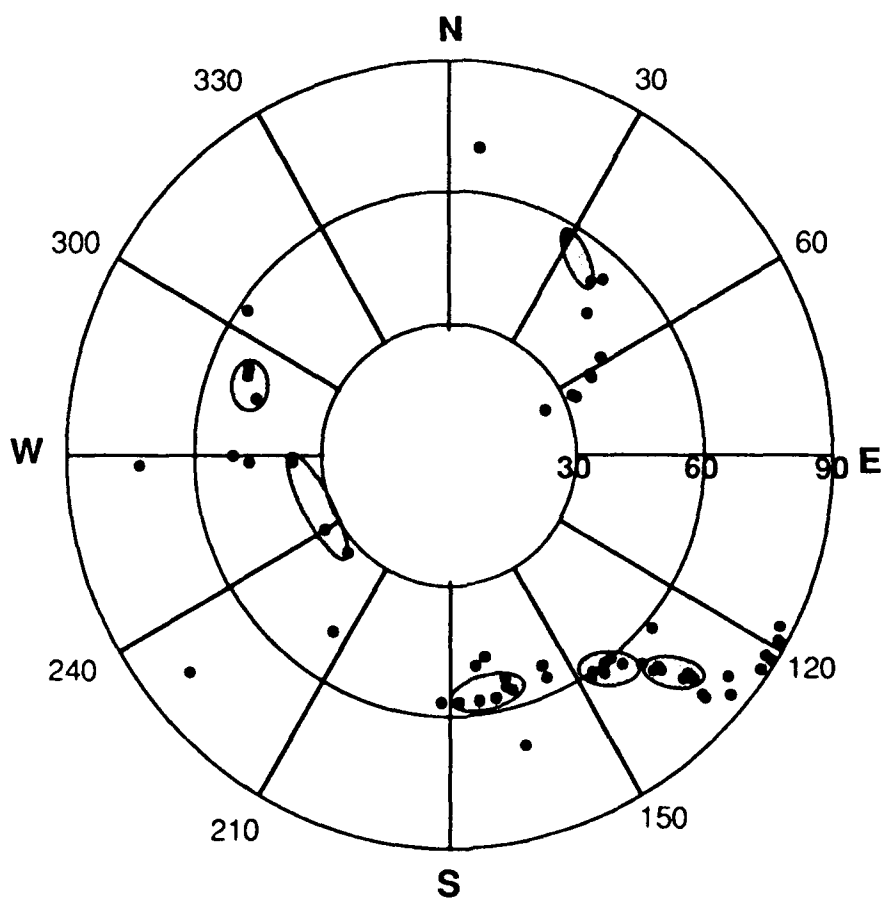
Figure A-23. Shaded ellipses correspond to azimuthal bins shown for each quadrant.

HIA-50-NE

8066.hia.001.eqr

8085.hia.001.eqr

9280.hia.001.eqr

stock.001.eqr

Seconds

Figure A-24

HIA-55-SE

7178.hia.001.eqr

8151.hia.001.eqr

9010.hia.001.eqr

9195.hia.001.eqr

9212.hia.001.eqr

stock.001.eqr

Seconds
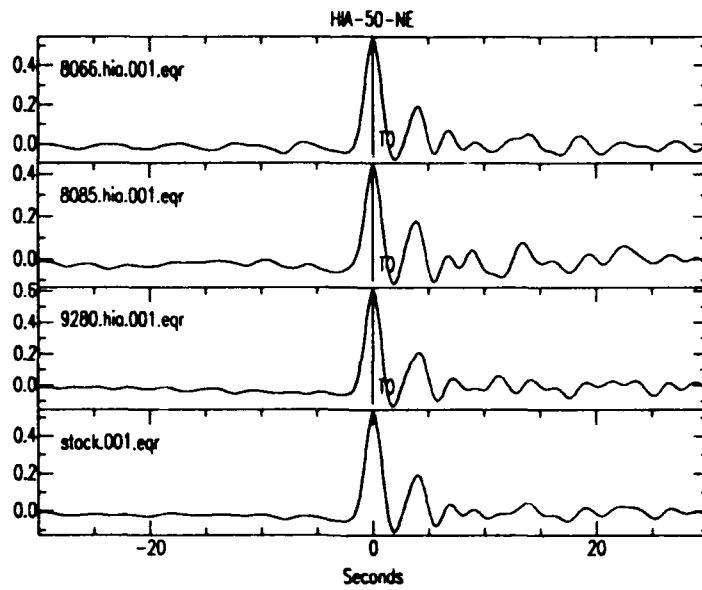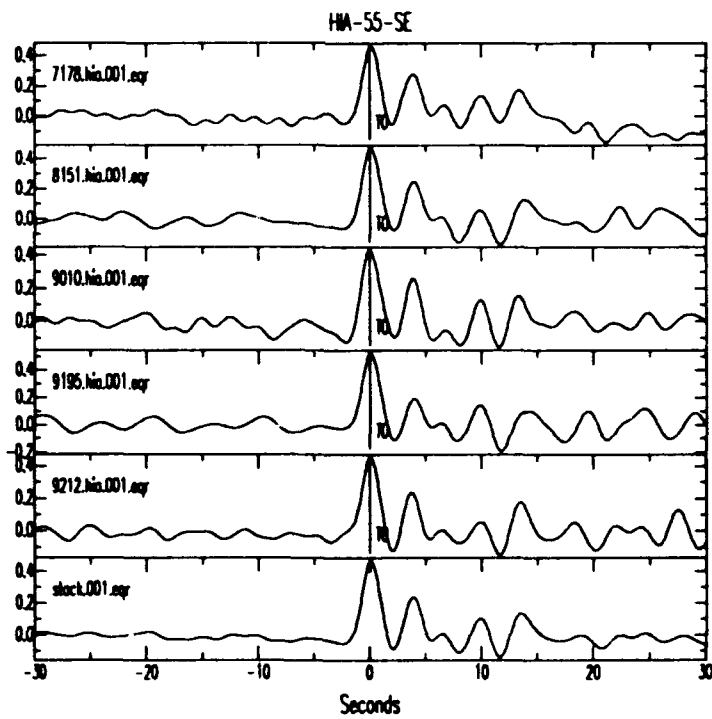
Figure A-25

85
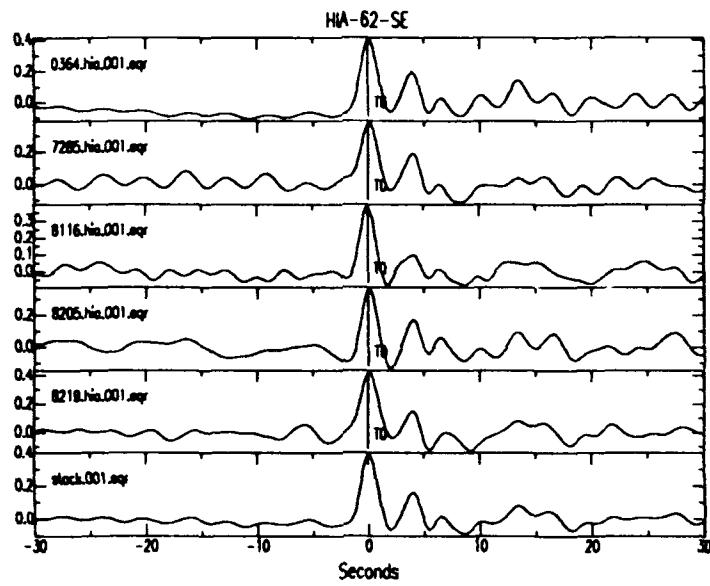
Figure A-26

Figure A-27

86
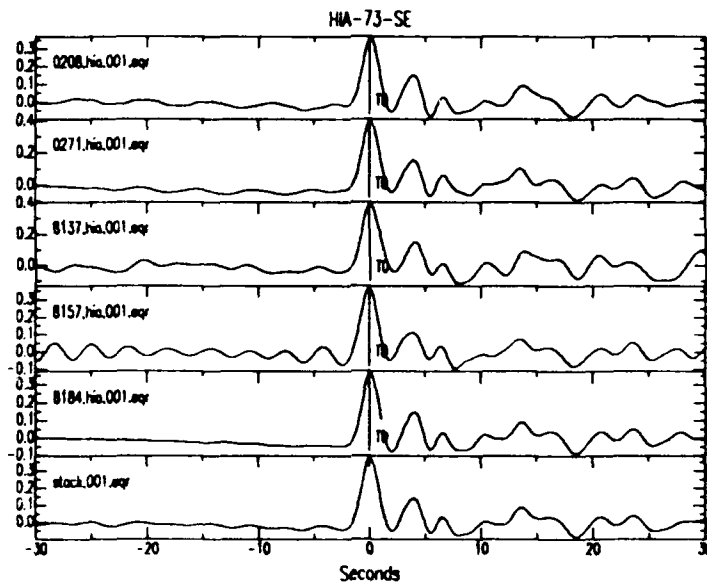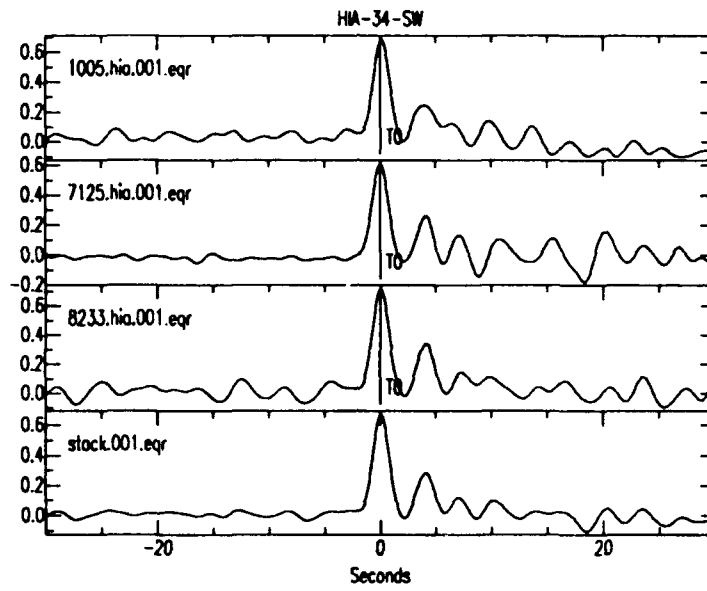
Figure A-28

Figure A-29

87
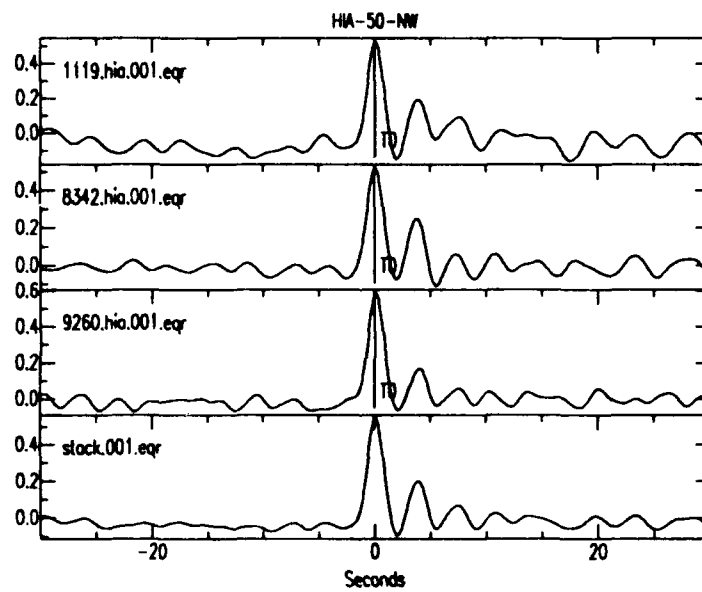
MDJ Event Distribution
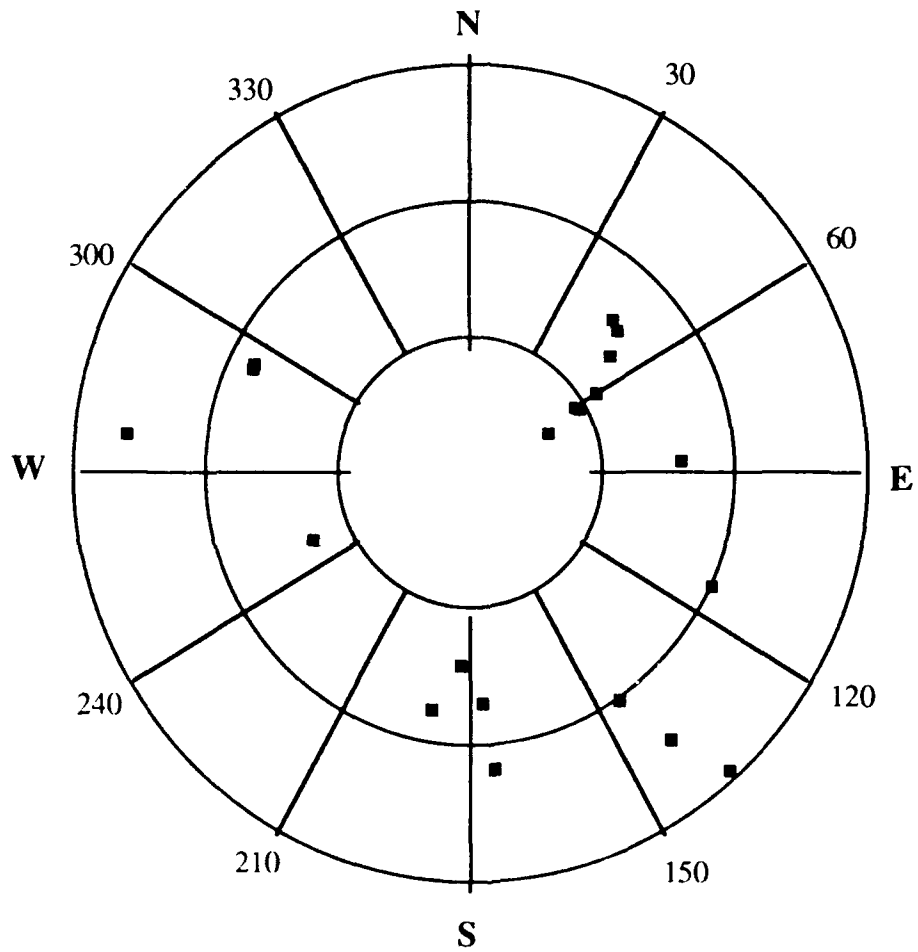
Figure A-30 1. Individual stacking suites are not available for each quadrant.
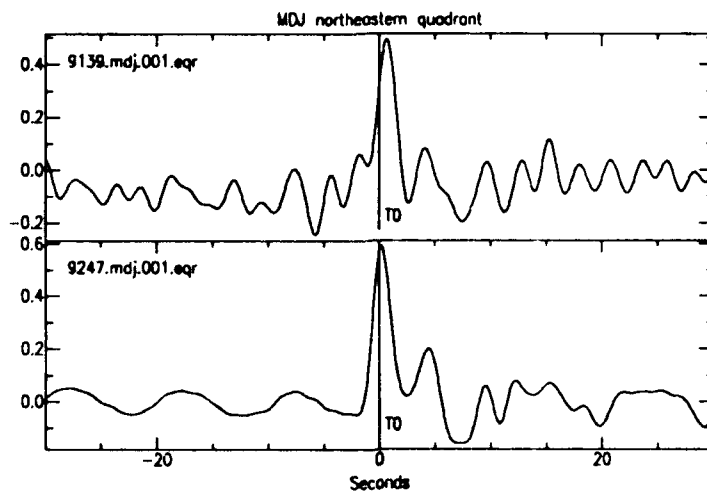
Figure A-31

Figure A-32

89
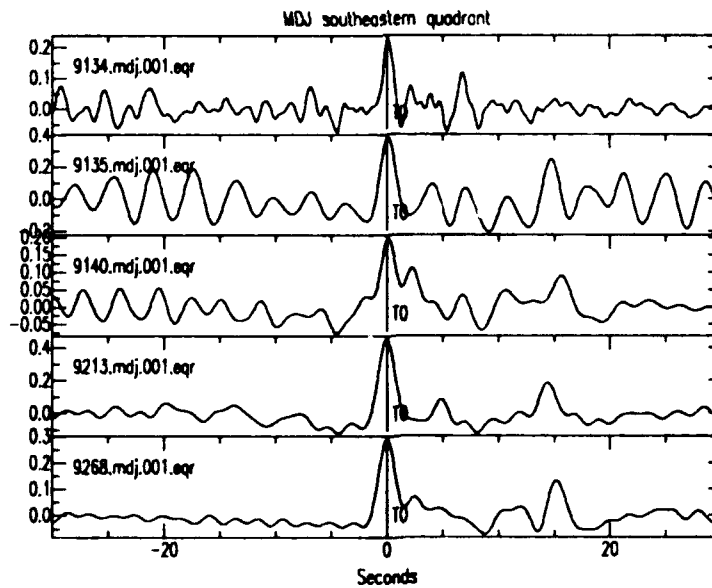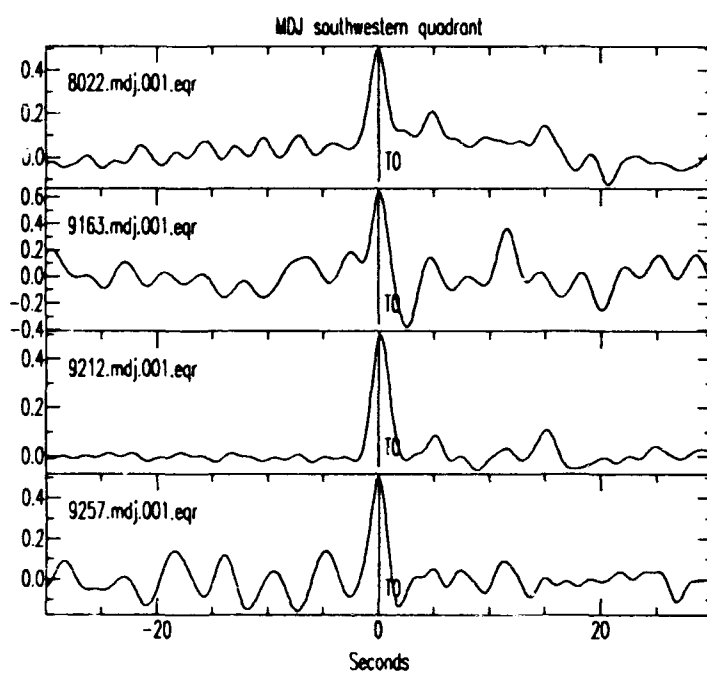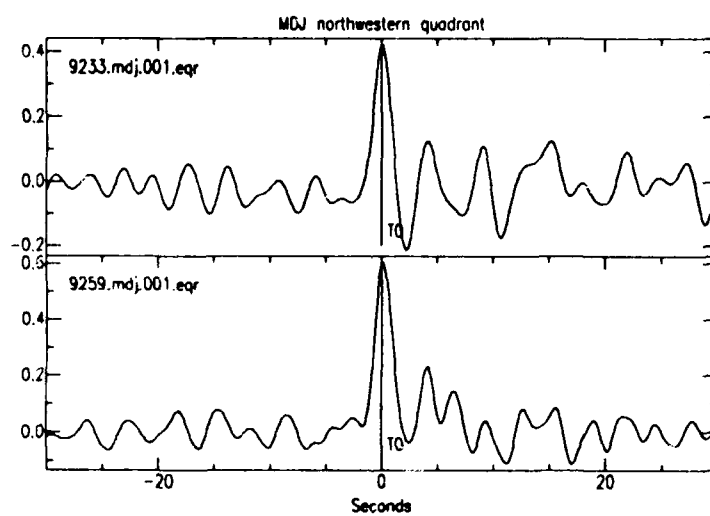
Figure A-33

Figure A-34

WMQ Event Distribution
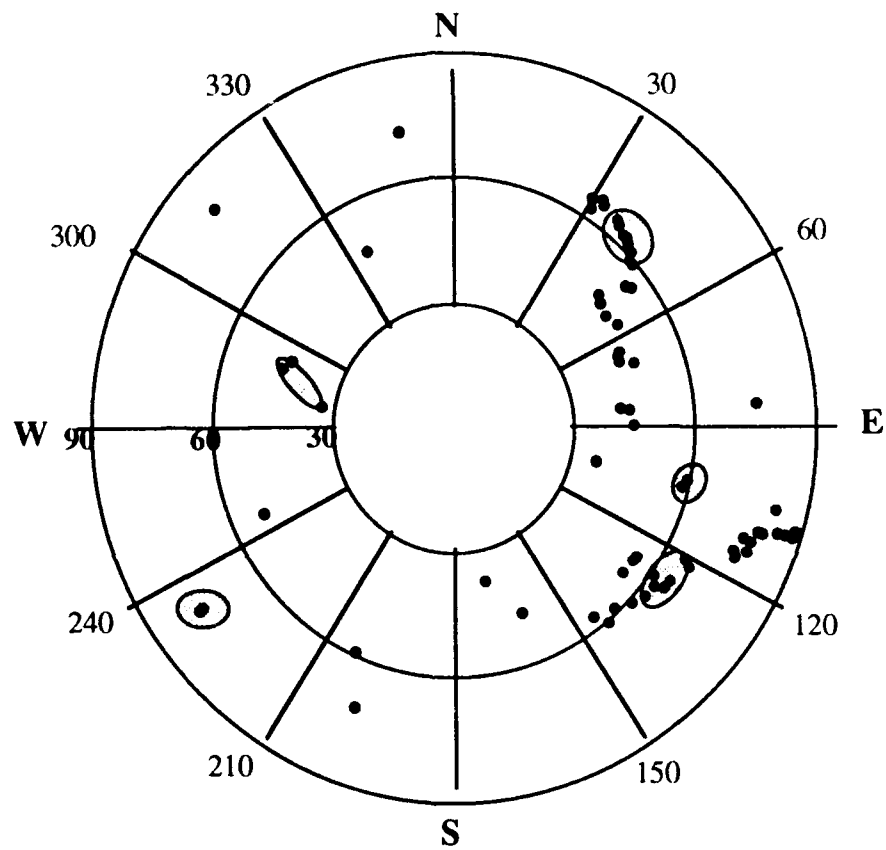
Figure A-35. Shaded ellipses correspond to azimuthal bins shown
for each quadrant.

WMQ-63-NE

Figure A-36

WMQ-75-SE

Figure A-37

92
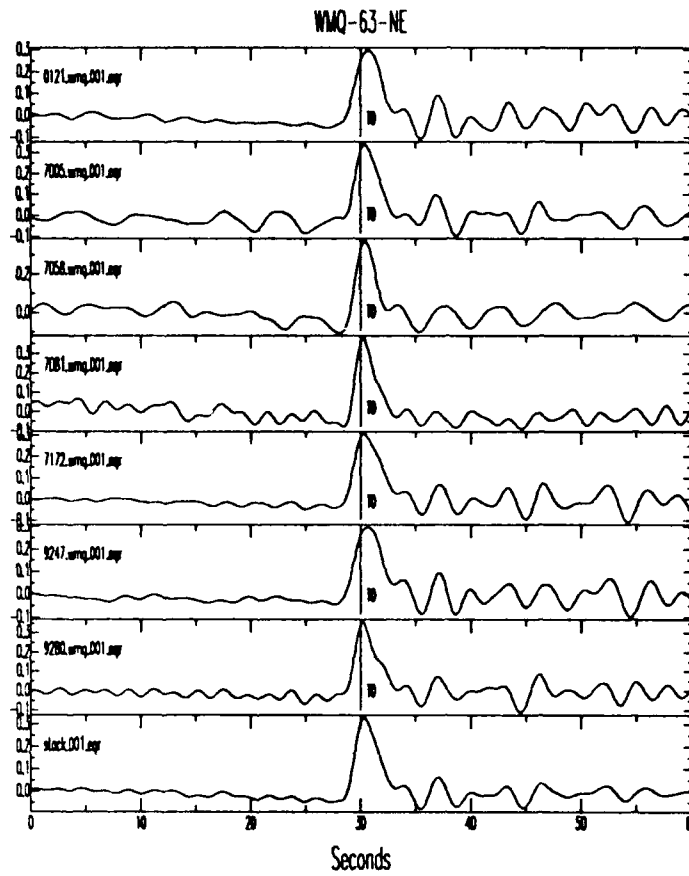
Figure A-38

Figure A-39
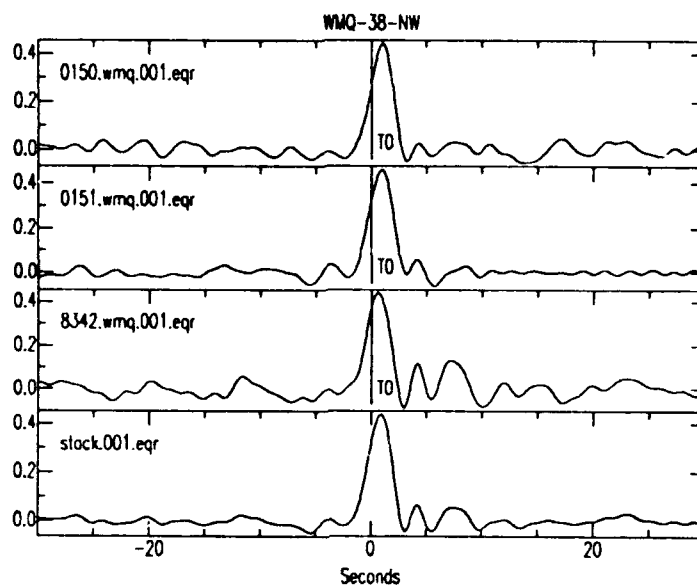
Figure A-40

Prof. Thomas Ahrens
Seismological Lab, 252-21
Division of Geological & Planetary Sciences
California Institute of Technology
Pasadena, CA 91125

Prof. Keiiti Aki
Center for Earth Sciences
University of Southern California
University Park
Los Angeles, CA 90089-0741

Prof. Shelton Alexander
Geosciences Department
403 Deike Building
The Pennsylvania State University
University Park, PA 16802

Dr. Ralph Alewine, III
DARPA/NMRO
3701 North Fairfax Drive
Arlington, VA 22203-1714

Prof. Charles B. Archambeau
CIRES
University of Colorado
Boulder, CO 80309

Dr. Thomas C. Bache, Jr.
Science Applications Int'l Corp.
10260 Campus Point Drive
San Diego, CA 92121 (2 copies)

Prof. Muawia Barazangi
Institute for the Study of the Continent
Cornell University
Ithaca, NY 14853

Dr. Jeff Barker
Department of Geological Sciences
State University of New York
 at Binghamton
Vestal, NY 13901

Dr. Douglas R. Baumgardt
ENSCO, Inc
5400 Port Royal Road
Springfield, VA 22151-2388

Dr. Susan Beck
Department of Geosciences
Building #77
University of Arizona
Tuscon, AZ 85721

Dr. T.J. Bennett
S-CUBED
A Division of Maxwell Laboratories
11800 Sunrise Valley Drive, Suite 1212
Reston, VA 22091

Dr. Robert Blandford
AFTAC/TT, Center for Seismic Studies
1300 North 17th Street
Suite 1450
Arlington, VA 22209-2308

Dr. G.A. Bollinger
Department of Geological Sciences
Virginia Polytechnical Institute
21044 Derring Hall
Blacksburg, VA 24061

Dr. Stephen Bratt
Center for Seismic Studies
1300 North 17th Street
Suite 1450
Arlington, VA 22209-2308

Dr. Lawrence Burdick
Woodward-Clyde Consultants
566 El Dorado Street
Pasadena, CA 91109-3245

Dr. Robert Burridge
Schlumberger-Doll Research Center
Old Quarry Road
Ridgefield, CT 06877

Dr. Jerry Carter
Center for Seismic Studies
1300 North 17th Street
Suite 1450
Arlington, VA 22209-2308

Dr. Eric Chael
Division 9241
Sandia Laboratory
Albuquerque, NM 87185

Prof. Vernon F. Cormier
Department of Geology & Geophysics
U-45, Room 207
University of Connecticut
Storrs, CT 06268

Prof. Steven Day
Department of Geological Sciences
San Diego State University
San Diego, CA 92182

1

Marvin Denny
U.S. Department of Energy
Office of Arms Control
Washington, DC 20585

Dr. Zoltan Der
ENSCO, Inc.
5400 Port Royal Road
Springfield, VA 22151-2388

Prof. Adam Dziewonski
Hoffman Laboratory, Harvard University
Dept. of Earth Atmos. & Planetary Sciences
20 Oxford Street
Cambridge, MA 02138

Prof. John Ebel
Department of Geology & Geophysics
Boston College
Chestnut Hill, MA 02167

Eric Fielding
SNEE Hall
INSTOC
Cornell University
Ithaca, NY 14853

Dr. Mark D. Fisk
Mission Research Corporation
735 State Street
P.O. Drawer 719
Santa Barbara, CA 93102

Prof Stanley Flatte
Applied Sciences Building
University of California, Santa Cruz
Santa Cruz, CA 95064

Dr. John Foley
NER-Geo Sciences
1100 Crown Colony Drive
Quincy, MA 02169

Prof. Donald Forsyth
Department of Geological Sciences
Brown University
Providence, RI 02912

Dr. Art Frankel
U.S. Geological Survey
922 National Center
Reston, VA 22092

Dr. Cliff Frolich
Institute of Geophysics
8701 North Mopac
Austin, TX 78759

Dr. Holly Given
IGPP, A-025
Scripps Institute of Oceanography
University of California, San Diego
La Jolla, CA 92093

Dr. Jeffrey W. Given
SAIC
10260 Campus Point Drive
San Diego, CA 92121

Dr. Dale Glover
Defense Intelligence Agency
ATTN: ODT-1B
Washington, DC 20301

Dr. Indra Gupta
Teledyne Geotech
314 Montgomery Street
Alexanderia, VA 22314

Dan N. Hagedon
Pacific Northwest Laboratories
Battelle Boulevard
Richland, WA 99352

Dr. James Hannon
Lawrence Livermore National Laboratory
P.O. Box 808
L-205
Livermore, CA 94550

Dr. Roger Hansen
HQ AFTAC/TTR
Patrick AFB, FL 32925-6001

Prof. David G. Harkrider
Seismological Laboratory
Division of Geological & Planetary Sciences
California Institute of Technology
Pasadena, CA 91125

Prof. Danny Harvey
CIRES
University of Colorado
Boulder, CO 80309

2

Prof. Donald V. Helmberger
Seismological Laboratory
Division of Geological & Planetary Sciences
California Institute of Technology
Pasadena, CA 91125

Prof. Eugene Herrin
Institute for the Study of Earth and Man
Geophysical Laboratory
Southern Methodist University
Dallas, TX 75275

Prof. Robert B. Herrmann
Department of Earth & Atmospheric Sciences
St. Louis University
St. Louis, MO 63156

Prof. Lane R. Johnson
Seismographic Station
University of California
Berkeley, CA 94720

Prof. Thomas H. Jordan
Department of Earth, Atmospheric &
  Planetary Sciences
Massachusetts Institute of Technology
Cambridge, MA 02139

Prof. Alan Kafka
Department of Geology & Geophysics
Boston College
Chestnut Hill, MA 02167

Robert C. Kemerait
ENSCO, Inc.
445 Pineda Court
Melbourne, FL 32940

Dr. Max Koontz
U.S. Dept. of Energy/DP 5
Forrestal Building
1000 Independence Avenue
Washington, DC 20585

Dr. Richard LaCoss
MIT Lincoln Laboratory, M-200B
P.O. Box 73
Lexington, MA 02173-0073

Dr. Fred K. Lamb
University of Illinois at Urbana-Champaign
Department of Physics
1110 West Green Street
Urbana, IL 61801

Prof. Charles A. Langston
Geosciences Department
403 Deike Building
The Pennsylvania State University
University Park, PA 16802

Jim Lawson, Chief Geophysicist
Oklahoma Geological Survey
Oklahoma Geophysical Observatory
P.O. Box 8
Leonard, OK 74043-0008

Prof. Thorne Lay
Institute of Tectonics
Earth Science Board
University of California, Santa Cruz
Santa Cruz, CA 95064

Dr. William Leith
U.S. Geological Survey
Mail Stop 928
Reston, VA 22092

Mr. James F. Lewkowicz
Phillips Laboratory/GPEH
Hanscom AFB, MA 01731-5000(2 copies)

Mr. Alfred Lieberman
ACDA/VI-OA State Department Building
Room 5726
320-21st Street, NW
Washington, DC 20451

Prof. L. Timothy Long
School of Geophysical Sciences
Georgia Institute of Technology
Atlanta, GA 30332

Dr. Randolph Martin, III
New England Research, Inc.
76 Olcott Drive
White River Junction, VT 05001

Dr. Robert Masse
Denver Federal Building
Box 25046, Mail Stop 967
Denver, CO 80225

Dr. Gary McCartor
Department of Physics
Southern Methodist University
Dallas, TX 75275

Dr. Richard Sailor
TASC, Inc.
55 Walkers Brook Drive
Reading, MA 01867

Prof. Charles G. Sammis
Center for Earth Sciences
University of Southern California
University Park
Los Angeles, CA 90089-0741

Prof. Christopher H. Scholz
Lamont-Doherty Geological Observatory
 of Columbia University
Palisades, CA 10964

Dr. Susan Schwartz
Institute of Tectonics
1156 High Street
Santa Cruz, CA 95064

Secretary of the Air Force
(SAFRD)
Washington, DC 20330

Office of the Secretary of Defense
DDR&E
Washington, DC 20330

Thomas J. Sereno, Jr.
Science Application Int'l Corp.
10260 Campus Point Drive
San Diego, CA 92121

Dr. Michael Shore
Defense Nuclear Agency/SPSS
6801 Telegraph Road
Alexandria, VA 22310

Dr. Matthew Sibol
Virginia Tech
Seismological Observatory
4044 Derring Hall
Blacksburg, VA 24061-0420

Prof. David G. Simpson
IRIS, Inc.
1616 North Fort Myer Drive
Suite 1440
Arlington, VA 22209

Donald L. Springer
Lawrence Livermore National Laboratory
L-025
P.O. Box 808
Livermore, CA 94550

Dr. Jeffrey Stevens
S-CUBED
A Division of Maxwell Laboratory
P.O. Box 1620
La Jolla, CA 92038-1620

Lt. Col. Jim Stobie
ATTN: AFOSR/NL
Bolling AFB
Washington, DC 20332-6448

Prof. Brian Stump
Institute for the Study of Earth & Man
Geophysical Laboratory
Southern Methodist University
Dallas, TX 75275

Prof. Jeremiah Sullivan
University of Illinois at Urbana-Champaign
Department of Physics
1110 West Green Street
Urbana, IL 61801

Prof. L. Sykes
Lamont-Doherty Geological Observatory
 of Columbia University
Palisades, NY 10964

Dr. David Taylor
ENSCO, Inc.
445 Pineda Court
Melbourne, FL 32940

Dr. Steven R. Taylor
Los Alamos National Laboratory
P.O. Box 1663
Mail Stop C335
Los Alamos, NM 87545

Prof. Clifford Thurber
University of Wisconsin-Madison
Department of Geology & Geophysics
1215 West Dayton Street
Madison, WS 53706

Prof. M. Nafi Toksoz
Earth Resources Lab
Massachusetts Institute of Technology
42 Carleton Street
Cambridge, MA 02142

5

Dr. Larry Turnbull
CIA-OSWR/NED
Washington, DC 20505

DARPA/RMO/SECURITY OFFICE
3701 North Fairfax Drive
Arlington, VA 22203-1714

Dr. Gregory van der Vink
IRIS, Inc.
1616 North Fort Myer Drive
Suite 1440
Arlington, VA 22209

HQ DNA
ATTN: Technical Library
Washington, DC 20305

Dr. Karl Veith
EG&G
5211 Auth Road
Suite 240
Suitland, MD 20746

Defense Intelligence Agency
Directorate for Scientific & Technical Intelligence
ATTN: DTIB
Washington, DC 20340-6158

Prof. Terry C. Wallace
Department of Geosciences
Building #77
University of Arizona
Tuscon, AZ 85721

Defense Technical Information Center
Cameron Station
Alexandria, VA 22314 (2 Copies)

Dr. Thomas Weaver
Los Alamos National Laboratory
P.O. Box 1663
Mail Stop C335
Los Alamos, NM 87545

TACTEC
Battelle Memorial Institute
505 King Avenue
Columbus, OH 43201 (Final Report)

Dr. William Wortman
Mission Research Corporation
8560 Cinderbed Road
Suite 700
Newington, VA 22122

Phillips Laboratory
ATTN: XPG
Hanscom AFB, MA 01731-5000

Prof. Francis T. Wu
Department of Geological Sciences
State University of New York
 at Binghamton
Vestal, NY 13901

Phillips Laboratory
ATTN: GPE
Hanscom AFB, MA 01731-5000

AFTAC/CA
(STINFO)
Patrick AFB, FL 32925-6001

Phillips Laboratory
ATTN: TSML
Hanscom AFB, MA 01731-5000

DARPA/PM
3701 North Fairfax Drive
Arlington, VA 22203-1714

Phillips Laboratory
ATTN: SUL
Kirtland, NM 87117 (2 copies)

DARPA/RMO/RETRIEVAL
3701 North Fairfax Drive
Arlington, VA 22203-1714

Dr. Michel Bouchon
I.R.I.G.M.-B.P. 68
38402 St. Martin D'Heres
Cedex, FRANCE

Dr. Michel Campillo
Observatoire de Grenoble
I.R.I.G.M.-B.P. 53
38041 Grenoble, FRANCE

Dr. Jorg Schlittenhardt
Federal Institute for Geosciences & Nat'l Res.
Postfach 510153
D-3000 Hannover 51, GERMANY

Dr. Kin Yip Chun
Geophysics Division
Physics Department
University of Toronto
Ontario, CANADA

Dr. Johannes Schweitzer
Institute of Geophysics
Ruhr University/Bochum
P.O. Box 1102148
4360 Bochum 1, GERMANY

Prof. Hans-Peter Harjes
Institute for Geophysic
Ruhr University/Bochum
P.O. Box 102148
4630 Bochum 1, GERMANY

Prof. Eystein Husebye
NTNF/NORSAR
P.O. Box 51
N-2007 Kjeller, NORWAY

David Jepsen
Acting Head, Nuclear Monitoring Section
Bureau of Mineral Resources
Geology and Geophysics
G.P.O. Box 378, Canberra, AUSTRALIA

Ms. Eva Johannisson
Senior Research Officer
National Defense Research Inst.
P.O. Box 27322
S-102 54 Stockholm, SWEDEN

Dr. Peter Marshall
Procurement Executive
Ministry of Defense
Blacknest, Brimpton
Reading FG7-FRS, UNITED KINGDOM

Dr. Bernard Massinon, Dr. Pierre Mechler
Societe Radiomana
27 rue Claude Bernard
75005 Paris, FRANCE (2 Copies)

Dr. Svein Mykkeltveit
NTNT/NORSAR
P.O. Box 51
N-2007 Kjeller, NORWAY (3 Copies)

Prof. Keith Priestley
University of Cambridge
Bullard Labs, Dept. of Earth Sciences
Madingley Rise, Madingley Road
Cambridge CB3 OEZ, ENGLAND